19

Mechanics of Carbon Nanotubes[1]

CONTENTS

Dong Qian
Northwestern University

Gregory J. Wagner
Northwestern University

Wing Kam Liu
Northwestern University

Min-Feng Yu
University of Illinois

Rodney S. Ruoff
Northwestern University

Abstract

Soon after the discovery of carbon nanotubes, it was realized that the theoretically predicted mechanical properties of these interesting structures — including high strength, high stiffness, low density, and structural perfection — could make them ideal for a wealth of technological applications. The experimental verification, and in some cases refutation, of these predictions, along with a number of computer simulation methods applied to their modeling, has led over the past decade to an improved but by no means complete understanding of the mechanics of carbon nanotubes. We review the theoretical predictions and discuss the experimental techniques that are most often used for the challenging tasks of visualizing and manipulating these tiny structures. We also outline the computational approaches that have been taken, including *ab initio* quantum mechanical simulations, classical molecular dynamics, and continuum models. The development of multiscale and multiphysics models and simulation tools naturally arises as a result of the link between basic scientific research and engineering application; while this issue is still under intensive study, we present here some of the approaches to this topic. Our

---

[1] This chapter appeared previously in *Applied Mechanics Reviews,* 56, 6, 2002. It is reprinted here with permission of ASME International.

concentration throughout is on the exploration of mechanical properties such as Young's modulus, bending stiffness, buckling criteria, and tensile and compressive strengths. Finally, we discuss several examples of exciting applications that take advantage of these properties, including nanoropes, filled nanotubes, nanoelectromechanical systems, nanosensors, and nanotube-reinforced polymers.

19.1   Introduction

The discovery of multi-walled carbon nanotubes (MWCNTs) in 1991[1] has stimulated ever-broader research activities in science and engineering devoted entirely to carbon nanostructures and their applications. This is due in large part to the combination of their expected structural perfection, small size, low density, high stiffness, high strength (the tensile strength of the outermost shell of an MWCNT is approximately 100 times greater than that of aluminum), and excellent electronic properties. As a result, carbon nanotubes (CNTs) may find use in a wide range of applications in material reinforcement, field-emission panel display, chemical sensing, drug delivery, and nanoelectronics.

Indeed, NASA is developing materials using nanotubes for space applications, where weight-driven cost is the major concern, by taking advantage of their tremendous stiffness and strength. Composites based on nanotubes could offer strength-to-weight ratios beyond any materials currently available. Companies such as Samsung and NEC have invested tremendously and demonstrated product quality devices utilizing carbon nanotubes for field-emission display.[2,3] Such devices have shown superior qualities such as low turn-on electric field, high-emission current density, and high stability. With the advance of materials synthesis and device processing capabilities, the importance of developing and understanding nanoscale engineering devices has dramatically increased over the past decade. Compared with other nanoscale materials, single-walled carbon nanotubes (SWCNTs) possess particularly outstanding physical and chemical properties. SWCNTs are remarkably stiff and strong, conduct electricity, and are projected to conduct heat even better than diamond, which suggests their eventual use in nanoelectronics. Steady progress has been made recently in developing SWCNT nanodevices and nanocircuits,[4,5] showing remarkable logic and amplification functions. SWCNTs are also under intensive study as efficient storage devices, both for alkali ions for nanoscale power sources and for hydrogen for fuel cell applications.

On other fronts, CNTs also show great potential for biomedical applications due to their biocompatibility and high strength. The current generation of composites used for replacement of bone and teeth are crude admixtures of filler particles (often glass) that have highly inadequate mechanical properties compared with skeletal tissue. Fiber-based composites have been investigated in the past but have not worked well because of eventual degradation of the filler/matrix interface, usually due to attack by water. Thus, a major issue is interfacial stability under physiological conditions. Graphitic materials are known to resist degradation in the types of chemical environments present in the body. Recent demonstration of CNT artificial muscle[6] is one step along this direction and promises a dramatic increase in work density output and force generation over known technologies, along with the ability to operate at low voltage. CNTs are also being considered for drug delivery: they could be implanted without trauma at the sites where a drug is needed, slowly releasing a drug over time. They are also of considerable promise in cellular experiments, where they can be used as nanopipettes for the distribution of extremely small volumes of liquid or gas into living cells or onto surfaces. It is also conceivable that they could serve as a medium for implantation of diagnostic devices.

The rapid pace of research development as well as industry application has made it necessary to summarize the current status about what we have known and what we do not know about this particularly interesting nanostructure. A number of excellent reviews on the general properties of CNTs can be found in References 7–9. In this paper we have made this effort with emphasis on the mechanical aspects.

The paper is organized as follows: Section 19.2 focuses on the mechanical properties of CNTs. This includes the basic molecular structure, elastic properties, strength, and crystal elasticity treatment. Section 19.3 summarizes the current experimental techniques that were used in the measurement of the mechanical properties of CNTs. A brief discussion on the challenges in the experiment is also presented. Various simulation methods are discussed in Section 19.4. The length scale spans from

quantum level to continuum level, which highlights the multiscale and multiphysics features of the nanoscale problem. Section 19.5 considers a few important mechanical applications of CNTs. Finally, conclusions are made in Section 19.6.

19.2 Mechanical Properties of Nanotubes

19.2.1 Molecular Structure of CNTs

19.2.1.1 Bonding Mechanisms

The mechanical properties of CNTs are closely related to the nature of the bonds between carbon atoms. The bonding mechanism in a carbon nanotube system is similar to that of graphite, as a CNT can be thought of as a rolled-up graphene sheet. The atomic number for carbon is 6, and the atom electronic structure is $1s^2 2s^2 2p^2$ in atomic physics notation. For a detailed description of the notation and the structure, readers may refer to basic textbooks on general chemistry or physics.[10] When carbon atoms combine to form graphite, sp^2 hybridization[10] occurs. In this process, one *s*-orbital and two *p*-orbitals combine to form three hybrid sp^2-orbitals at 120° to each other within a plane (shown in Figure 19.1). This in-plane bond is referred to as a σ-bond (*sigma*-bond). This is a strong covalent bond that binds the atoms in the plane and results in the high stiffness and high strength of a CNT. The remaining *p*-orbital is perpendicular to the plane of the σ-bonds. It contributes mainly to the interlayer interaction and is called the π-bond (*pi*-bond). These out-of-plane, delocalized π-bonds interact with the π-bonds on the neighboring layer. This interlayer interaction of atom pairs on neighboring layers is much weaker than a σ-bond. For instance, in the experimental study of *shell-sliding*,[11] it was found that the shear strength between the outermost shell and the neighboring inner shell was 0.08 MPa and 0.3 MPa according to two separate measurements on two different MWCNTs. The bond structure of a graphene sheet is shown in Figure 19.1.

19.2.1.2 From Graphene Sheet to Single-Walled Nanotube

There are various ways of defining a unique structure for each carbon nanotube. One way is to think of each CNT as a result of rolling a graphene sheet, by specifying the direction of rolling and the circumference of the cross-section. Shown in Figure 19.2 is a graphene sheet with defined roll-up vector *r*. After rolling to form an NT, the two end nodes coincide. The notation we use here is adapted from References 8, 12, and 13. Note that *r* (bold solid line in Figure 19.2) can be expressed as a linear combination of base vectors *a* and *b* (dashed line in Figure 19.2) of the hexagon, i.e.,

$$r = na + mb$$

with *n* and *m* being integers. Different types of NT are thus uniquely defined by the values of *n* and *m,* and the ends are closed with caps for certain types of fullerenes (Figure 19.3).

Three major categories of NT can also be defined based on the chiral angle θ (Figure 19.2) as follows:
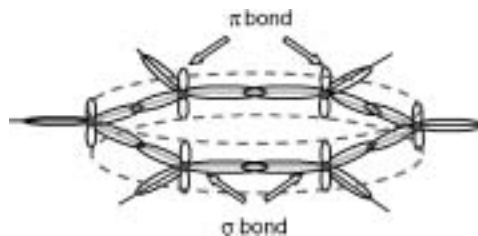

FIGURE 19.1 Basic hexagonal bonding structure for one graphite layer (the *graphene sheet*). Carbon nuclei shown as filled circle, out-of-plane π-bonds represented as delocalized (dotted line), and σ-bonds connect the C nuclei in-plane.
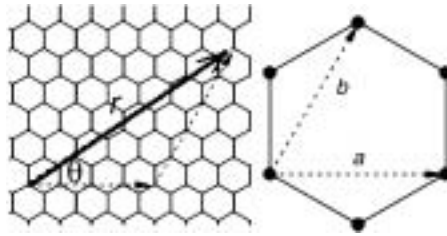
FIGURE 19.2 Definition of roll-up vector as linear combinations of base vectors *a* and *b*.
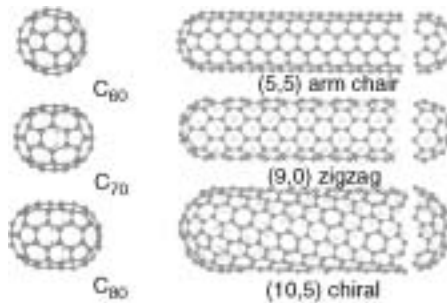

FIGURE 19.3. Examples of zigzag, chiral, and armchair nanotubes and their caps corresponding to different types of fullerenes. (From Dresselhaus MS, Dresselhaus G, and Saito R, (1995), Physics of carbon nanotubes, *Carbon*. 33(7): 883–891. With permission from Elsevier Science.)

$$\theta = 0 \qquad \textit{Zigzag}$$

$$0 < \theta < 30 \qquad \textit{Chiral}$$

$$\theta = 30 \qquad \textit{Arm Chair}$$

Based on simple geometry, the diameter *d* and the chiral angle θ of the NT can be given as:

$$d = 0.783\sqrt{n^2 + nm + m^2}\,\text{Å}$$

$$\theta = \sin^{-1}\left[\frac{\sqrt{3}m}{2(n^2 + nm + m^2)}\right]$$

Most CNTs to date have been synthesized with closed ends. Fujita et al.[14] and Dresselhaus et al.[8,15] have shown that NTs which are larger than (5,5) and (9,0) tubes can be capped. Based on Euler's theorem of polyhedra,[16] which relates the numbers of the edges, faces, and vertices, along with additional knowledge of the minimum energy structure of fullerenes, they conclude that any cap must contain six pentagons that are isolated from each other. For NTs with large radii, there are different possibilities of forming caps that satisfy this requirement. The experimental results of Iijima et al.[17] and Dravid[18] indicate a number of ways that regular-shaped caps can be formed for large-diameter tubes. *Bill*-like[19] and semi-toroidal[17] types of termination have also been reported. Experimental observation of CNTs with open ends can be found in Reference 17.

19.2.1.3 Multi-Walled Carbon Nanotubes and Scroll-Like Structures

The first carbon nanotubes discovered[1] were multi-walled carbon nanotubes (shown in Figures 19.4 and 19.5). Transmission electron microscopy studies on MWCNTs suggest a Russian doll-like structure (nested shells) and give interlayer spacing of approximately ~0.34 nm,[20,21] close to the interlayer separation
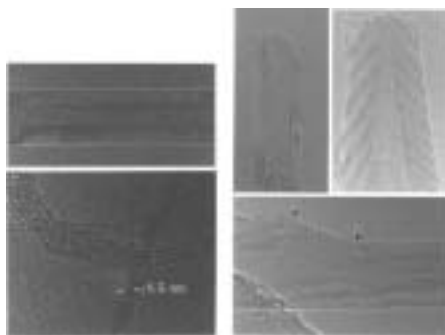
FIGURE 19.4 Top left: High-resolution transmission electronic microscopy (HRTEM) image of an individual MWCNT. The parallel fringes have ~0.34 nm separation between them and correspond to individual layers of the coaxial cylindrical geometry. Bottom left: HRTEM image showing isolated SWCNT as well as bundles of such tubes covered with amorphous carbon. The isolated tubes shown are approximately 1.2 nm in diameter. Top right: HRTEM image showing the tip structure of a closed MWCNT. The fringe (layer) separation is again 0.34 nm. Bottom right: The image of an MWCNT showing the geometric changes due to the presence of five and seven membered rings (position indicated in the image by P for pentagon and H for heptagon) in the lattice. Note that the defects in all the neighboring shells are conformal. (From Ajayan PM and Ebbesen TW, (1997), Nanometer-size tubes of carbon, *Rep. Prog. Phys.* 60(10): 1025–1062. With permission.)
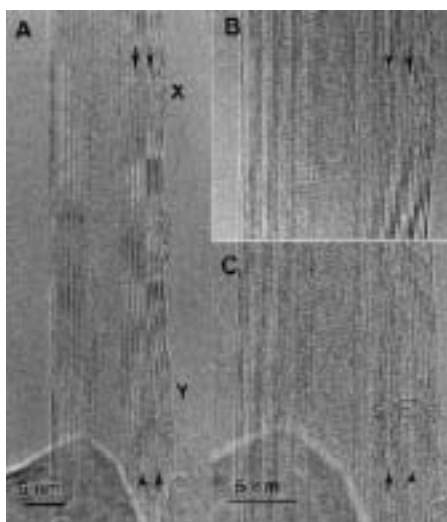

FIGURE 19.5 HRTEM image of an MWCNT. Note the presence of anomalously large interfringe spacings indicated by arrows. (From Amelinckx S, Lucas A, and Lambin P, (1999), Electron diffraction and microscopy of nanotubes, *Rep. Prog. Phys.* 62(11): 1471–1524. With permission.)

of graphite, 0.335 nm. However, Kiang et al.[22] have shown that the interlayer spacing for MWCNTs can range from 0.342 to 0.375 nm, depending on the diameter and number of nested shells in the MWCNT. The increase in intershell spacing with decreased nanotube diameter is attributed to the increased repulsive force as a result of the high curvature. The experiments by Zhou et al.,[21] Amelinckx et al.,[23] and Lavin et al.[24] suggested an alternative *scroll* structure for some MWCNTs, like a cinnamon roll. In fact, both forms might be present along a given MWCNT and separated by certain types of defects. The energetics analysis by Lavin et al.[24] suggests the formation of a scroll, which may then convert into a stable multi-wall structure composed of nested cylinders.

19.2.2 Modeling of Nanotubes as Elastic Materials

19.2.2.1 Elastic Properties: Young's Modulus, Elastic Constants, and Strain Energy

Experimental fitting to mechanical measurements of the Young's modulus and elastic constants of nanotubes have been mostly made by assuming the CNTs to be elastic beams. An extensive summary is given in Section 19.2.2.2. Aside from the use of the beam assumption, there are also experimental measurements that were made by monitoring the response of a CNT under axial load. Lourie and Wagner[27] used micro-Raman spectroscopy to measure the compressive deformation of a nanotube embedded in an epoxy matrix. For SWCNT, they obtained a Young's modulus of 2.8–3.6 TPa, while for MWCNT, they measured 1.7–2.4 TPa.

Yu et al.[28] Presented results of 15 SWCNT bundles under tensile load and found Young's modulus values in the range from 320 to 1470 GPa (mean: 1002 GPa). The stress vs. strain curves are shown in Figure 19.6. Another experiment performed by Yu et al.[29] on the tensile loading of MWCNTs yielded a Young's modulus from 270 to 950 GPa (Figure 19.7). It should be pointed out that concepts such as Young's modulus and elastic constants belong to the framework of continuum elasticity; an estimate of these material parameters for nanotubes implies the continuum assumption. Because each individual SWCNT involves only a single layer of rolled graphene sheet, the thickness t will not make any sense until it is given based on the continuum assumption. In the above-mentioned experiments, it is assumed that the thickness of the nanotube is close to the interlayer distance in graphite, i.e., 0.34 nm.

In the following, we focus on the theoretical prediction of these parameters. Unless explicitly given, a thickness of 0.34 nm for the nanotube is assumed. The earliest attempt to predict Young's modulus
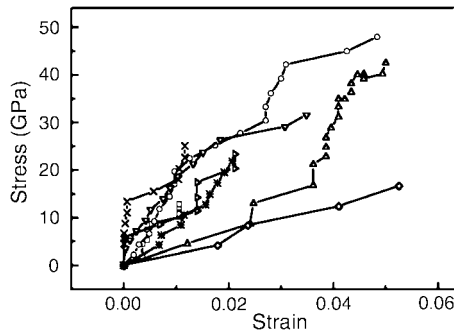
FIGURE 19.6 Eight stress vs. strain curves obtained from the tensile-loading experiments on individual SWCNT bundles. The values of the nominal stress are calculated using the cross-sectional area of the perimeter SWCNTs assuming a thickness of 0.34 nm. (From Yu MF, Files BS, Arepalli S, and Ruoff RS, (2000), Tensile loading of ropes of single-wall carbon nanotubes and their mechanical properties, *Phys. Rev. Lett.* 84(24): 5552–5555. With permission.)

FIGURE 19.7 Plot of stress vs. strain curves for five individual MWCNTs. (Reprinted from Yu MF, Lourie O, Dyer MJ, Moloni K, Kelly TF, and Ruoff RS, (2000), Strength and breaking mechanism of multi-walled carbon nanotubes under tensile load, *Science.* 287(5453): 637–640. © 2000 American Association for the Advancement of Science. With permission.)

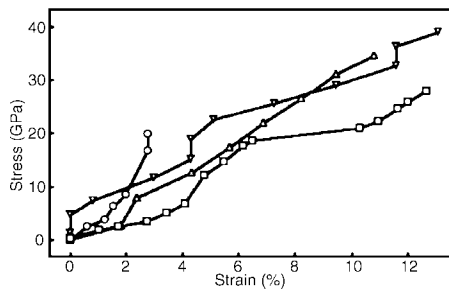theoretically seems to have been made by Overney et al.[30] Using an empirical Keating Hamiltonian with parameters determined from first principles, the structural rigidity of (5,5) nanotubes consisting of 100, 200, and 400 atoms was studied. Although the values are not explicitly given, it was later pointed out by Treacy et al.[31] that the results from Overney et al. implied a Young's modulus in the range of 1.5 to 5.0 TPa. The earliest energetics analysis of CNTs was presented by Tibbetts[32] using elastic theory. He pointed out that the strain energy of the tube is proportional to $1/R^2$ (where R is the radius of the CNT). Ruoff and Lorents[33] suggested the use of elastic moduli of graphite by neglecting the change in the atomic structure when a piece of graphene sheet is rolled into a nanotube. Because the mechanical behavior of single-crystal graphite is well understood, it would be a good approximation to use the in-plane modulus (1.06 TPa of graphite). However, whether such an approximation is good for SWCNTs with small radius was not known.

Robertson et al.[34] examined the energetics and elastic properties of SWCNTs with radii less than 0.9 nm using both Brenner's potential[35] and first-principles total energy methods. Their results showed a consistent linear proportionality to $1/R^2$ of the strain energy, which implies that small deformation beam theory is still valid even for the small radius limit. An elastic constant (C_{11}) close to that of graphite was predicted using the second set of parameters from Brenner's potential;[35] however, it was also shown that the first set of parameters from the same potential results in excess stiffness. Gao et al.[36] carried out a similar study on SWCNTs of larger radius (up to 17 nm) with a potential that is derived from quantum mechanics. A similar linear relation of the strain energy to $1/R^2$ was found. By computing the second derivative of the potential energy, values of Young's modulus from 640.30 GPa to 673.49 GPa were obtained from the MD simulation for closest-packed SWCNTs.

Yakobson et al.[37] compared particular molecular dynamics (MD) simulation results to the continuum shell model[38] and thereby fitted both a value for Young's modulus (~5.5 TPa) and for the effective thickness of the CNTs ($t = 0.066$ nm). Lu[39] derived elastic properties of SWCNTs and MWCNTs using an empirical model in his MD simulation. A Young's modulus of ~1TPa and a shear modulus of ~0.5 TPa were reported based on a simulated tensile test. Lu also found from his simulation that factors such as chirality, radius, and the number of walls have little effect on the value of Young's modulus. Yao et al.[40] used a similar approach but with a different potential model and obtained a Young's modulus of approximately 1 TPa. In addition, they treated the dependence of Young's modulus on both the radius and chirality of the tube. They employed an MD model that included bending, stretching, and torsion terms, and their results showed that the strain in the tube was dominated by the torsional terms in their model. An alternate method is to derive Young's modulus based on the energy-per-surface area rather than per-volume. This was used in the study by Hernandez et al.[41] Using a nonorthogonal tight-binding scheme, they reported a *surface* Young's modulus of 0.42 TPa-nm, which, when converted to Young's modulus assuming the thickness of 0.34 nm, resulted in a value of 1.2 TPa. This value is slightly higher than that obtained by Lu.[39]

Zhou et al.[42] estimated strain energy and Young's modulus based on electronic band theory. They computed the total energy by taking account of all occupied band electrons. The total energy was then decomposed into the rolling energy, the compressing or stretching energy, and the bending energy. By fitting these three values with estimates based on the continuum elasticity theory, they obtained Young's modulus of 5.1 TPa for SWCNT having an effective wall thickness of 0.71 Å. Note that this is close to the estimate by Yakobson et al.[37] because the rolling energy and stretching energy terms were also included in the shell theory that Yakobson et al. used. In addition, the accuracy of the continuum estimate was validated by the derivation of a similar linear relation of the strain energy to $1/R^2$.

Although no agreement has been reached among these publications regarding the value of the Young's modulus at this moment, it should be pointed out that a single value of Young's modulus cannot be uniquely used to describe both tension/compression *and* bending behavior. The reason is that tension and compression are mainly governed by the in-plane σ-bond, while pure bending is affected mainly by the out-of-plane π-bond. It may be expected that different values of elastic modulus should be obtained from these two different cases unless different definitions of the thickness are adopted, and that is one reason that accounts for the discrepancies described above. To overcome this difficulty, a consistent continuum treatment in the framework of crystal elasticity is needed; and we present this in Section 19.2.4.

19.2.2.2 Elastic Models: Beams and Shells

Although CNTs can have diameters only several times larger than the length of a bond between carbon atoms, continuum models have been found to describe their mechanical behavior very well under many circumstances.[43] Indeed, their small size and presumed small number of defects make CNTs ideal systems for the study of the links between atomic motion and continuum mechanical properties such as Young's modulus and yield and fracture strengths. Simplified continuum models of CNTs have taken one of two forms: simple beam theory for small deformation and shell theory for larger and more complicated distortions.

Assuming small deformations, the equation of motion for a beam is:

$$\rho A \frac{\partial^2 u}{\partial t^2} + EI \frac{\partial^4 u}{\partial x^4} = q(x) \tag{19.1}$$

where u is the displacement, ρ is the density, A the cross-sectional area, E Young's modulus, I the moment of inertia, and $q(x)$ a distributed applied load. This equation is derived assuming that displacements are small and that sections of the beam normal to the central axis in the unloaded state remain normal during bending; these assumptions are usually valid for small deformations of long, thin beams, although deviations from this linear theory are probable for many applications of CNTs.[44,45] The natural frequency of the ith mode of vibration is then given by:

$$\omega_i = \frac{\beta_i^2}{L^2} \sqrt{\frac{EI}{\rho A}} \tag{19.2}$$

where β_i is the root of an equation that is dictated by the boundary conditions. For a beam clamped at one end (zero displacement and zero slope) and free at the other (zero reaction forces), this equation is:

$$\cos \beta_i \cosh \beta_i + 1 = 0 \tag{19.3}$$

Thus, the frequencies of the first three modes of vibration of a clamped-free beam can be computed from Equation (19.3) with $\beta_1 \approx 1.875$, $\beta_2 \approx 4.694$, and $\beta_3 \approx 7.855$.

Measurements on vibrating CNTs can therefore be used to estimate Young's modulus. The first experimental measurements of Young's modulus in MWCNTs were made by Treacy et al.,[31] who used a vibrating beam model of a MWCNT to estimate a modulus of about 1.8 TPa. The authors observed TEM images of MWCNTs that appeared to be undergoing thermal vibration, with a mean-square vibration amplitude that was found to be proportional to temperature. Assuming equipartition of the thermal energy among vibrational modes and a hollow cylinder geometry of the tube, this allowed Young's modulus to be estimated based on the measured amplitude of vibration at the tip of the tube. The spread in the experimental data is quite large, with modulus values for 11 tubes tested ranging from 0.40 to 4.15 TPa with a mean value of 1.8 TPa; the uncertainty was ±1.4 TPa. A similar study by Krishnan et al.[46] of SWCNTs found an average modulus of about 1.3–0.4/+0.6 TPa for 27 SWCNTs.

Rather than relying on estimates of thermal vibrations, Poncharal et al.[44] used electromechanical excitation as method to probe the resonant frequencies of MWCNTs. For tubes of small diameter (less than about 12 nm), they found frequencies consistent with a Young's modulus in the range of 1 TPa. However, for larger diameters, the bending stiffness was found to decrease by up to an order of magnitude, prompting the authors to distinguish their measured *bending modulus* (in the range 0.1 to 1 TPa) from the true Young's modulus. One hypothesis put forth for the decrease in effective modulus is the appearance of a mode of deformation, in which a wavelike distortion or *ripple* forms on the inner arc of the bent MWCNT. This mode of deformation is not accounted for by simple beam theory. Liu et al.[45] used a combination of finite element analysis (using the elastic constants of graphite) and nonlinear vibration analysis to show that nonlinearity can cause a large reduction in the effective bending modulus. However, Poncharal et al. reported that there was no evidence of nonlinearity (such as a shift of frequency with
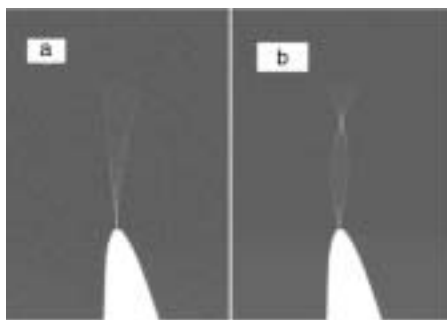
FIGURE 19.8 Scanning electron microscope (SEM) images of electric field-induced resonance of an individual MWCNT at its fundamental resonance frequency (a) and at its second-order harmonic (b).

varying applied force) in their experimental results, which causes some doubt as to whether a large nonlinear effect such as the rippling mode can explain the decrease in bending modulus with increasing tube diameter. Similar resonance excitation of MWCNTs has recently been realized by Yu et al.[47] inside a scanning electron microscope (SEM) (Figure 19.8).

Static models of beam bending can also be used to measure mechanical properties. Wong et al.[48] measured the bending force of MWCNTs using atomic force microscopy (AFM). Assuming the end displacement of an end-loaded cantilevered beam is given by PL3/3EI, where P is the applied force, they fit a Young's modulus of 1.28 ± 0.59 TPa. Salvetat et al.[49,50] measured the vertical deflection vs. the applied force dependence of MWCNT and SWCNT ropes spanning one of the pores in a well-polished alumina nanopore membrane using AFM. They fit values of about 1 TPa for MWCNTs grown by arc discharge, whereas those grown by the catalytic decomposition of hydrocarbons had a modulus 1–2 orders of magnitude smaller.

Govinjee and Sackman[51] studied the validity of modeling MWCNTs with Euler beam theory. They showed the size dependency of the material properties at the nanoscale, which does not appear in the classical continuum mechanics. The beam assumption was further explored by Harik.[52,53] From scaling analysis, he proposed three nondimensional parameters to check the validity of the continuum assumption. The relation between these parameters and MD simulation was discussed. Ru[54–59] has used a shell model to examine the effects of interlayer forces on the buckling and bending of CNTs. It is found that, for MWCNTs, the critical axial strain is decreased from that of a SWCNT of the same outside diameter,[54–56] in essence because the van der Waals forces between layers always cause an inward force on some of the tubes. Note that although the critical axial strain is reduced, the critical axial force may be increased due to the increased cross-sectional area. The phenomenon is also seen when the CNT is embedded in an elastic matrix.[57,58] Ru uses a similar analysis to treat the buckling of columns of SWCNTs arranged in a honeycomb pattern.[59]

19.2.2.3 Elastic Buckling and Local Deformation of NT

Experiments have shown a few cases of exceptional tensile strength of carbon nanotubes (see Section 19.2.3 Strength of Nanotubes). In addition, experiment and theory have addressed structural instability for tubes under compression, bending, or torsion. Buckling can occur in both the axial and transversal direction. Buckling can also occur in the whole structure or locally. Analyses based on continuum theory and the roles of interlayer potential are discussed in Section 19.4.2.2.

Yakobson et al.[37,43] modeled buckling of CNTs under axial compression and used the Brenner potential in their MD simulation. Their simulation also showed four *snap-throughs* during the load process, resulting from instability. The first buckling pattern starts at a nominal compressive strain of 0.05. Buckling due to bending and torsion was demonstrated in References 37, 60, 61, and 62. In the case of bending, the pattern is characterized by the collapse of the cross-section in the middle of the tube, which confirms the experimental observations by Iijima et al.[63] and Ruoff et al.[64,65] using HRTEM

FIGURE 19.9 (a) Buckling of SWCNT under bending load. (b) Buckling of SWCNT under torsional load.

and by Wong et al.[48] using AFM. When the tube is under torsion, flattening of the tube, or equivalently a collapse of the cross-section, can occur due to the torsional load. Shown in Figure 19.9 are the simulation results of buckling patterns using a molecular dynamics simulation code developed by the authors. Falvo et al.[66] bent MWCNTs by using the tip of an AFM. They showed that MWCNTs could be bent repeatedly through large angles without causing any apparent fracture in the tube. Similar methods were used by Hertel et al.[67] to buckle MWCNTs due to large bending. Lourie et al.[68] captured the buckling of SWCNTs under compression and bending by embedding them into a polymeric film. Unlike the single kink seen by Iijima et al.,[63] the buckling pattern under bending was characterized by a set of local rippling modes.

The radial deformability for tubes has also been studied. Ruoff et al.[69] first studied radial deformation between adjacent nanotubes (Figure 19.10). Partial flattening due to van der Waals forces was observed in TEM images of two adjacent and aligned MWCNTs along the contact region. This was the first observation that CNTs are not necessarily perfectly cylindrical. Indeed, in an anisotropic physical environment, all CNTs are likely to be, at least to some degree, not perfectly cylindrical due to mechanical deformation. Tersoff and Ruoff[70] studied the deformation pattern of SWCNTs in a closest-packed crystal and concluded that rigid tubes with diameters smaller than 1 nm are less affected by the van der Waals attraction and hardly deform. But for diameters over 2.5 nm, the tubes flatten against each other and form a honeycomb-like structure. This flattening of larger diameter SWCNTs could have a profound effect on factors such as storage of molecular hydrogen in SWCNT crystals composed of such larger diameter tubes, if they can be made, because the interstitial void space is dramatically altered. Lopez et al.[70a] have reported the observation, with HRTEM, of polygonized SWCNTs in contact.
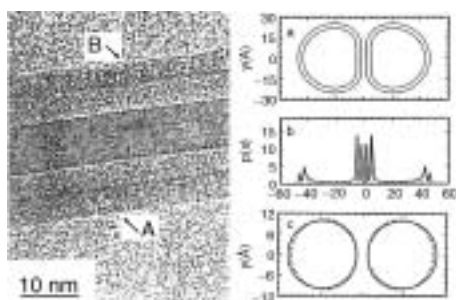

FIGURE 19.10 Left: HRTEM image of two adjacent MWCNTs *a* and *b*. Nanotube *a* has 10 fringes, and nanotube *b* has 22. The average interlayer spacings for inner layers and outer layers belonging to MWCNT *a* are 0.338 nm and 0.345 nm, respectively. For MWCNT *b*, these are 0.343 nm and 0.351 nm, respectively. The 0.07 and 0.08 nm differences, respectively, are due to the compressive force acting in the contact region, and the deformation from perfectly cylindrical shells occurring in both inner and outer portions of each MWCNT. Right from top to bottom: (a) Calculated deformation resulting from van der Waals forces between two double-layered nanotubes. (b) Projected atom density from (a). The projected atom density is clearly higher in the contact region, in agreement with the experimental observation of the much darker fringes in the contact region as compared to the outer portions of MWCNTs *a* and *b*. (c) Calculated deformation for adjacent single-layer nanotubes. (From Ruoff RS, Tersoff J, Lorents DC, Subramoney S, and Chan B, (1993), Radial deformation of carbon nanotubes by van der Waals forces, *Nature*, 364(6437): 514–516. With permission.)

Chopra et al.[71] observed fully collapsed MWCNTs with TEM and showed that the collapsed state can be energetically favorable for certain types of CNTs having a certain critical radius and overall wall thickness. Benedicts et al.[72] Proposed the use of the ratio of mean curvature modulus to the interwall attraction of graphite to predict whether the cross-section will collapse and applied their model for a collapsed MWCNT observed in TEM by the same authors. In addition, their experiment also provided the first microscopic measurement of the intensity of the inter-shell attraction.

Hertel et al.[73] and Avouris et al.[74] studied the van der Waals interaction between MWCNTs and a substrate by both experiment (using AFM) and simulation. They found that radial and axial deformations of the tube may lead to a high energy binding state, depending on the types of CNTs present. Fully or partially collapsed MWCNTs on surfaces have also been reported by Yu et al.,[75,76] and their work included a careful analysis of the mechanics of tubes when in contact with surfaces. Lordi and Yao[77] simulated the radial deformation of CNTs due to a local contact and compared the model structures with experimental images of CNTs in contact with nanoparticles. With simulation of both SWCNT and MWCNT up to the radius of a (20, 20) nanotube (13.6 Å), no collapse due to local contact was reported. Instead, the radial deformation was found to be reversible and elastic. Based on these results, they suggested that mechanically cutting a nanotube should be rather difficult, if not impossible.

Gao et al.[36] carried out an energetics analysis on a wide range of nanotubes. They showed the dependence of geometry on the radius of the tube. To be more specific, a circular cross-section is the stable configuration for a radius below 1 nm, in line with the prior results obtained by Tersoff and Ruoff[70] mentioned above. If the radius is between 1 and 2 nm, both circular and collapsed forms are possible. Beyond 3 nm the SWCNT tends to take the collapsed form. However, we should note that the treatment by Gao et al. is of isolated SWCNTs, and their results would be modified by contact with a surface (which might accelerate collapse. Yu et al.,[75,76] on the other hand, as already demonstrated by Tersoff and Ruoff,[70] showed that completely surrounding a SWCNT by similar sized SWCNTs might stabilize against complete collapse.

It is interesting to speculate whether larger diameter SWCNTs would *ever* remain completely cylindrical in any environment. A nearly isotropic environment would be a liquid comprised of small molecules, or perhaps a homogeneous polymer comprised of relatively small monomers. However, because the CNTs have such small diameters, fluctuations are present in the environment on this length scale, locally destroying the time-averaged isotropicity present at longer length scales, may trigger collapse. Alternatively, if full collapse does not occur, the time-averaged state of such a CNT in a (time-averaged) isotropic environment might be perfectly cylindrical. Perhaps for this reason, CNTs might be capable of acting as probes of minute fluctuations in their surrounding (molecular) environment.

Shen et al.[78] conducted a radial indentation test of ~10 nm diameter MWCNTs with scanning probe microscopy. They observed deformability (up to 46%) of the tube and resilience to a significant compressive load (20 μN). The radial compressive elastic modulus was found to be a function of compressive ratios and ranged from 9.0 to 80.0 GPa.

Yu et al.[79] Performed a nanoindentation study by applying compressive force on individual MWCNTs with the tip of an AFM cantilever in tapping-mode (Figure 19.11) and demonstrated a deformability similar to that observed by Shen et al. They estimated the effective elastic modulus of a range of indented MWCNTs to be from 0.3 GPa to 4 GPa by using the Hertzian contact model. The reader should note that the difference between this effective elastic modulus and the elastic modulus discussed in Section 19.2.2.1 is that the effective modulus refers to the elastic response to deformation of an anisotropic indentation load applied in the radial direction. We thus also distinguish this type of load from the isotropic load that could, for example, be applied by high pressure for CNTs suspended in a liquid pressure medium, which is more appropriately referred to as *isotropic radial compressive loading*. Yu et al.[76] provided further energetics analysis on MWCNTs that are in configurations of partial or full collapse, or collapsed combined with a twist. They showed that interlayer van der Waals interactions play an important role in maintaining the collapsed configuration.

Chesnokov et al.[80] observed remarkable reversible volume compression of SWCNTs under quasi-hydrostatic pressure up to 3 GPa and obtained a volume compressibility of 0.0277 GPa^{-1}, which suggests the use of CNT as energy-absorbing materials. The volume compressibility of SWCNTs having a diameter
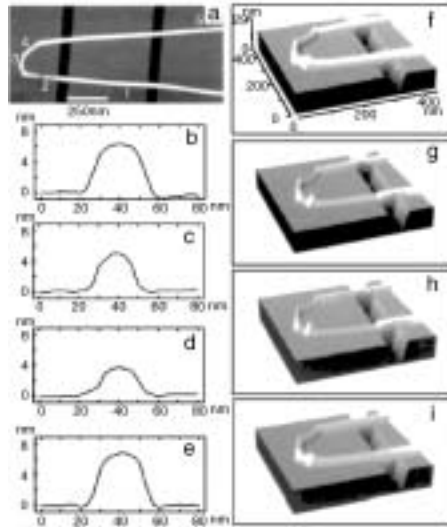
FIGURE 19.11 Deformability of an MWCNT deposited on a patterned silicon wafer as visualized with tapping-mode AFM operated far below mechanical resonance of a cantilever at different set points. The height in this and all subsequent images was coded in grayscale, with darker tones corresponding to lower features. (a) Large-area view of an MWCNT bent upon deposition into a hairpin shape. (b)–(e) Height profiles taken along the thin marked line in (a) from images acquired at different set-point (S/S_0) values: (b) 1.0; (c) 0.7; (d) 0.5; (e) 1.0. (f)–(i) Three-dimensional images of the curved region of the MWCNT acquired at the corresponding set-point values as in (b)–(e). (From Yu MF, Kowalewski T, and Ruoff RS, (2000), Investigation of the radial deformability of individual carbon nanotubes under controlled indentation force, *Phys. Rev. Lett.* 85(7): 1456–1459. With permission.)

of 1.4 nm under hydrostatic pressure was also studied by Tang et al.[81] by *in situ* synchrotron X-ray diffraction. The studied SWCNT sample, which consisted primarily of SWCNT bundles and thus not individual or separated SWCNTs, showed linear elasticity under hydrostatic pressure up to 1.5 GPa at room temperature with a compressibility value of 0.024GPa^{-1}, which is smaller than that of graphite (0.028GPa^{-1}). However, the lattice structure of the SWCNT bundles became unstable for pressure beyond ~4 GPa and was destroyed upon further increasing the pressure to 5 GPa.

A very subtle point that comes into the picture is the effect of interlayer interactions when CNTs collapse. This effect can produce some results that cannot be described by traditional mechanics. For instance, Yu et al.[82] observed fully collapsed MWCNT ribbons in the twisted configuration with TEM. One such cantilevered MWCNT ribbon had a twist present in the freestanding segment (Figure 19.12a). Such a configuration cannot be accounted for by elastic theory because no external load (torque) is present to hold the MWCNT ribbon in place and in the twisted form. However, it is known that the difference of approximately 0.012 eV/atom in the interlayer binding energy of the *AA* and the *AB* stacking configurations (Figure 19.12d, c) exists for two rigid graphitic layers spaced 0.344 nm apart. The analysis by Yu et al.[82] suggests that the elastic energy cost for the twist formation of this particular CNT ribbon can be partially compensated by achieving more favorable atomic registry. The observation of the existence of this freestanding twist in the ribbon thus suggests that an energy barrier exists to keep the twisted ribbon from untwisting. The mechanics analysis performed suggests that this twisted structure is metastable. More details on the modeling of interlayer interaction with the account of this registry effect are presented in Section 19.4.2.2.

As a brief summary, compared with their high rigidity in the axial direction, CNTs are observed to be much more compliant in the radial direction. Thus a CNT readily takes the form of a partially or fully collapsed nanoribbon when the radius and wall thickness are in particular ranges, when either isolated in free space, or in contact with a surface. A CNT may also locally flatten when surrounded, as occurs, for example, in the SWCNT bundles.
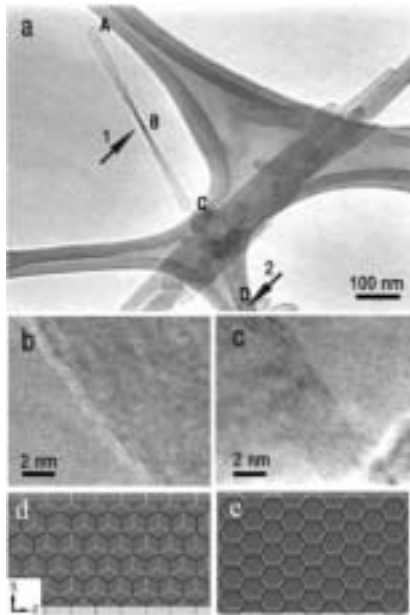
FIGURE 19.12 A free-standing twisted MWCNT ribbon. (a) A TEM image of this ribbon anchored on one end by a carbon support film on a lacy carbon grid. Arrows point to the twists in the ribbon. (b) and (c) Eight resolved fringes along both edges of the ribbon imaged near the anchor point. (d) A schematic depicting the AB stacking between armchair CNT shells (the two layers are the layer having brighter background and black lattices vs. the layer having darker background and white lattices). The AB stacking can be achieved by shifting the layer positions along the *x* direction that is perpendicular to the long axis of the MWCNT. (e) A schematic depicting the lattice alignment between the zigzag CNT shells by allowing the relative shifting of the layers along the *x* direction. The AB stacking is not possible; only AA stacking or other stacking (as shown in the schematic) is possible. (From Yu MF, Dyer MJ, Chen J, Qian D, Liu WK, and Ruoff RS, (2001), Locked twist in multi-walled carbon nanotube ribbons, *Phys. Rev. B, Rapid Commn*. 64: 241403R. With permission.)

19.2.3 Strength of Nanotubes

The strength of a CNT will likely depend largely on the distribution of defects and geometric factors. In the case of geometric factors, buckling due to compression, bending, and torsion has been discussed in Section 19.2.2.3. Note that even in these loading cases, it is still possible for plastic yielding to take place due to highly concentrated compressive force. Another geometric factor is the interlayer interaction in the case of MWCNTs and bundles of CNTs.

19.2.3.1 Strength Due to Bond Breaking or Plastic Yielding

Unlike bulk materials, the density of the defects in nanotubes is presumably less; and therefore the strength is presumably significantly higher at the nanoscale. The strength of the CNT could approach the theoretical limit depending on the synthesis process. There are several major categories of synthesis method: carbon evaporation by arc current discharge,[1,83,84] laser ablation,[85,86] or chemical vapor deposition (CVD).[87–89] MWCNTs produced by the carbon plasma vapor processes typically possess higher quality in terms of defects than those produced by the shorter time, lower temperature CVD processes. However, it is not known at this time whether the SWCNTs produced by the laser ablation method, for example, are better than those produced by CVD growth from preformed metal catalyst particles present on surfaces. It is thus worth mentioning the essential role of various catalysts in the production of SWCNTs.[90]

There have been few experimental reports on testing the tensile strength of nanotubes. The idea is simple but seems rather difficult to implement at this stage. Yu et al.[28] were able to apply a tensile load on 15 separate SWCNT bundles and measure the mechanical response (Figure 19.13). The maximum tensile strain they obtained was 5.3%, which is close to the theoretical prediction made by Nardelli et al.[91]
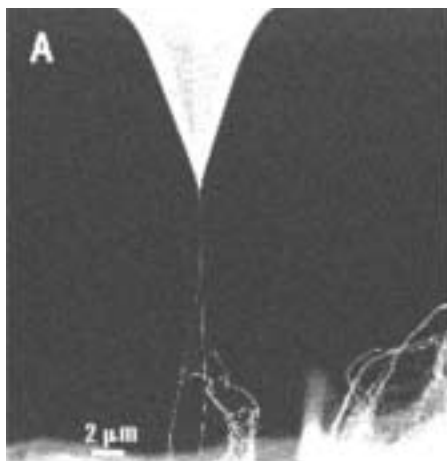
FIGURE 19.13 SEM image of a tensile-loaded SWCNT bundle between an AFM tip and a SWCNT buckytube paper sample. (From Yu MF, Files BS, Arepalli S, and Ruoff RS, (2000), Tensile loading of ropes of single-wall carbon nanotubes and their mechanical properties, *Phys. Rev. Lett.* 84(24): 5552–5555. With permission.)

The *average* SWCNT tensile strength for each bundle ranged from 13 to 52 GPa, calculated by assuming the load was applied primarily on the SWCNTs present at the perimeter of each bundle.

Tensile loading of 19 individual MWCNTs was reported by Yu et al.,[29] (Figure 19.14) and it was found that the MWCNTs broke in the outermost layer by a "sword-in-sheath" breaking mechanism with tensile strain at break of up to 12%. The tensile strength of this outermost layer (equivalent to a large-diameter SWCNT) ranged from 11 to 63 GPa.

By laterally stretching suspended SWCNT bundles fixed at both ends using an AFM operated in lateral force mode, Walters et al.[92] were able to determine the maximum elongation of the bundle and thus the breaking strain. The tensile strength was thus estimated to be 45±7 GPa by assuming a Young's modulus of 1.25TPa for SWCNT. The tensile strength of very long (~2mm) ropes of CVD-grown aligned MWCNTs was measured to be 1.72±0.64 GPa by Pan et al.[93] using a modified tensile testing apparatus, by constantly monitoring the resistance change of the ropes while applying the tensile load. The much lower value they obtained is perhaps to be expected for CVD-grown MWCNTs, according to the authors. But another factor may be the much longer lengths tested, in that a much longer CNT may be more likely to have a critical concentration of defects that could lead to failure present somewhere along their length. The dependence of fracture strength on length has not yet been experimentally addressed.

Another way of applying tensile load is to use the load transferred by embedding the CNTs in a matrix material. Wagner et al.[94] observed fragmentation in SWCNTs using this method and reported a tensile
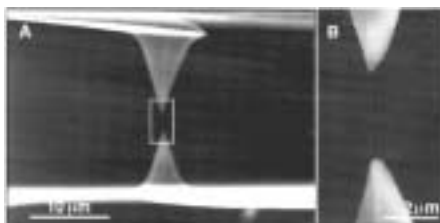
FIGURE 19.14 Tensile loading of individual MWCNTs. (A) An SEM image of an MWCNT attached between two AFM tips. (B) Large magnification image of the indicated region in (A) showing the MWCNT between the AFM tips. (Reprinted from Yu MF, Lourie O, Dyer MJ, Moloni K, Kelly TF, and Ruoff RS, (2000), Strength and breaking mechanism of multi-walled carbon nanotubes under tensile load, *Science.* 287(5453): 637–640. ©2000 American Association for the Advancement of Science. With permission.)

strength of 55 GPa. Tensile strength measurements on a resin-based SWCNT composite were performed by Li et al.[95] Through a treatment that includes modeling the interfacial load transfer in the SWCNT–polymer composite, the tensile strength of the SWCNTs was fit to an average value of ~22 GPa. A compression test of the CNT has been performed by Lourie et al.[68] in which, in addition to the buckling mode that is mentioned in Section 19.2.2.3, they also observed plastic collapse and fracture of thin MWCNTs. The compressive strength and strain corresponding to these cases were estimated to be approximately 100–150 GPa and > 5%, respectively.

Theoretical prediction of CNT strength has emphasized the roles of defects, loading rate, and temperature using MD simulation. Yakobson et al.[37,43,61,96] Performed a set of MD simulations on the tensile loading of nanotubes. Even with very high strain rate, nanotubes did not break completely in half; and the two separated parts were instead connected by a chain of atoms. The strain and strength from these simulations are reported to be 30% and 150 GPa, respectively. The fracture behavior of CNT has also been studied by Belytschko et al.[97] using MD simulations. Their results show moderate dependence of fracture strength on chirality (ranges from 93.5 GPa to 112 GPa), and fracture strain between 15.8% and 18.7% were reported. In these simulations, the fracture behavior is found to be almost independent of the separation energy and to depend primarily on the inflection point in the interatomic potential. The values of fracture strains compare well with experimental results by Yu et al.[29]

A central theme that has been uncovered by quantum molecular dynamics simulations of plastic yielding in CNTs is the effect of pentagon/heptagon (or 5/7) defects (Figure 19.15, where the bond rotation leading to the 5–7–7–5 defect initially formed. This is referred to as the *Stone–Wales bond-rotation*[8]) which, for certain types of SWCNTs and at sufficiently high temperature, can lead to plastic yielding.[96] Nardelli et al.[99] studied the mechanism of strain release under tensile loading using both classical and quantum molecular dynamics (MD and QMD). They found that in the case of tension, topological defects such as the 5–7–7–5 defect tend to form when strain is greater than 5% in order to achieve the relaxation of the structure. At high temperature (which for these carbon systems means temperatures around 2000 K) the 5–7–7–5 defect can, for a subset of the SWCNT types, separate into two 5,7 pairs that can glide with respect to each other. Nardelli et al.[91] observed the ductile–to–brittle failure transition as a function of both temperature and strain in their MD simulation. Generally, high strain (15%) and low temperature (1300K) lead to brittle behavior (crack extension or separation), while low strain (3%) and high temperature (3000K) make nanotubes more ductile (dislocation motion without cracking). The reader is reminded of the short time scale of these simulations.

Srivastava et al.[100] demonstrated that a local reconstruction leading to formation of sp^3 bonds can occur under compressive load, and obtained a compressive strength of approximately 153 GPa. Wei
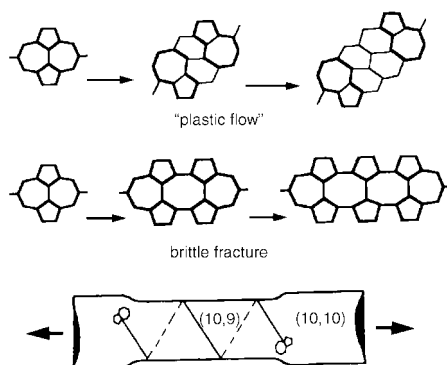
FIGURE 19.15 The 5–7–7–5 dislocation evolves either as a crack (brittle cleavage) or as a couple of dislocations gliding away along the spiral slip plane (plastic yield). In the latter case, the change of the nanotube chirality is reflected by a step-wise change of diameter and by corresponding variations of electrical properties. (From Yakobson BI, 1997, in *Recent Advances in the Chemistry and Physics of Fullerenes and Related Materials*, Kadish KM (Ed.), Electrochemical Society, Inc., Pennington, NJ, 549. With permission of Elsevier Science.)

et al.[101] and Srivastava et al.[102] demonstrated that finite temperature (starting from 300 K) can help the nanotube to overcome a certain energy barrier to achieve plastic deformation. They conducted a similar study of the temperature effect using MD with compressive loading at 12% strain and observed both the formation of sp^3 bonds (at 300K) and 5/7 defects (1600K) for an (8,0) tube. In addition, it was reported[102] that a slower strain rate tends to trigger plastic yield. The conclusion is very similar to the one obtained by Nardelli et al.,[99] but a subtle question is whether the ductile behavior is due to strain or strain rate.

A detailed analysis on the mechanism of defects and dislocation is presented by Yakobson.[61,103] It was shown that the glide direction of the 5/7 defects is dependent on the chirality of the nanotube and, consequently, an irreversible change in the electronic structure also takes place in the vicinity of the chirality change (an armchair tube changes from metallic to semiconducting). Similar conclusions about the effect of strain release on the electronic structure of the tube have been given by Zhang et al.[104] Zhang et al. also observed the dependence of the elastic limit (the onset of plastic yielding) on the chirality of the tube: for the same radius, an (n,0), thus zigzag, tube has nearly twice the limit of an (n,n), thus armchair, tube. This is due mostly to the different alignment of the defects with the principle shear direction. The compressive strength they obtained ranged from 100 to 170 GPa. Another mechanism of defect nucleation is described by Zhang and Crespi,[105] where plastic flow can also occur due to the spontaneous opening of double-layered graphitic patches.

As a brief summary, experimental and simulation efforts have recently been undertaken to assess the strength of CNT. A major limitation for simulation currently is the small time scale that current MD methods can address, much shorter than are actually implemented in experiment. Implicit methods and bridging scale methods show promise in alleviating this difficulty.

19.2.3.2 Strength Due to Interlayer Sliding

Most synthesized nanotubes are either randomly agglomerated MWCNTs or bundles of closest-packed SWCNTs.[85,90] The SWCNTs have a narrow diameter distribution as synthesized and are consequently typically tightly and efficiently packed in bundles.[86,106] The tensile response of SWCNT nanoropes has been measured by Yu et al.;[28] tensile loading of individual MWCNTs was presented by Yu et al.[29] They demonstrated that MWCNTs that are mounted by attachment to the outermost shell and then loaded in tension break in the outermost shell, thus indicating negligible load transfer to the inner shells. This limits the potential of MWCNTs for structural applications — in terms of exhibiting high stiffness and strength in tension, they are a victim of their own high perfection of bonding, as there is evidently no covalent bonding between the nested shells and thus little or no load transfer from the outer shell to the inner shells.

The weak intershell interaction has been measured by Yu et al.[11] (Figure 19.16) and estimated by Cumings and Zettl.[107] In the study of *shell-sliding* of two MWCNTs by Yu et al.,[11] direct measurement of the dependence of the pulling force on the contact length between the shells was performed, and the shear strength between the outermost shell and the neighboring inner shell for two MWCNTs was found to be 0.08 and 0.3 Mpa, respectively. These values are on the low end of the experimental values of the shear strength in graphite samples,[108] thus emphasizing the weak intershell interactions in high-quality, highly crystalline MWCNTs, similar to the type originally discovered by Iijima.[1] Cumings et al.[107] demonstrated inside a TEM that a *telescope process* can be repeated on the MWCNTs that they tested up to 20 times without causing any apparent damage. (The reader should note that assessment of damage at the nanoscale is quite challenging. Here, the authors simply note that there was no apparent change as imaged by high-resolution TEM.) These two studies motivate contemplation of the possibility of a nanoscale-bearing system of exceptional quality. The shear strengths corresponding to static friction and dynamic friction were estimated to be 0.66 and 0.43 MPa, respectively.[107] These values are on the same order as what Yu et al. obtained by experimental measurement.[11]

For SWCNT bundles, there have been theoretical estimates that, in order to achieve load transfer so that the full bundle cross-section would be participating in bearing load up to the intrinsic SWCNT breaking strength (when loading has, for example, been applied only to those SWCNTs on the perimeter), the SWCNT contact length must be on the order of 10 to 120 microns.[109,110] This is much longer than the typical length of individual SWCNTs in such bundles,[111,112] where mean length values on the order
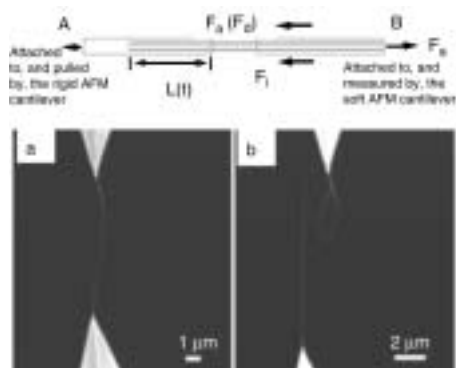
FIGURE 19.16 The forces involved in the shell-sliding experiment can be described by $F_a = F_s + F_i = \pi d\tau L(t) + F_i$, where F_a is the applied pulling force as a function of time, τ is the shear strength, L is the contact length, d the shell diameter, and F_i is a diameter-dependent force originating from both surface tension and edge effects. SEM images showing the sword-in-sheath breaking mechanism of MWCNTs. (a) An MWCNT attached between AFM tips under no tensile load. (b) The same MWCNT after being tensile loaded to break. Notice the apparent overall length change of the MWCNT fragments after break compared to the initial length and the curling of the top MWCNT fragment in (b). (From Yu MF, Yakobson BI, and Ruoff RS, (2000), Controlled sliding and pull-out of nested shells in individual multi-walled carbon nanotubes, *J. Phys. Chem. B.* 104(37): 8764–8767. With permission.)

of a few hundred nanometers have been obtained. This means that load transfer in a parallel bundle containing such relatively short SWCNTs is very likely to be very small and thus ineffective. Quantitative analysis of actual dynamics by modeling using MD requires an interlayer potential that precisely accounts for the interlayer interaction as a function of relative slide position as well as correct incorporation of thermal effects. A general discussion of interlayer potentials is presented in Section 19.3.2.2.

19.2.4 Elastic Properties Based on Crystal Elasticity

It now can be seen that all the theoretical studies presented in Section 19.2.2.1 have either failed to distinguish between the case of infinitesimal strain and finite strain or have directly applied the result at infinitesimal strain to the case of finite strain. In this section, the elastic properties of CNTs at finite strain will be discussed. The significance of this study is obvious from the various deformation patterns due to the load. Of particular interest is the derivation of the elastic constants based on a known atomic model, from either an empirical expression or *ab initio* calculation.

Early attempts to derive elastic constants based on the potential energy of a crystal system were made by Born and Huang.[113] In their treatment, the potential energy was expressed as a function of the displacements of atoms. Because the formulation does not generally guarantee the rotational invariance, the so-called Born–Huang conditions were proposed. Keating[114–117] showed the inconsistencies in the Born–Huang conditions and stated that the potential energy of the crystal system can be alternatively expressed in terms of the variables that intrinsically preserve the invariance property. Based on Brugger's thermodynamic definition[118] of elastic constants, Martin[119–121] derived elastic constants for a crystal system in which the energy density is a sum of the contributions from many-body interactions. Martin's approach is in fact a hyperelastic approach because the energy density was considered as a function of the Lagrangian strain. Based on the embedded-atom method (EAM),[122,123] Tadmor et al.[124,125] derived the corresponding elasticity tensor at finite deformation in their quasicontinuum analysis. Friesecke and James[126] proposed another approach of bridging between continuum and atomic structure, with emphasis on nanostructures in which the size of one dimension is much larger than the other.

The essence of hyperelasticity has been discussed in detail in References 127 through 129. The advantage of the hyperelastic formulation is that it is inherently material frame-invariant; therefore, no special treatment is needed in the large deformation computation.

As a brief summary, if the energy density W of the material is known, the relation between the nominal stress P and the deformation gradient F is given as:[127]

$$P = \frac{\partial W}{\partial F^T} \text{ or } P_{ij} = \frac{\partial W}{\partial F_{ji}} \tag{19.4}$$

In Equation (19.4), F_{ij} $\partial x_i/\partial X_j$, in which x and X are, respectively, the spatial and material coordinates. The lower-case subscript denotes the dimension. An equivalent form is to express in terms of the second Piola–Kirchhoff stress S (referred to as 2nd PK stress) and Lagrangian strain E, i.e.,

$$S = \frac{\partial W}{\partial E} \text{ or } S_{ij} = \frac{\partial W}{\partial E_{ij}} \tag{19.5}$$

Correspondingly, there are two sets of elasticity tensors:

$$C^{PF} = \frac{\partial^2 W}{\partial F^T \partial F^T} \text{ or } C^{PF}_{ijkl} = \frac{\partial^2 W}{\partial F_{ji} \partial F_{lk}} \tag{19.6}$$

and

$$C^{SE} = \frac{\partial^2 W}{\partial E \partial E} \text{ or } C^{SE}_{ijkl} = \frac{\partial^2 W}{\partial E_{ij} \partial E_{kl}} \tag{19.7}$$

C^{PF} and C^{SE} are generally referred to as the *first elasticity tensor* and the *second elasticity tensor*, respectively. Their difference is mainly governed by different stress and strain measures that are involved in their definition. It can be shown that the two elasticity tensors are related by

$$C^{PF}_{ijkl} = C^{SE}_{imnk} F_{jm} F_{\ln} + S_{ik} \delta_{lj} \tag{19.8}$$

where δ_{ij} is the Kronecker delta.

In addition, there are also the *third elasticity tensor* $C^{(3)}_{ijkl}$ and *fourth elasticity tensor* $C^{(4)}_{ijkl}$. The *third elasticity tensor* relates the velocity gradient $L_{ij} = \partial v_i/\partial x_j$ to the push-forward of the rate of nominal stress P, i.e.,

$$F_{ir}\dot{P}_{rj} = C^{(3)}_{ijkl} L^T_{kl} \tag{19.9}$$

The fourth elasticity tensor is the spatial form of the second elasticity tensor and is defined by

$$C^{(4)}_{ijkl} = F_{im} F_{jn} F_{kp} F_{lq} C^{SE}_{mnpq} \tag{19.10}$$

It can be shown that the fourth elasticity tensor is essentially the tangent moduli in the spatial form and it relates the convective rate of the Kirchhoff stress to the rate of deformation:

$$D_{ij} = \frac{1}{2}(L_{ij} + L_{ji}) \tag{19.11}$$

The convected rate of Kirchhoff stress corresponds to the mathematical concept of Lie derivatives, which consistently define the time derivatives of tensors. Therefore, the fourth elasticity tensor plays an important role in maintaining objectivity during stress update and material stability analysis. More detailed descriptions can be found in Chapters 5 and 6 in the book by Belytschko, Liu, and Moran.[127]

To apply hyperelasticity to the crystal system, the Cauchy–Born rule[124,130,131] must be imposed. This rule assumes that the local crystal structure deforms homogeneously and that the mapping is characterized by

the deformation gradient F. With this assumption, we can apply the Equations (19.4) to (19.7) to specific atomic models of the nanotube system. We consider the undeformed state of the CNT to be the same as that of a graphene sheet and adopt the classical Tersoff–Brenner model.[35,132–135] The empirical equation is given as follows:

$$\Phi_{ij} = \Phi_R(r_{ij}) - \bar{B}_{ij}\Phi_A(r_{ij}) \tag{19.12}$$

in which i, j are the indices for carbon atoms. Φ_R and Φ_A represent the repulsive and attractive parts of the potential, respectively. The effect of bonding angle is considered in the term $\bar{B}_{ij}$. The detailed expression for each individual term looks a little tedious due to the consideration of many-body effects. Readers may consult the original paper[35] for parameters and functional forms.

The basic element of the graphite structure is a single hexagon, with each side of the hexagon a result of the covalent bond due to sp^2 hybridization described in Section 19.2.1.1. Because each bond is also shared by the other neighboring hexagon, the total bonding energy Φ for one hexagon can be given as half of the summation of the bonding energy from all six covalent bonds. This summation can be further reduced if the symmetry is considered. The energy density, due to the fact that the single layer of graphite is only a result of repeating the hexagon structure, is given as:

$$W = \frac{\Phi}{A_0} \tag{19.13}$$

with $\Phi = \sum_{l=1}^{3} \Phi_l$. In Equation (19.13), A_0 is the area of the undeformed hexagon and Φ_I is the bond energy for the Ith bond. According to Brenner's potential:

$$\Phi_I = \Phi_I(r^1, r^{l1}, r^{l2}, \cos\theta^{l1}, \cos\theta^{l2}) \tag{19.14}$$

in which $I1$ and $I2$ refer to the neighboring bonds of bond I and Φ_I is a function of bond lengths and bonding angles. Note that W is in fact the surface energy density of the system, and the thickness term t is not needed because we are dealing with a single layer of graphite. As a result of this, the units for the stress and elasticity tensors are different from those used in the conventional procedures. According to Section 19.2.1.2, the deformation gradient is determined by the roll-up vector, which is composed of the direction and length of rolling operation and the subsequent mechanical relaxation after rolling. These effects are embedded in the deformation gradient F_{ij}. The relaxed structure can be obtained from MD simulation for a specific type of CNT. We have evaluated elastic constants and Young's modulus for various types of nanotubes. For the purpose of comparison, we have converted the elastic constants and Young's modulus by assuming an artificial thickness $t = 0.34$ nm. With this assumption, the second elasticity tensor in the hyper-elastic formulation is given as:

$$C_{ijkl}^{SE} = \frac{\partial S_{ij}}{\partial E_{kl}} \tag{19.15a}$$

with

$$S_{ij} = \frac{1}{A_0 t}\sum_{I=1}^{3}\left(\sum_{N=1,I1,I2}\frac{\partial\Phi}{\partial r^N}\frac{\partial r^N}{\partial E_{ij}} + \sum_{N=1,2}\frac{\partial\Phi_I}{\partial\cos\theta_{IN}}\frac{\partial\cos\theta_{IN}}{\partial E_{ij}}\right) \tag{19.15b}$$

We view the concept of Young's modulus as a tangent modulus that is defined in the deformed configuration (the CNT as a result of rolling the graphene sheet.). Therefore it can be calculated from both the above equation and the expression for the fourth elasticity tensor (Equation (19.10)). The standard definition of Young's modulus is the ratio of the uniaxial stress exerted on a thin rod (a nanotube, in our case) to the resulting normal strain in the same direction. If we define 1 to be the axial direction

and 2 and 3 to be the other two orthogonal directions, then it can be shown that the relation between Young's modulus Y and the elastic constants is given as:

$$Y = \frac{C_{11}C_{23}^2 + C_{12}C_{13}^2 + C_{33}C_{12}^2 - C_{11}C_{22}C_{33} - 2C_{12}C_{13}C_{23}}{C_{23}^2 - C_{22}C_{33}} \tag{19.16a}$$

$$C_{ijkl} = F_{im}F_{jn}F_{kp}F_{lq}\left(\frac{\partial S_{mn}}{\partial E_{pq}}\right) \tag{19.16b}$$

Note that the Voigt notation has been used in Equation (19.16a), and elastic constants correspond to the components of the fourth elasticity tensor are defined in Equation (19.16b). By plugging the model parameters and the deformation gradient, the Young's modulus for a (10,10) and (100,100) nanotube are obtained as 0.7 and 1TPa, respectively. It is observed that the Young's modulus from the case of (10,10) is quite different from that of graphite due to the effect of rolling. Such effect becomes small as the radius of CNT increases. Note that this value of Young's modulus is determined *consistently* based on crystal elasticity *combined* with the use of MD simulation. In contrast with some of the approaches described in Section 19.2.2.1, which use purely molecular dynamics to determine the Young's modulus, the approach is semi-analytical and serves as a link between the continuum and atomistic scale. In addition, as we extend to the finite deformation case, the issue of anisotropy naturally arises as a result of this formulation, which can only be qualitatively reproduced by MD. It is emphasized that the thickness assumption is only used in the comparison with the experiments or theoretical predictions that have taken the interlayer separation as the thickness. Clearly this thickness t is not needed in our formulation.

The procedure described above reveals certain limitations of the standard hyperelastic approach and Cauchy–Born rule, which can be described as follows:

- The deformation is in fact not homogenous as the graphene sheet is rolled into CNT. Correspondingly, the energy of the CNT not only depends on the deformation gradient but also on higher order derivatives of *F*. In such case, a set of high-order elastic constants that belongs to the framework of *multipolar* theory[136] needs to be determined.
- Another aspect that has been missing in the hyperelastic theory is the dependence of the energy on the so-called inner displacement of the lattice, which can be defined as the relative displacement between two overlapping Bravais lattices. Note that the inner displacement can occur without violating the Cauchy–Born rule. According to Cousins,[137] the consideration of these variables results in the so-called *inner elastic constants*.

In general, the factors mentioned above are difficult to evaluate through purely analytical method. A continuum treatment, which accounts for the effect of inner displacement, has been proposed recently in References 138 through 140. For computational implementations, see Section 19.4.3.

19.3 Experimental Techniques

The extremely small dimensions of CNTs — diameters of a few tens of nanometers for MWCNTs and about 1 *nm* for SWCNTs, and length of a few microns — impose a tremendous challenge for experimental study of mechanical properties. The general requirements for such study include (1) the challenge of CNT placement in an appropriate testing configuration, such as of picking and placing, and in certain cases the fabrication of clamps; (2) the achievement of desired loading; and (3) characterizing and measuring the mechanical deformation at the nanometer length scale. Various types of high-resolution microscopes are indispensable instruments for the characterization of nanomaterials, and recent innovative developments in the new area of *nanomanipulation* based on inserting new tools into such instruments has enhanced our ability to probe nanoscale objects. We discuss several of these below.

19.3.1 Instruments for the Mechanical Study of Carbon Nanotubes

Electron microscopy (EM, SEM, and TEM) and scanning probe microscopy (SPM) have been the most widely used methods for resolving and characterizing nanoscale objects. Electron microscopy uses high-energy electron beams (several keV up to several hundred keV) for scattering and diffraction, which allows the achievement of high resolving power, including down to subnanometer resolution because of the extremely short wavelength (a fraction of an Angstrom) of electrons at high kinetic energy.

We and others have primarily used transmission electron microscopy (TEM) and scanning electron microscopy (SEM) to study nanotube mechanics. In TEM, an accelerated electron beam from a thermal or a field emitter is used. The beam transmits through the sample and passes several stages of electro-magnetic lenses, projecting the image of the studied sample region to a phosphor screen or other image recording media. In SEM, a focused electron beam (nanometers in spot size) is rastered across the sample surface; and the amplified image of the sample surface is formed by recording the secondary electron signal or the back scattering signal generated from the sample.

Sample requirements typically differ between TEM and SEM. In TEM, a thin (normally several tens of nanometers or less in thickness) and small (no more than 50mm^2) sample is a requirement as a small sample chamber is available; and a dedicated holder is typically used in these expensive instruments (which are thus typically time-shared among many users) for sample transfer. In SEM there is no strict limit on sample size in principle, and normally a large sample chamber is available so that samples can be surveyed over large areas. As to the difference in the ultimate resolution, TEM is limited by such factors as the spread in energy of the electron beam and the quality of the ion optics; and SEM is limited by the scattering volume of the electrons interacting with the sample material. TEM normally has a resolution on the order of 0.2 nm, while SEM is capable of achieving a resolution up to 1 nm.

An exciting new development in electron microscopy is the addition of aberration correction, also referred to as *corrective ion optics*. We provide no extensive review of this topic here, but note for the reader that a coming revolution in electron microscopy will allow for image resolution of approximately 0.04 nm with TEM and of about 0.1 nm for SEM, and perhaps better. There are two types of corrective ion optics: one corrects for spherical aberration (to correct for aberration in the lenses) and one for achromatic aberration (meant to correct for the spread in the wavelengths of the electrons emanating from the emitter). As newer instruments are installed in the next few years, such as at national laboratories, improvement in the image resolution for mechanics studies of nanosized specimens is an enticing goal (see, for example, http://www.ornl.gov/reporter/no22/dec00.htm and http://www.nion.com/).

The scanning or atomic force microscope (SFM, also referred to as AFM) has also been particularly useful for mechanical studies of CNTs. Since the invention of the STM in 1986, it has been quickly accepted as a standard tool for many applications related to surface characterization. High-resolution (nanometer up to atomic resolution) mapping of surface morphology on almost any type of either conductive or nonconductive material can be achieved with an SFM.

The principle of the microscope is relatively simple. A probe, having a force-sensitive cantilever with a sharp tip, is used as a sensor to physically scan, in close proximity to, the sample surface. The probe is driven by a piezoelectric tube capable of nanometer-resolution translations in the x, y and z directions; and the tip normally has a radius of curvature on the order of 10 nm. The force interaction between tip and sample results in deflection of the cantilever. While scanning the sample surface in the x and y directions, the deflection of the cantilever is constantly monitored by a simple optical method or other approaches. A feedback electronic circuit that reads the deflection signal and controls the piezoelectric tube is responsible for keeping a constant force between the tip and the sample surface, and a surface profile of the sample can thus be obtained. Depending on the type of interaction force involved for sensing, an SPM instrument can include a host of methods, such as AFM, friction-force microscopy (FFM), magnetic-force microscopy (MFM), electric-force microscopy (EFM), and so on. Depending on the mechanism used for measuring the force interaction, scanning probe microscopy also includes many

modes of operation, such as contact mode, tapping mode, and force modulation mode. For more information on scanning force microscopy, see, for example, References 141 and 142 as well as http://www.thermomicro.com/spmguide/contents.htm.

19.3.2 Methods and Tools for Mechanical Measurement

Following is a brief summary of the methods used for measuring the mechanical properties of CNTs, and especially isolated individual CNTs; and new tools specifically designed for such tasks will be introduced.

19.3.2.1 Mechanical Resonance Method

Treacy and co-workers[31] deduced values for Young's modulus for a set of MWCNTs by measuring the amplitude from recorded TEM images of the thermal vibration of the free ends of each when naturally cantilevered. Krishnan et al.[46] succeeded in measuring the Young's modulus of SWCNTs (Figure 19.17) using a similar method. The amplitude was measured from the blurred spread of tip positions of the free end of the cantilevered CNT compared with the clamped end. The amplitude can be modeled by considering the excitation of mechanical resonance of a cantilever:

$$\sigma^2 = \frac{16L^3 kT}{\pi Y (a^4 - b^4)} \sum_n \beta_n^{-4} \approx 0.4243 \frac{L^3 kT}{Y(a^4 - b^4)} \tag{19.17}$$

where σ is the amplitude at the free end, L is the length of the cantilevered beam, k is the Boltzmann constant, T is the temperature, Y is the Young's modulus, a is the outer radius and b is the inner radius of CNT, and β_n is a constant for free vibration mode n. The tip blurring originates from thermal activation of vibrations (the CNT behaves classically because of the low frequency modes that are populated by the expected kT of thermal vibrational energy), and the amplitude can be modeled by considering the excitation of mechanical resonance of a cantilever. The image is blurred simply because the frequency is
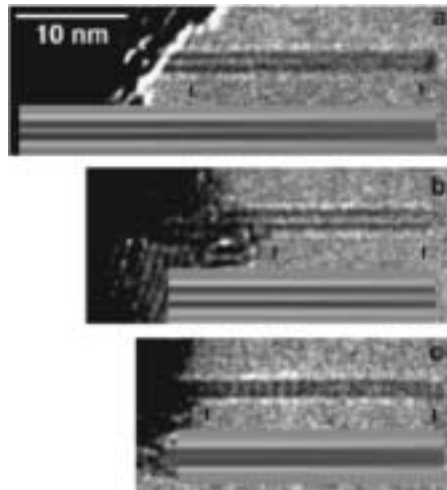

FIGURE 19.17 TEM images of vibrating single-walled nanotubes. Inserted with each micrograph is the simulated image corresponding to the best least-square fit for the adjusted length L and tip vibration amplitude σ. The tick marks in each micrograph indicate the section of the nanotube shank that was fitted. The nanotube length, diameter W, tip amplitude, and the estimated Young's modulus E are (a) $L = 36.8$ nm, $\sigma = 0.33$ nm, $W = 1.50$ nm, $E = 1.33 \pm 0.2$ TPa; (b) L = 24.3 nm, $\sigma = 0.18$ nm, $W = 1.52$ nm, $E = 1.20 \pm 0.2$ TPa; and (c) $L = 23.4$ nm, $\sigma = 50.30$ nm, $W = 1.12$ nm, $E = 1.02 \pm 0.3$ TPa. (From Krishnan A, Dujardin E, Ebbesen TW, Yianilos PN, and Treacy MMJ, (1998), Young's modulus of single-walled nanotubes, *Phys. Rev. B.* 58(20): 14013–14019. With permission.)
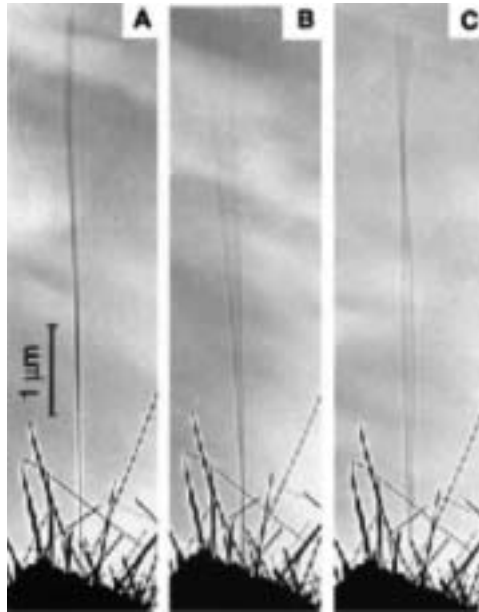
FIGURE 19.18 Electric field-driven resonance of MWCNT. (A) In the absence of a potential, the nanotube tip $(L = 6.25$ mm, $D = 14.5$ nm) vibrated slightly because of thermal effects. (B) Resonant excitation of the fundamental mode of vibration $(f_1 = 530$ kHz. (**C**) Resonant excitation of the second harmonic $(f_2 = 3.01$ MHz). For this nanotube, a value of $E_b = 0.21$ TPa was fit to the standard continuum beam mechanics formula. (Reprinted from Poncharal P, Wang ZL, Ugarte D, and de Heer WA, (1999), Electrostatic deflections and electromechanical resonances of carbon nanotubes, *Science.* 283(5407): 1513–1516. ©1999 American Association for the Advancement of Science. With permission.)

high relative to the several-second integration time needed for generating the TEM image. Because the resonance is a function of the cantilever stiffness, and the geometry is directly determined by the TEM imaging, the Young's modulus values could be fit. The advantage of this method is that it is simple to implement without the need for additional instrument modification or development — only a variable-temperature TEM holder is needed. The principle can also be applied for the study of other nanowire-type materials as long as the tip blurring effect is obvious. The drawback is that a model fit is needed to determine the real cantilever length, and human error is inevitable in determining the exact amplitude of the blurred tip. As pointed out by the authors, the error for the Young's modulus estimation using such method is around ±60%.

Poncharal et al.[44] introduced an electric field excitation method (Figure 19.18) for the study of mechanical resonance of cantilevered MWCNTs and measured the bending modulus. In the experiment, a specially designed TEM holder was developed that incorporated a piezo-driven translation stage and a mechanical-driven translation stage. The translation stages allowed the accurate positioning of the MWCNT material inside the TEM, in this case relative to a counter electrode. Electrical connections were made to the counter electrode and the electrode attaching the MWCNT materials, so that DC bias as well as AC sinusoidal voltage could be applied between the counter electrode and the MWCNT. The generated AC electric field interacts with induced charges on the MWCNT, which produces a periodic driving force. When the frequency of the input AC signal matched the mechanical resonance frequency of the MWCNT, obvious oscillation corresponding to the resonance mode of the cantilever MWCNT was observed (Figure 19.18) and the resonance frequency of the MWCNT thereby determined. Using continuum beam mechanics, the bending modulus of the MWCNT was calculated from the measured resonance frequency and CNT geometry according to Equation (19.2). The benefits of such an approach are the efficient method for driving mechanical resonances and, because the whole experiment is done inside a TEM, the ability to analyze the high-aspect ratio nanostructures in detail.

19.3.2.2 Scanning-Force Microscopy Method

The atomic force microscope operated in lateral-force mode, contact mode, or tapping mode, has been the main tool in studying the mechanical response of individual CNTs under static load and when in contact with surfaces. Falvo et al.[66] used a nanomanipulator and contact mode AFM to manually manipulate and bend MWCNTs deposited on a substrate surface. The strong surface force between the MWCNTs and the substrate allowed such an operation to be performed. By intentionally creating large curvature bends in MWCNTs, buckles and periodic ripples were observed. These authors estimated that, based on the local curvature of the bend found, some MWCNTs could sustain up to 16% strain without obvious structural or mechanical failure (Figure 19.19)

Wong et al.[48] measured the bending modulus of individual MWCNTs using an AFM operated in lateral-force mode (Figure 19.20). The MWCNTs, deposited on a low-friction MoS2 surface, were pinned down at one end by overlaying SiO pads using lithography. AFM was then used to locate and measure the dimension of the MWCNT, and lateral force was applied at the different contact points along the length of the MWCNT (Figure 19.20). By laterally pushing the MWCNT, lateral force vs. deflection data were recorded. The data were then analyzed using a beam mechanics model that accounted for the friction force, the concentrated lateral force, and the rigidity of the beam. The bending modulus value for the MWCNT was obtained by fitting the measured force vs. deflection curve. Such a method also allowed the bending strength to be determined by deflecting the beam past the critical buckling point.

Salvetat et al. used another approach to deflect under load MWCNT[49] and SW$_{CNT}$ ropes[50] by depositing them onto a membrane having 200 nm pores (Figure 19.21). By positioning the AFM tip directly on the midpoint of the CNT spanning the pore and applying an indentation force (Figure 19.21), force vs. deflection curves were obtained and compared with theoretical modeling based on beam mechanics. Elastic moduli
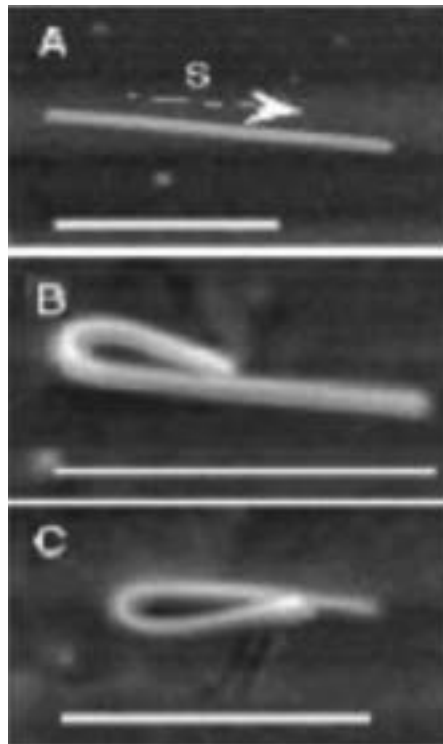

FIGURE 19.19   Bending and buckling of MWCNTs. (a) An original straight MWCNT. (b) The MWCNT is bent upwards all the way back onto itself. (c) The same MWCNT is bent all the way back onto itself in the other direction (Reprinted from Falvo MR, Clary GJ, Taylor RM, Chi V, Brooks FP, Washburn S, and Superfine R, (1997), Bending and buckling of carbon nanotubes under large strain, *Nature*. 389(6651): 582–584. ©1997 Macmillan Publishers. With permission.)
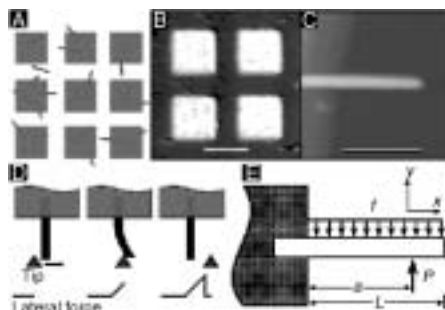
FIGURE 19.20 Overview of one approach used to probe mechanical properties of nanorods and nanotubes. (A) SiC nanorods or carbon nanotubes were deposited on a cleaved MoS_2 substrate, and then pinned by deposition of a grid of square SiO pads. (B) Optical micrograph of a sample showing the SiO pads and the MoS_2 substrate. The scale bar is 8 mm. (C) An AFM image of a 35.3 nm diameter SiC nanorod protruding from an SiO pad. The scale bar is 500 nm. (D) Schematic of beam bending with an AFM tip. The tip (triangle) moves in the direction of the arrow, and the lateral force is indicated by the trace at the bottom. (E) Schematic of a pinned beam with a free end. The beam of length L is subjected to a point load P at $x = a$ and to a distributed friction force f. (Reprinted from Wong EW, Sheehan PE, and Lieber CM, (1997), Nanobeam mechanics: elasticity, strength, and toughness of nanorods and nanotubes, *Science*. 277(5334): 1971–1975. ©1997 American Association for the Advancement of Science. With permission.)
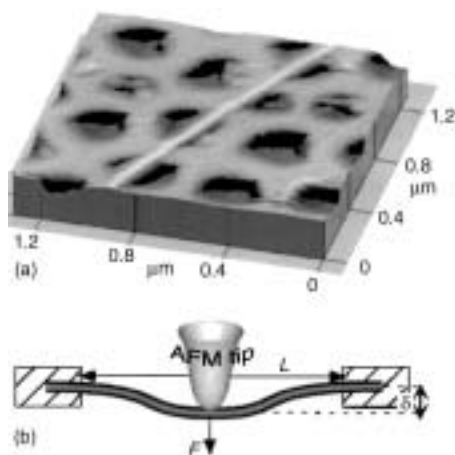

FIGURE 19.21 (a) AFM image of an SWCNT bundle adhered to the polished alumina ultrafiltration membrane, with a portion bridging a pore of the membrane. (b) Schematic of the measurement: the AFM is used to apply a load to the nanobeam and to determine directly the resulting deflection. A closed-loop feedback ensured an accurate scanner positioning. Si_3N_4 cantilevers with force constants of 0.05 and 0.1 N/m were used as tips in the contact mode. (From Salvetat JP, Briggs GAD, Bonard JM, Bacsa RR, Kulik AJ, Stockli T, Burnham NA, and Forro L, (1999), Elastic and shear moduli of single-walled carbon nanotube ropes, *Phys. Rev. Lett.* 82(5): 944–947. With permission.)

for individual MWCNTs and separately for SWCNT bundles were deduced. In principle, such a measurement requires a well-controlled and stable environment to eliminate the errors induced by unexpected tip–surface interactions and instrument instability as well as a very sharp AFM tip for the experiment.

The radial deformability of individual MWCNTs was studied by Shen et al.[78] using an indentation method and Yu et al.[79] using a tapping mode method in AFM. Load was applied along the radial direction (perpendicular to the axial direction that is defined as along the long-axis of the CNT) of MWCNTs, and the applied force vs. indentation depth curve was measured. Using the classic Hertz theory, the deformability of the MWCNT perpendicular to the long axis direction was obtained. The reader should note that this is not the radial compressibility, because the force is not symmetrically applied in the radial direction (not isotropic). Thus, one might think of this as *squashing* the MWCNT locally by indentation.
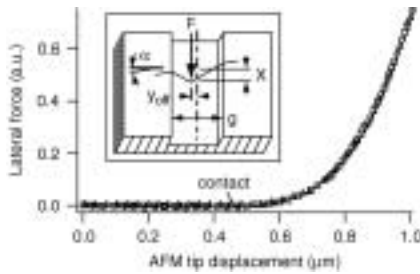
FIGURE 19.22 Lateral force on SWCNT bundle as a function of AFM tip position. The four symbols represent data from four consecutive lateral force curves on the same rope, showing that this rope is straining elastically with no plastic deformation. Inset: The AFM tip moves along the trench, in the plane of the surface, and displaces the rope as shown. (From Walters DA, Ericson LM, Casavant MJ, Liu J, Colbert DT, Smith KA, and Smalley RE, (1999), Elastic strain of freely suspended single-wall carbon nanotube ropes, *Appl. Phys. Lett.* 74(25): 3803–3805. With permission.)

These two approaches are technically different. In the indentation method, the image scan is stopped and the AFM tip is held steady to apply a vertical force on a single point on the MWCNT through the extension and retraction of the piezoelectric tube along the z direction. A force vs. indentation depth curve is obtained by monitoring the AFM cantilever deflection under the extension or retraction. In the tapping mode method, an off-resonance tapping technique is used so that the tapping force can be quantitatively controlled by adjusting the free cantilever amplitude and the set point. The set point is a control parameter in tapping mode AFM for keeping a constant cantilever amplitude (thus a constant distance between the AFM tip and the sample surface) in imaging scan mode. AFM images of each MWCNT are acquired using different set points, and force vs. indentation depth curves are obtained by plotting the curve of the set point vs. MWCNT height. The advantage of using the tapping mode method is that the squashing deformability of the MWCNT along its whole length can be obtained through several image acquisitions, though care must be taken to choose the appropriate tapping mode imaging parameters for such an experiment.

Walters et al.[92] studied the elastic strain of SWCNT nanobundles by creating a suspended SWCNT bundle that was clamped at both ends by metal pads over a trench created with standard lithographic methods. Using an AFM operated in lateral-force mode, they were able to repeatedly stretch and relax the nanoropes elastically as shown in Figure 19.22, including finally stretching to the breaking point to determine the maximum strain. The absolute force used to stretch the SWCNT bundle was not measured, and the breaking strength was estimated by assuming the theoretical value of ~1 TPa for Young's modulus for the SWCNTs in the rope.

19.3.2.3 Measurement Based on Nanomanipulation

The response to axial tensile loading of individual MWCNTs was realized by Yu et al.[29] using a new testing stage based on a nanomanipulation tool operating inside an SEM. The nanomanipulation stage allowed for the three-dimensional manipulation — picking, positioning, and clamping — of individual MWCNTs. The individual MWCNTs were attached to AFM probes having sharp tips by a localized electron beam induced deposition (EBID) of carbonaceous material inside the SEM. An MWCNT so clamped between two AFM probes was then tensile loaded by displacement of the rigid AFM probe (Figure 19.23), and the applied force was measured at the other end by the cantilever deflection of the other, compliant AFM probe. The measured force vs. elongation data were converted, by SEM measurement of the MWCNT geometry, to a stress vs. strain curve; and the breaking strength of each MWCNT was obtained by measuring the maximum tensile loading force at break.

Yu et al.[28] applied a similar approach for the tensile strength measurement of small bundles of SWCNTs. The entangled and web-like agglomeration of SWCNTs in raw samples made it difficult to find an individual SWCNT and resolve it by SEM or to pick out individual SWCNT nanobundles; so a modified
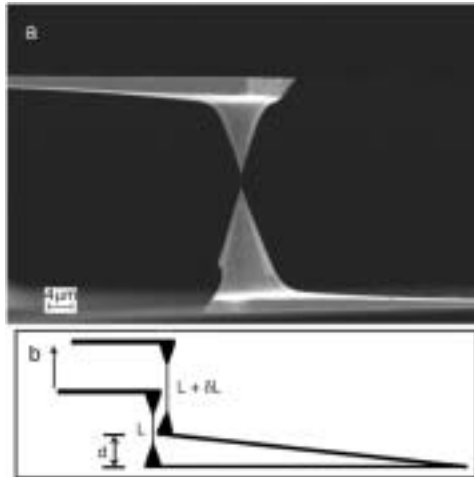
FIGURE 19.23 (a) Individual MWCNT is clamped in place and stretched by two opposing AFM tips. (b) Schematic of the tensile loading experiment. (Reprinted from Yu MF, Lourie O, Dyer MJ, Moloni K, Kelly TF, and Ruoff RS, (2000), Strength and breaking mechanism of multi-walled carbon nanotubes under tensile load, *Science*. 287(5453): 637–640. ©2000 American Association for the Advancement of Science. With permission.)
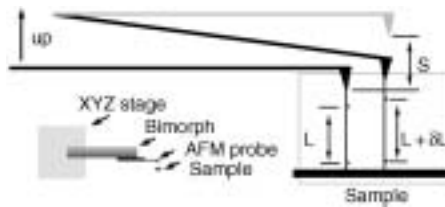

FIGURE 19.24 Schematic showing the principle of the experiment for the measurement of the tensile strength of SWCNT bundles. The gray cantilever indicates where the cantilever would be if no rope were attached on the AFM tip after its displacement upward to achieve tensile loading.

approach was used for the experiment. SWCNT bundles having a strong attachment at one end to the sample surface were selected as candidates for the measurement. The free end of the SWCNT bundle was then approached and attached to an AFM tip by the same EBID method outlined above. The AFM tip was used to stretch the SWCNT bundle to the breaking point, and the same AFM tip also served as the force sensor to measure the applied force (Figure 19.24). Stress vs. strain curves for SWCNT bundles were obtained as well as the breaking strength; these stress vs. strain curves were generated by assuming a model in which only the perimeter SWCNTs in a bundle actually carried the load. The reader is referred to Reference 26 for the full explanation of this model.

The shear strength between the shells of an MWCNT is also an interesting subject for experimental study. Yu et al.[11] were able to directly measure the friction force between the neighboring layers while pulling the inner shells out of the outer shells of an MWCNT, using the same apparatus for measuring the tensile strength of individual MWCNTs. The possibility of such measurement was based on the discovery that tensile-loaded MWCNTs normally broke with a sword-in-sheath breaking mechanism.[29] The separated outer shell can still be in contact with the underlying inner shell in certain cases (in other cases, the *snap back* of the loading and force-sensing cantilevers leads to two separated fragments). The consecutive measurement of force and contact length (the overlap length between the outer shell and its neighbor) provided the necessary data for obtaining the dynamic and static shear strength between the shells.
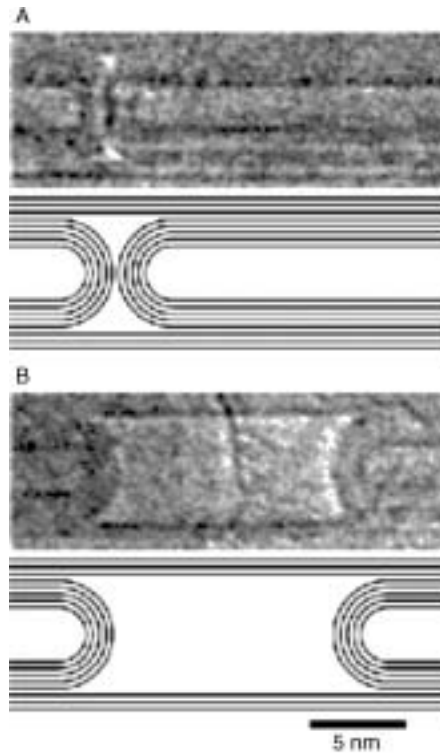
FIGURE 19.25 (A) An as-grown bamboo section. (B) The same area after the core tubes on the right have been telescoped outward. The line drawings beneath the images are schematic representations to guide the eye. (Reprinted from Cumings J and Zettl A, (2000), Low-friction nanoscale linear bearing realized from multi-wall carbon nanotubes, *Science.* 289(5479): 602–604. ©2000 American Association for the Advancement of Science. With permission.)

A similar experiment done in a TEM rather than an SEM was that of Cummings et al.,[107] who used a TEM holder having a piezoelectric-driven translation stage for approaching and opening the end of a MWCNT. The MWCNT cap was opened by *eroding* it away, using an electric discharge method inside the TEM.[143] The end of the exposed core part was then spot-welded to the moving probe using a short electrical pulse, and the MWCNT was telescoped by drawing out the core part from the outer shell housing. It was then possible to disengage the core part from the welding spot and observe the retraction of the core part back into its housing by the surface-driven forces (Figure 19.25). By analyzing the surface force and the friction forces involved in such a retraction using published parameters and modeling, the upper limit values for the dynamic and static friction force between the shells were estimated but not experimentally measured

19.3.3 Challenges and New Directions

The new developments in the area of nanoscale manipulation and measurement as reflected in the studies presented in the last section have certainly helped our understanding of the mechanics of CNTs. Because CNTs possess unique one-dimensional structures that maintain their conformations while being manipulated (in contrast, e.g., to biomolecules or certain polymer systems), they represent a "nanotinkertoy" for manipulation on the nanoscale. Therefore, such types of approaches also provide a window on current capabilities for exploring and exploiting the nanoworld and an avenue for future advancement in methods and tools useful in nanotechnology. In general, mechanical characterization takes a totally different approach than does electrical characterization. Mechanical characterization normally requires dynamic physical interaction with the object. — for example, in the case for CNT, stretching, bending, compressing,

and twisting with nanometer positioning accuracy, while performing measurement with nano-Newton force resolution and nanometer dimensional change resolution. Thus, in order for a successful and reliable mechanical study on nanoscale structures, extreme care must be taken to evaluate the three-dimensional stability and accuracy of the instrument and the effect of any significant external factors such as surface contact, mechanical attachment, stray electric charge, and so on. The experiments described in the last section represent the current state of the art in the manipulation and mechanical characterization of CNTs and should provide useful references for further instrument development, which can then be applied to many other low-dimensional nanostructures for mechanical studies.

But what has the community not yet achieved? We have not yet measured the tensile-loading response of an individual SWCNT, nor have we applied a known torque and controllably introduced a twist or series of twists along a CNT. The challenges here include: (1) the visualization, manipulation, precise placement, and fixation of a *flexible* one-dimensional nanostructure, the SWCNT, onto a device having displacement and force-sensing capabilities for the tensile measurement; and (2) a technical breakthrough in generating repeatable coaxial rotation with subnanometer runoff and with sufficient force output for applying torque to CNT. The influence of environment on NT mechanics — such as effects of temperature, chemical environment, or loading rate — has not yet been explored in any detail; nor do we have a clear and detailed picture of the initial defect distribution, or the nucleation, propagation, and ultimate failure resulting from defects. From the experimental perspective, such advances will come with new approaches and automated tools with subnanometer or atomic scale resolving power and stability generated by innovative thinking. It is clear that to attain further advances in nanoscale mechanics, focused effort is necessary in developing new measurement tools that can be integrated into high spatial resolution imaging instruments and that incorporate micro- or nanoelectromechanical system designs.

19.4   Simulation Methods

There are two major categories of molecular simulation methods for NT systems: classical molecular dynamics (MD) and *ab initio* methods. In general, *ab initio* methods give more accurate results than MD, but they are also much more computationally intensive. A hybrid method, tight-binding molecular dynamics (TBMD), is a blend of certain features from both MD and *ab initio* methods. In addition to these methods, continuum and multiscale approaches have also been proposed.

19.4.1   *Ab Initio* and Tight-Binding Methods

The central theme of *ab initio* methods is to obtain accurate solutions to the Schrödinger equation. A comprehensive description of these methods can be found in the book by Ohno et al.[144] Some notation is also adapted in this section. For general background in quantum mechanics, the reader is referred to any of the standard textbooks, such as References 145 through 149. In general, the state of a particle is defined by a wave function ψ based on the well-known wave–particle duality. The Schrödinger equation is

$$H\psi = E\psi \qquad (19.18)$$

where H is the Hamiltonian operator of the quantum mechanical system, and ψ is the energy eigenfunction corresponding to the energy eigenvalue E.

Although the phrase *ab initio* is used, analytical or exact solutions are available only for a very limited class of problems. In general, assumptions and approximations need to be made. One of the most commonly used approximations is the Born–Oppenheimer approximation. In this approximation, it is assumed that the electrons are always in a steady state derived from their averaged motion because their positions change rapidly compared to the nuclear motion. Therefore, the motion of the electrons can be considered separately from the motion of the nuclei — as if the nuclei were stationary.

For an N-electron system, the Hamiltonian operator for each electron can be expressed as:

$$H_i = -\frac{1}{2}\nabla_i^2 + \sum_{j>i}^{N} \frac{1}{|\mathbf{r}_i - \mathbf{r}_j|} + \nu(\mathbf{r}_i) \tag{19.19}$$

The Hamiltonian operator in the above equation is composed of three parts. The first term in Equation (19.19) gives the kinetic energy when operating on the electron wave function; the second term gives the electron–electron Coulomb interaction; and the last term comes from the Coulomb potential from the nuclei. The total Hamiltonian operator of the N-electron system is then:

$$H = \sum_{i=1}^{N} H_i \tag{19.20}$$

and the electron state is solved from the following eigenvalue equation:

$$H\psi_{\lambda_1, \lambda_2, \ldots, \lambda_N} = E_{\lambda_1, \lambda_2, \ldots, \lambda_N}\psi_{\lambda_1, \lambda_2, \ldots, \lambda_N} \tag{19.21a}$$

in which λ_i denotes an eigenstate that corresponds to the one-electron eigenvalue equation:

$$H_i\psi_{\lambda_i} = E_{\lambda_i}\psi_{\lambda_i} \tag{19.21b}$$

Because obtaining exact solutions to Equation (19.21b) is generally very difficult, approximation methods have been developed. In the following, we will introduce two of the most commonly used approaches.

19.4.1.1 The Hartree–Fock Approximation

In the Hartree–Fock approximation,[150–152] the ground state of the Hamiltonian H is obtained by applying the variational principle with a normalized set of wave functions ψ_i. The methodology is identical to the Ritz method, i.e., to seek the solution by minimizing the expectation value of H with a trial function:

$$\langle \psi|H|\psi \rangle = \sum_{S_1}\sum_{S_2}\sum_{S_3} \int \psi^* H\psi \, dr_1 dr_2 \ldots dr_N \tag{19.22}$$

One possible choice of the trial function is the Slater determinant of the single-particle wave functions, i.e.,

$$\psi = \frac{1}{\sqrt{N!}} \begin{vmatrix} \psi_1(1) & \psi_2(1) & \ldots & \psi_N(1) \\ \psi_1(2) & \psi_2(2) & & \psi_N(2) \\ . & . & & . \\ . & . & & . \\ \psi_1(N) & \psi_2(N) & & \psi_N(N) \end{vmatrix} \tag{19.23}$$

In the above equation, the number in the bracket indicates the particle coordinate, which is composed of the spatial coordinate r and internal spin degree of freedom. The subscript denotes the energy level of the wave function, and $\psi_\lambda(i)$ forms an orthonormal set.

The Hamiltonian, on the other hand, is decomposed into a one-electron contribution H_0 and two-body electron–electron Coulomb interaction U as follows:

$$H = \sum_i H_0(i) + \frac{1}{2}\sum_{i,j} U(i,j) \tag{19.24}$$

The one-electron contribution H_0 consists of the kinetic energy and nuclear Coulomb potential:

$$H_0(i) = -\frac{1}{2}\nabla_i^2 + v(r_i) \tag{19.25}$$

in which

$$v(r_i) = -\sum_j \frac{Z_j}{|r_i - R_j|} \tag{19.26}$$

with Z_j being the nuclear charge of the jth atom. The two-body electron–electron interaction is given as the Coulomb interaction:

$$U(i, j) = \frac{1}{|\boldsymbol{r}_i - \boldsymbol{r}_j|} \tag{19.27}$$

With the trial function and decomposition of H, the expectation value of the Hamiltonian can then be rewritten as:

$$\langle \psi|H|\psi \rangle = \sum_{\lambda=1}^{N} \langle \psi_\lambda|H_0|\psi_\lambda \rangle + \frac{1}{2}\sum_{\lambda,\nu} \langle \psi_\lambda\psi_\nu|U|\psi_\lambda\psi_\nu \rangle - \frac{1}{2}\sum_{\lambda,\nu} \langle \psi_\lambda\psi_\nu|U|\psi_\nu\psi_\lambda \rangle \tag{19.28}$$

Applying the variational principle to Equation (19.28), it can be shown that solving the electron state of the system can now be approximated by solving the following equation for the one-electron wave function:

$$H_0\psi_\lambda(i) + \left[\sum_{\nu=1}^{N}\sum_{S_j}\int\psi_\nu^*(j)U(i,j)\psi_\nu(j)dr_j\right]\psi_\lambda(i)$$

$$-\left[\sum_{\nu=1}^{N}\sum_{S_j}\int\psi_\nu^*(j)U(i,j)\psi_\lambda(j)dr_j\right]\psi_\lambda(i) = \varepsilon_\lambda\psi_\lambda(i) \tag{19.29}$$

in which ε_j is the Lagrangian multiplier used to enforce the orthonormal condition for the eigenfunction. The Hartree–Fock approximation has been used in many *ab initio* simulations. A more detailed description and survey of this method can be found in Reference 153.

19.4.1.2 Density Functional Theory

The density functional theory was originally proposed in a paper by Hohenberg and Kohn.[154] In this paper, they showed that the ground-state electronic energy is a unique functional of the electronic density. In most cases, the potential due to the external field comes mainly from the nuclei. The electronic energy can then be expressed as:

$$E = T[\rho(r)] + \int\frac{[\rho(r)\rho(r')]}{(|r-r'|)}drdr' + \int V_N(r)dr + E_{XC}[\rho(r)] \tag{19.30}$$

In Equation (19.30), $T[\rho(r)]$ is the kinetic energy and is a function of the electron density; the second term represents the electrostatic potential; the third term denotes the contribution from the nuclei; and the last term is the exchange–correlation functional. Kohn and Sham[155] presented a procedure to calculate the electronic state corresponding to the ground state using this theory, and their method is generally referred to as the *local-density approximation,* or LDA. LDA is another type of widely used *ab initio* method. The term *local density* comes from the assumption that the exchange–correlation function corresponding to the homogeneous electron gas is used. This assumption is only valid locally when the inhomogeneity due to the presence of the nuclei is small.

The essence of the LDA method is to obtain the ground state by introducing the variational principle to the density functional. This leads to a one-electron Schrödinger equation (also called the Kohn–Sham equation) for the Kohn–Sham wave function ψ_λ

$$\left\{ -\frac{1}{2}\nabla^2 + v(r) + \int \frac{\rho(r')}{|r - r'|} dr' + \mu_{XC}[\rho](r) \right\} \psi_\lambda(r) = \varepsilon_\lambda \psi_\lambda(r) \qquad (19.31)$$

Note that the term $\mu_{XC}[\rho](r)$ is the derivative of the exchange–correlation functional with respect to the electron density. Different functional forms for the exchange–correlation energy have been proposed.[156–159] The problem is reduced to obtaining the solutions to systems of one-electron equations. Once ψ_λ and ε_λ are solved, the total energy can be obtained from Equation (19.30). The major advantage of using LDA is that the error in the electron energy is second-order between any given electron density and ground-state density.

The solution procedure requires an iterative diagonalization process, which in general involves $O(N^3)$ order of computation. A single electron wave function with a plane-wave basis and pseudo-potential have been used in the application of the LDA method.[160] Major improvements have been made using the Car–Parrinello MD method[161] and conjugate gradient (CG) method.[160] The Car–Parrinello method reduces the order from $O(N^3)$ to $O(N^2)$. As shown in Reference 160, the CG method can even be more efficient.

19.4.1.3   The Tight-Binding Method

The tight-binding theory was originated by Slater and Koster.[162] The advantage of the tight-binding method is that it can handle a much larger system than the *ab initio* method while maintaining better accuracy than MD simulation. A survey of the method can be found in Reference 163. In the tight-binding method, a linear combination of atomic orbitals (referred to LCAO) is adopted in the wave function. Although the exact forms of the basis are not known, the Hamiltonian matrix can be parameterized; and the total energy and electronic eigenvalues can be deduced from the Hamiltonian matrix. The interatomic forces are evaluated in a straightforward way based on the Hellmann–Feynman theorem, and the rest of the procedure is almost identical to the MD simulation. For this reason sometimes the tight-binding method is also referred to as the *tight-binding MD method* or simply *TBMD.*

As shown by Foulkes and Haydock,[164] the total energy can be expressed as the sum of the eigenvalues of a set of occupied nonself-consistent one-electron molecular eigenfunctions in addition to certain analytical functions. The analytical function is usually assumed to take the form of a pair–additive sum. For example, the total energy can be given as

$$E = \sum_i \sum_{j > i} E_{ij} + \sum_k \varepsilon_k \qquad (19.32)$$

The first term on the right side is the interatomic interaction, and the second term is the sum of the energies of occupied orbitals. A simple scheme in constructing the second term is to expand the wave function in a localized orthonormal minimal basis with parameterized two-center Hamiltonian matrix elements. The parameterization process can be performed by fitting to results from the *ab initio* methods[165,166] or computing the matrix exactly based on the localized basis.[167–169] A major problem with the TBMD method is the way that the parameterization of the Hamiltonian limits its applicability, or *transferability* as referred to in the computational physics community. As a simple example, when one switches from diamond structure to graphite, the nature of the nearest neighbor changes. In the early development of TBMD, Harrison[163] attempted to use a set of universal parameters; this approach turns out to be neither transferable nor accurate. The solution is then to add in modifications[170,171] or to use a completely different basis.[172]

19.4.2 Classical Molecular Dynamics

Many reviews are available on the subject of classical molecular dynamics.[173–175] MD is essentially a particle method[176,177] because the objective is to solve the governing equations of particle dynamics based on Newton's second law, i.e.,

$$m_i \frac{d^2 \mathbf{r}_i}{dt^2} = -\nabla V \qquad (19.33)$$

in which m_i and $\mathbf{r}_i$ are the mass and spatial coordinates of the ith atom, respectively; V is the empirical potential for the system; and ∇ denotes the spatial gradient. Due to the small time scale involved, explicit integration algorithms such as the Verlet method[178,179] and other high-order methods are commonly used to ensure high-order accuracy.

An alternate but equivalent approach is to solve the Hamiltonian system of ordinary differential equations:

$$dp_i/dt = -\partial H/\partial q_i \qquad (19.34)$$

$$dq_i/dt = -\partial H/\partial p_i \qquad (19.35)$$

in which (q_i, p_i) are the set of canonically conjugate coordinates and momenta, respectively. H is the Hamiltonian function given as:

$$H = \sum_{i=1}^{N} \frac{p_i^2}{2m_i} + V \qquad (19.36)$$

Symplectic integrators[180] have been developed to solve the above Hamiltonian equations of motion. The major advantages of this class of methods are that certain invariant properties of the Hamiltonian system can be preserved,[180] and it is easy to implement in large-scale computations.

19.4.2.1 Bonding Potentials

The basic formulation of MD requires that the spatial gradient of the potential function V be evaluated. Different empirical potentials for an NT system have been developed to satisfy this requirement. Allinger and co-workers developed[181,182] a molecular mechanics force field #2 (MM2) and an improved version known as the MM3 force field. Their model has been applied in the analysis of a variety of organic and inorganic systems. It should be noted that MM2/MM3 is designed for a broad class of problems. It is expected that the model may not work well under certain conditions. For example, the model is known to yield unrealistic results when interatomic distance is in the region of highly repulsive interactions. Mayo et al.[183] presented a generic force field based on simple hybridization considerations. The proposed form of the potential is a combination of bond length (two-body), angle bend (three-body), and torsion (four-body) terms. This empirical model has been used by Guo et al.[184] in the analysis of crystal structures of C_{60} and C_{70}, and by Tuzun et al.[185,186] in the analysis of carbon NT filled with fluid and inert gas atoms. Like the MM2/MM3 model, this force field covers a wide range of nonmetallic main group elements.

Another class of empirical potentials for CNT is characterized by the quantum-mechanical concept of bond order formalism originally introduced by Abell.[187] An alternate interpretation of this formalism can also be found in Reference 188. Using a Morse-type potential, Abell showed that the degree of bonding universality can be well maintained in molecular modeling for similar elements. Tersoff[132–135] introduced this important concept for the modeling of Group IV elements such as C, Si, and Ge, and reasonably accurate results were reported. In Tersoff–Abell bond order formalism, the energy of the system is a sum of the energy on each bond. The energy of each bond is composed of a repulsive part and attractive part. A bond order function is embedded in the formulation. The bond order depends on the local atomic environment such as angular dependency due to the bond angles. Nordlund et al.[189] modified the Tersoff

potential such that the interlayer interaction is also considered. Brenner[35] made further improvements to the Tersoff potential by introducing additional terms into the bond order function. The main purpose of these extra terms is to correct the overbinding of radicals. Compared with the Tersoff potential, Brenner's potential shows robustness in the treatment of conjugacy; and it allows for forming and breaking of the bond with the correct representation of bond order. Brenner's potential has enjoyed success in the analysis of formation of fullerenes and their properties,[34,190–192] surface patterning,[193] indentation and friction at nanoscale,[194–203] and energetics of nanotubes.[34] An improved version of Brenner's potential has recently been proposed.[188,204] Based on the approximation of the many-atom expansion for the bond order within the two-center, orthogonal tight-binding (TB) model. Pettifor and Oleinik[205,206] have derived analytical forms that handle structural differentiation and radical formation. The model can be thought of as semi-empirical as it is partly derived from TB. Application of this model to hydrocarbon systems can be found in Reference 205. Depending on the range of applicability, a careful selection of potential model for a specific problem is needed.

19.4.2.2 Interlayer Potentials

Another important aspect of modeling in the analysis of CNT systems is the interlayer interaction. There are two major functional forms used in the empirical model: the inverse power model and the Morse function model. A very widely used inverse power model, the Lennard–Jones (LJ) potential, was introduced by Lennard–Jones[207,208] for atomic interactions:

$$\mu(R_{ij}) = 4\varepsilon\left[\left(\frac{R}{R_{ij}}\right)^{12} - \left(\frac{R}{R_{ij}}\right)^{6}\right] \tag{19.37}$$

where R_{ij} denotes the interatomic distance between atoms i and j, σ is the collision diameter (the inter-atomic distance at which $\phi(R)$ is zero), and ε is the energy at the minimum in $\phi(R_{ij})$. This relationship is shown in Figure 19.26. In the figure, the energy u, interatomic distance R, and interatomic force F are all normalized as $u^* = u/\varepsilon$, $r^* = R_{ij}/R$, and $F^* = FR/\varepsilon$. The corresponding force between the two atoms as a function of interatomic distance is also shown in Figure 19.26 and can be expressed as:

$$F_{ij} = -\frac{\partial u(R_{ij})}{\partial R_{ij}} = 24\frac{\varepsilon}{R}\left[2\left(\frac{R}{R_{ij}}\right)^{13} - \left(\frac{R}{R_{ij}}\right)^{7}\right] \tag{19.38}$$

For the carbon–carbon system, the LJ potential energy has been treated by Girifalco and Lad[209,210] and is given as:
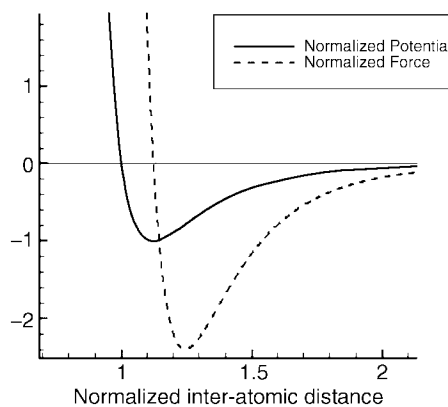

FIGURE 19.26 The pair potential and inter-atomic force in a two-atom system.

$$\phi_i = \frac{A}{\sigma^6}\left[\frac{1}{2}y_0^6\left(\frac{1}{\left(\frac{r_i}{\sigma}\right)^{12}} - \frac{1}{\left(\frac{r_i}{\sigma}\right)^6}\right)\right]$$

(19.39)

In Equation (19.39), σ is the bond length, y_0 is a dimensionless constant, and r_i is the distance between the ith atom pair. Two sets of parameters have been used: one for a graphite system[209] and the second for an fcc crystal composed of C_{60} molecules.[210] The converted parameters from the original data are given in Table 19.1.

TABLE 19.1 Model Parameters for LJ Potential

Parameter Source	A	Σ	y_0
LJ1 [209]	24.3×10^{-79} J•m^6	1.42 A	2.7
LJ2 [210]	32×10^{-79} J•m^6	1.42 A	2.742

Wang et al.[211] derived the following Morse-type potential for carbon systems based on local density approximations (LDA):

$$U(r) = D_e[(1 - e^{-\beta(r-r_e)})^2 - 1] + E_r e^{-\beta' r}$$

(19.40)

where $D_e = 6.50 \times 10^{-3}$ eV, is the equilibrium binding energy, $E_r = 6.94 \times 10^{-3}$ eV, is the hard-core repulsion energy, $r_e = 4.05$ Å, is the equilibrium distance between two carbon atoms, $\beta = 1.00/Å$, and $\beta' = 4.00/Å$. In a comparison study by Qian et al.,[212] it was found that the two LJ potentials yield much higher atomic forces in the repulsive region than the LDA potential; while in the attractive region, the LDA potential gives a much lower value of the binding energy than the two LJ potentials.

Further verification of this LDA potential is obtained by computing the equation of state (EOS) for a graphite system by assuming no relaxation within the graphene plane. The results are compared with published experimental data by Zhao and Spain[213] (referred to as EXP1) and by Hanfland et al. (referred to as EXP2),[214] and with the *ab initio* treatment (which included in-plane relaxation and treated an infinite crystal) by Boetgger.[215] The LDA model fits this experimental data and Boetger's model reasonably well. The LJ potential, in contrast, deviates strongly from the experimental high-pressure data for graphite (and Boettger's high-level computational treatment) where the relative volume is smaller (Figure 19.27). Based on this comparison, Qian et al.[212] Proposed to use LDA for interatomic distances less than 3.3 Å
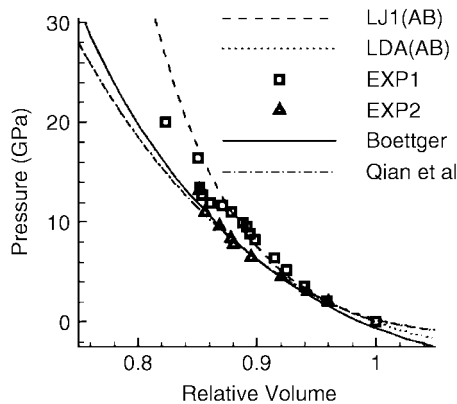

FIGURE 19.27 Comparison of EOS for graphite using different models with experimental data. (From Qian D, Liu WK, and Ruoff RS, (2001), Mechanics of c60 in nanotubes, *J. Phys. Chem. B.* 105: 10753–10758. With permission of Elsevier Science.)

and LJ for interatomic distance greater than 3.4 Å. The transition region is handled by curve fitting to ensure the continuity. A comparison of this model with the rest is also shown in Figure 19.27. Girifalco et al.[216] replaced the discrete sum of the atom pair potentials with a continuous surface integral. In their approach, different model parameters were derived for the cases of two parallel nanotubes and between C_{60} and nanotubes, although the LJ functional form is unchanged.

One of the major disadvantages of the potentials mentioned above is that the difference in interlayer binding energy of the AA and the AB stacking configurations for two rigid graphitic layers spaced at ~0.34 nm is probably not well represented; in short, the *corrugation* in the interlayer energy, due to the *pi* bonds projecting orthogonal to the plane of the layers, is not well captured. In addition, this registration effect also leads to unique nanoscale tribological features. Particularly, the corrugation between neighboring layers will play a central role in the friction present in such a nano-bearing system. The effects of interlayer registration between CNT and the surface it is sliding on have been studied recently in a number of interesting experiments by Falvo et al.[217–220] In these experiments, atomic force microscopy is used to manipulate the MWCNTs on the surface of graphite. A transition of slip-to-roll motion was reported as the MWCNT was moved to certain particular position. This phenomenon uncovers the effects of commensurance at the nanoscale. Both MD[221] and quasi-static simulation[222] have been performed to verify the experiments. Kolmogorov and Crespi[223] developed a new *registry-dependent graphitic potential* which accounts for the exponential atomic-core repulsion and the interlayer delocalization of π orbitals in addition to the normal two-body van der Waals attraction. This model derives an approximate 12 meV/atom difference between the AB stacking and the AA stacking. As discussed in Section 19.2.2.3, Yu et al.[82] applied this model to treat the mechanics of a free-standing twisted MWCNT observed experimentally. In more general settings than, for example, perfectly nested perfect cylinders or two perfectly parallel graphene sheets, the formulation of appropriate models of interlayer interactions remains an important challenge for modeling. Indeed at the nanoscale, the importance of surface interactions cannot be underestimated; and we envision further work by theoreticians and experimentalists to treat problems where some useful discussion between the two camps can be achieved.

19.4.3   Continuum and Multiscale Models

Despite constant increases in available computational power and improvement in numerical algorithms, even classical molecular dynamics computations are still limited to simulating on the order of 10^6–10^8 atoms for a few nanoseconds. The simulation of larger systems or longer times must currently be left to continuum methods. From the crystal elasticity approach in Section 19.2.4, one might immediately see the possibility of applying the finite element method (FEM) to the computational mechanics of nanotubes because the continuum concept of stress can be extracted from a molecular model. However, the fundamental assumption of the continuum approximation — that quantities vary slowly over lengths on the order of the atomic scales — breaks down in many of the most interesting cases of nanomechanics. Thus it would be very useful to have in hand a method that allows the use of a molecular dynamics-like method in localized regions, where quantities vary quickly on the atomic length scale, seamlessly blended with a continuum description of the surrounding material in which, presumably, small scale variations are unimportant or can be treated in an averaged sense.

Several promising methods have been developed toward this goal. The quasicontinuum method, introduced by Tadmor et al.[124,125] and extended and applied to several different problems over the last few years,[224–232] gives a theory for bridging the atomistic and continuum scales in quasistatic problems. In this method, a set of atoms L making up a Bravais lattice has selected from it a subset L_h. A triangulation of this subset allows the introduction of finite element-like shape functions $\varphi_h(\mathbf{l}_h)$ at lattice points $\mathbf{l}_h \in L_h$, allowing the interpolation of quantities at intermediate points in the lattice. For example, the deformed coordinates $\mathbf{q}$ at a lattice point $\mathbf{l}$ can be interpolated:

$$\mathbf{q}_h(\mathbf{l}) = \sum_{\mathbf{l}_h \in L_h} \varphi_h(\mathbf{l})\mathbf{q}_h(\mathbf{l}_h) \qquad (19.41)$$

In this way, the problem of the minimization of energy to find equilibrium configurations can be written in terms of a reduced set of variables. The equilibrium equations then take the form, at each reduced lattice point $\mathbf{l}_h$:

$$\mathbf{f}_h(\mathbf{l}_h) = \sum_{\mathbf{l} \in L} \mathbf{f}(\mathbf{l})\varphi_h(\mathbf{l}) = \mathbf{0} \tag{19.42}$$

The method is made practical by approximating summations over all atoms, as implied by the above equation, by using summation rules analogous to numerical quadrature. These rules rely on the smoothness of the quantities over the size of the triangulation to ensure accuracy. The final piece of the method is therefore the prescription of adaptivity rules, allowing the reselection of representative lattice points in order to tailor the computational mesh to the structure of the deformation field. The criteria for adaptivity are designed to allow full atomic resolution in regions of large local strain — for example, very close to a dislocation in the lattice.

The quasicontinuum method has been applied to the simulation of dislocations,[124,125,229,232] grain boundary interactions,[224,227] nanoindentation,[125,227 228] and fracture.[225,226] An extension of the method to finite temperatures has been proposed by Shenoy et al.[233] We have successfully extended the quasicontinuum method to the analysis of the nanotube (CNT) system, although careful treatment is needed. The major challenge in the simulation of CNTs using the quasicontinuum method is the fact that CNT is composed of atomic layers. The thickness of each layer is the size of one carbon atom. In this case, it can be shown that the direct application of the Cauchy–Born rule results in inconsistency in the mapping. Arroyo and Belytshko[234] corrected this inconsistent mapping by introducing the concept of exponential mapping from differential geometry. An alternate approach is to start with the variational principle and develop a method without the Cauchy–Born rule. We have developed the framework of this method with the introduction of a mesh-free approximation.[235–241] For a survey of mesh-free and particle methods and their applications, please see Reference 177; an online version of this paper can be found at http:// www.tam.nwu.edu/wkl/liu.html. In addition, two special journal issues[242,243] have been devoted to this topic. Odegard et al.[244] have proposed modeling a CNT as a continuum by equating the potential energy with that of the representative volume element (RVE). This assumption seems to be the same as that in the quasicontinuum method; however, the Born Rule is not used. The method has been recently applied in the constitutive modeling of CNT reinforced polymer composite systems.[245]

The mesh-free method has been directly applied by Qian et al.[212] in the modeling of a CNT interacting with C_{60}. The C_{60} molecule is, on the other hand, modeled with a molecular potential. The interaction between the C_{60} and the continuum is treated based on the conservation of momentum. The interaction forces on the CNT are obtained through the consistent treatment of the weak formulation.

In this approach, a continuous deformation mapping will be constructed through the mesh-free mapping function ϕ. The final form of the discrete equation can be shown to be:

$$f_l^{ext} + f_l^{int} + f_l^{inert} = 0 \tag{19.43}$$

The internal force term that is related to the internal energy is expressed as:

$$f_l^{int} = \sum_{l \in l} w_l f_i(\varphi(r, \theta)) \tag{19.44}$$

Another approach to the coupling of length scales is the FE/MD/TB model of Abraham et al.[246,247] In this method, three simulations are run simultaneously using finite element (FE), molecular dynamics (MD) and semi-empirical tight-binding (TB). Each simulation is performed on a different region of the domain, with a coupling imposed in *handshake* regions where the different simulations overlap. The method is designed for implementation on supercomputers via parallel algorithms, allowing the solution of large problems. One example of such a problem is the propagation of a crack in a brittle material.[246] Here, the TB method is used to simulate bond breaking at the crack tip, MD is used near the crack surface, and

the surrounding medium is treated with FE. This method has also been used by Nakano et al. in large-scale simulations of fracture.[248] Rafi-Tabar et al.[249,250] have presented a related method combining FE and MD for the simulation of crack propagation.

A related method, coarse-grained molecular dynamics (CGMD),[251,252] has been introduced as a replacement for finite elements in the FE/MD/TB simulations. In this approach, the continuum-level (or coarse-grained) energy is given by an ensemble average over the atomic motions in which the atomic positions are constrained to give the proper coarse-scale field. In this way, the fine-scale quantities that are not included in the coarse-scale motion are not neglected completely, as their thermodynamic average effect is retained.

We are currently developing a method for the coupling of continuum and MD simulations at finite temperature which, rather than enforcing coupling though boundary conditions in a hand-shake region, allows the continuum and MD representations to coexist in areas of interest in the computational domain. The methodology of the multiscale method can be traced back to the original paper by Liu et al.[253,254] and has been successfully applied in the multiple-scale problems involving strain localization,[255] boundary layers,[256] and coupling of finite elements with mesh-free shape functions.[257] In the current problem setting, this is done by writing a multiple-scale decomposition of the atomic displacements u_α in terms of finite element node displacements d_I and MD displacements d_α; the total scale is given by the usual finite element interpolation, plus the MD displacements, minus the projection of the MD displacements onto the finite element basis. Designating this projection operator as P:

$$u_\alpha = \sum_I N_I(x_\alpha)d_I + d_\alpha - Pd_\alpha \qquad (19.45)$$

where $N_I(x_\alpha)$ is the finite element shape function for node I evaluated at atom α. The key to the method is the subtraction of the projection of d_α, which we term the *bridging scale* and which allows for a unique decomposition into coarse and fine scales. With this decomposition, the Lagrangian (kinetic minus potential energies) can be written

$$L(d_I, \dot{d}_I, d_\alpha, \dot{d}_\alpha) = \sum_{I,J}\frac{1}{2}\dot{d}_I M_{IJ}\dot{d}_J + \sum\frac{1}{2}\dot{d}_\alpha M_{\alpha\beta}\dot{d}_\beta - U(d_I, d_\alpha) \qquad (19.46)$$

where M_{IJ} is the usual finite element mass matrix, $M_{\alpha B}$ is a fine-scale mass matrix, and U is the potential energy function. The equations of motion that can be derived from this Lagrangian are the usual finite element equation (plus a contribution to the internal force due to d_α), and the standard MD equations of motion (plus a driving term due to the continuum scale), i.e.,

$$\sum_J M_{IJ}\ddot{d}_J = -\frac{\partial U(d_I, d_\alpha)}{\partial d_I} \qquad (19.47a)$$

$$\sum_\beta M_{\alpha\beta}\ddot{d}_\beta = -\frac{\partial U(d_I, d_\alpha)}{\partial d_\alpha} \qquad (19.47b)$$

These equations can be solved using existing FE and MD codes along with suitable methods for exchanging information about internal forces and boundary conditions. An energy equation can also be derived by considering the continuum-level temperature to be described by the fluctuations in the fine-scale motions. Shown in Figure 19.28 is an example of implementing the multiscale method. It can be seen that the mesh-free discretization and MD coexist and are coupled in the fine-scale region. For the coarse-scale region, a mesh-free approximation is used. For the case shown in Figure 19.28, the error in the bending energy is less than 1% when compared with a purely MD approach. A systematic description of this method is to be described in an upcoming paper.[258]
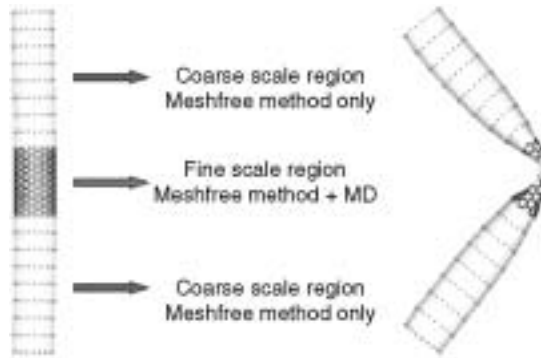
FIGURE 19.28 Multiscale analysis of carbon nanotube.

19.5 Mechanical Applications of Nanotubes

19.5.1 Nanoropes

As discussed in Section 19.2.3.2, the primary product of current methods of SWCNT synthesis contains not individual, separated SWCNTs, but rather bundles of closest-packed SWCNTs.[85,90] Load transfer to the individual SWCNTs in these bundles is of paramount importance for applications involving tensile load bearing. It is estimated that to achieve load transfer so that the full bundle cross-section would be participating in load bearing up to the intrinsic SWCNT breaking strength, the SWCNT contact length must be on the order of 10 to 120 microns. There is strong evidence, however, that the typical length of individual SWCNTs in such bundles is only about 300 nm.[111,112]

From continuum mechanics analysis of other types of wire or fiber forms,[259,260] it is found that twisting the wires or *weaving* the fibers can lead to a cable or rope that has much better load transfer mechanism in tension than a straight bundle would have. Compared with parallel wires, the major difference in terms of the mechanics of a wire rope is that wire ropes have a radial force (in the direction of vector **N** and **N'** as shown in Figure 19.29) that presses the surrounding wires to the core.

Correspondingly, the advantages of having wires in the form of a rope are

- A rope provides better load transfer and structural reliability. For example, when one wire component breaks, the broken sections of that particular wire can still bear load transferred from the other wires through the strong friction force that is a consequence of the radial compression.
- Wire rope has a smaller bending stiffness, therefore it is desirable for applications in which the rope has to be bent frequently. The fatigue life is significantly longer.
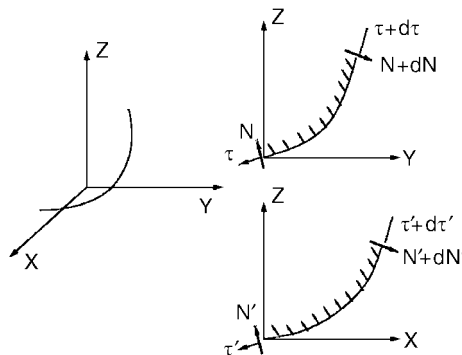- The radial force component gives the rope structure more stability than wires in parallel.

FIGURE 19.29 A three-dimensional section of a wire and force components in the *x-z* and *x-y* planes.

Based on preliminary modeling we have done of a seven-element twisted SWCNT bundle, it is believed that better load transfer in tension can be achieved by making nanoscale ropes and textiles of SWCNTs. We briefly describe some of these new mechanisms and issues below; a detailed analysis is given in Reference 261. We have used MD based on the empirical Tersoff–Brenner potential to analyze a bundle of SWCNTs under twist. A single strand composed of six (10,10) SWCNTs with length of 612 Å surrounding a core (10,10) tube is studied. Both ends of the core tube are fixed, and a twist around the center of the core on the six neighboring SWCNTs is applied at an angular velocity of 20π/ns (see Figure 19.30 for the cross-section before (a) and after (b) relaxation). The geometric parameters corresponding to the initial configuration are: $r = 6.78$ Å, $d = 3.44$ Å, $R = 2r+d = 17$ Å, $θ = π/3$.

Shown in Figure 19.31 are three snapshots of the deformation of the bundle after twisting is introduced. The corresponding change in the cross-section is shown in Figure 19.32 at the midpoint of the bundle. Clearly, radial deformation strongly depends on the twist angle. Further calculation[262] is performed on a bundle of SWCNTs with the same cross-sectional configuration but with a length of 153.72 Å. The total number of atoms is 17,500. Both ends of the core tube are fixed, and a twist around the center of the core on the six neighboring SWCNTs is applied to achieve a desired angle of twist. After this the whole twisted structure is relaxed to obtain the equilibrium configuration. A constant incremental displacement is then imposed on the core tube while holding the surrounding nanotubes fixed. Plotted in Figure 19.33 is the axial load transferred to the inner tube as a function of the twist angle. We use the transferred axial load as an index for the effectiveness of the load transfer mechanism. As can be seen in Figure 19.33, small twist has very little effect. For the case of 0 degrees (no twist), a force of only ~0.048 eV/Å is transferred to the center tube, and indication of a very smooth inter-tube contact condition; however, for a twist angle of 120 degrees, the transferred load increases to 1.63 eV/Å, about 34 times higher. Our calculation also indicates that too much twist results in unstable structures, i.e., the inner tube is being "squeezed out" when the twisting angle is 180 degrees or higher. This calculation clearly indicates that a great enhancement in the load transfer mechanism can be achieved by making the nanorope. More study on quantitatively determining the effects of various factors is under way.[261] For these significantly collapsed SWCNTs in highly twisted SWCNT bundles, the effective contact area is significantly increased; and this may contribute to better load transfer. In such twisted SWCNT bundles, the load transfer is likely enhanced by an expected increase in shear modulus due to the decrease in the interlayer separation. Recently, Pipes and Hubert[263] applied both textile mechanics and anisotropic elasticity to analyze polymer matrix composites consisting of discontinuous CNTs assembled in helical geometry. The effective elastic properties were predicted, and their study showed the strong dependence of the mechanical behavior on the helical angle of the assembly.
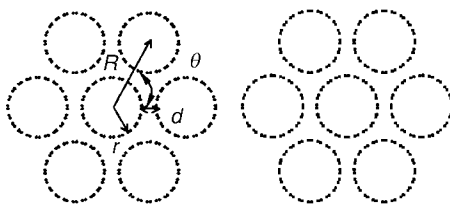

FIGURE 19.30   (Left) geometric parameters used in relaxed nanotube bundles. (Right) Configuration of bundled nanotubes after relaxation.

FIGURE 19.31   Snapshots of twisting of the SWCNT bundle. From a to f, the twisting angles are 30, 60, 90, 120, 150, and 180 degrees, respectively.
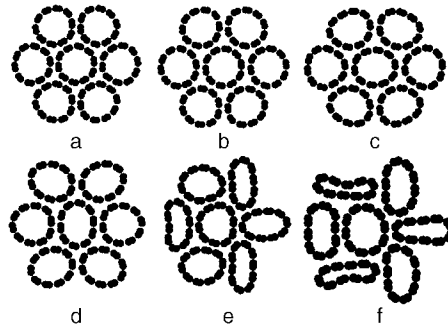
FIGURE 19.32 Change in cross-section at the midpoint of the SWNT bundle as a function of twist angle. From *a* to *f*, the twisting angles are 30, 60, 90, 120, 150, and 180 degrees, respectively.
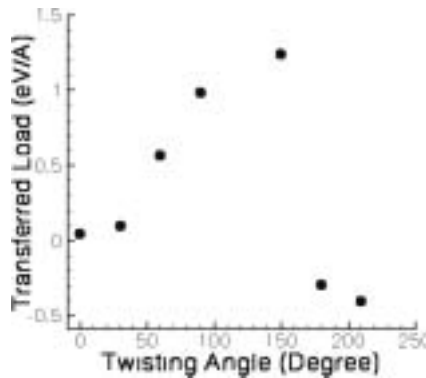

FIGURE 19.33 Transferred load as a function of twisting angle.

In the experiment (Figure 19.34), we attach the bundles using our previously developed nanoclamping methods (Figure 19.35)[11,29,264] and our new method of deposition of low electrical resistance W clamps. One goal involves measuring whether twisting enhances load transfer in terms of increased stiffness and strength. We measure the bundle stiffness without twisting, and then as a function of twisting, in the low-strain regime to assess the effective modulus of the bundle as a function of twist. To study the influence of twisting on strength, we will measure the load at break of similar diameter and length bundles with and without twisting, as a function of diameter, length, and number of twists. The boundary conditions also are assessed. We expect that the carbonaceous deposit made by electron beam-induced decomposition of residual hydrocarbons in the SEM, or the W deposit made, will (largely) be in contact with the outermost (perimeter) SWCNTs in the bundles. In untwisted perfect crystal SWCNT bundles having, for example, little load transfer to core SWCNTs from the perimeter SWCNTs, and with only perimeter SWCNTs clamped (from the method of deposition of our nanoclamp), we should be able to measure if load bearing and breakage occur only at the perimeter SWCNTs. We should be able to differentiate this from the load transfer we hypothesize will take
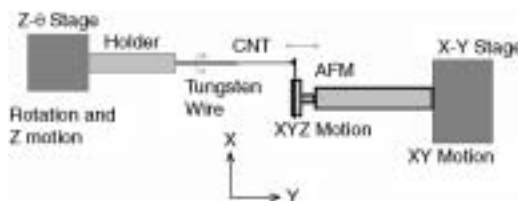

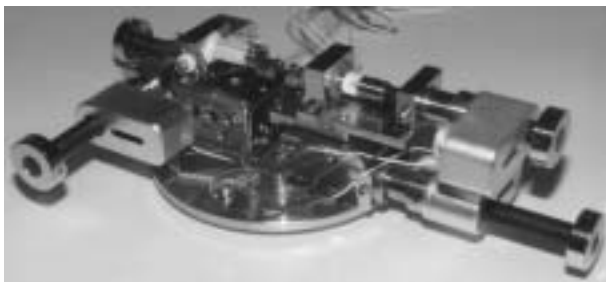**FIGURE 19.34** Proposed experimental stage for twisting the nanoropes.

FIGURE 19.35 Home-built nanomanipulation testing stage, which fits in the palm of the hand and is used in a high-resolution scanning electron microscopy. Further details are available in Yu et al., (2000), *J. Phys. Chem. B.* 104(37): 8764–8767; Yu et al., (2000), *Phys. Rev. Lett.* 84(24): 5552–5555; Yu et al., (2000), *Science.* 287(5453): 637–640.

place upon twisting. One method of monitoring such effects would be to simultaneously monitor the electrical conductivity of the bundle during mechanical loading.

We have recently been developing methods for simultaneous measurement of the electrical conductivity of nanofilaments spanning the opposing AFM tip cantilevers by using conductive AFM tip cantilevers and the W nanoclamp. We propose that such measurements will help to elucidate the dynamics of the nanobundle. The video recording allows for a time resolution of only ~1/30 of a second, the time between video frames. However, electrical conductivity can be measured on a much finer time scale; doing so may allow us to infer when individual SWCNTs have broken prior to the whole bundle breaking, to study interlayer interactions between SWCNTs in the bundle as a function of twisting, and to study changes in conductivity that occur simply due to mechanical deformation of individual tubes in the bundle. Mapping out the electromechanical response of SWCNT bundles as a function of compressive, tensile, and torsional, loading will provide a data base useful for assessing their application as actuators, sensors, and NEMS components. Measuring the electromechanical response in real applications such as cabling in a suspension bridge could also be a useful method of monitoring the reliability of nanorope components in everyday use.

19.5.2 Filling the Nanotubes

The mechanical benefits of filling nanotubes with various types of atoms are the following:

- Filling provides reinforcements for the hollow tube in the radial direction, thus preventing it from buckling, which, from the discussion in Section 19.2.2.3, is known to take place easily.
- Filling provides the smoothest and smallest nano-bearing system.
- Filling also provides an efficient storage system.

Currently there are two major experimental techniques that fill the CNT with foreign materials: arc evaporation, in which foreign materials are put in the anode for their incorporation into the CNTs formed from the carbon plasma, and opening the CNT by chemical agents followed by subsequent filling from either solution-based transport or by vapor transport. Because the chemical and physical environment in the solution-based filling method is less intensive, fragile materials such as biomaterials can also be put into the CNTs using that method.

Early attempts to make filled CNTs using arc evaporation have also resulted in filled carbon nanoparticles rather than filled CNTs. The foreign fillers include most metallic elements,[265–276] magnetic materials,[277–281] and radioactive materials,[282,283] surrounded by a carbon shell. One of the most well-known commercial applications of such filled nanoparticles is the invention of the so-called Technegas,[284,285] which is essentially radioactive material coated with carbon and used as an imaging agent in the detection of lung cancer.

A major breakthrough in filling CNTs was made by Ajayan et al.,[286,287] in which CNTs were opened by an oxidation process and foreign materials (molten lead in their case) were drawn into the CNT due to capillary action. This is the first experiment that showed the possibility of opening the CNT, although
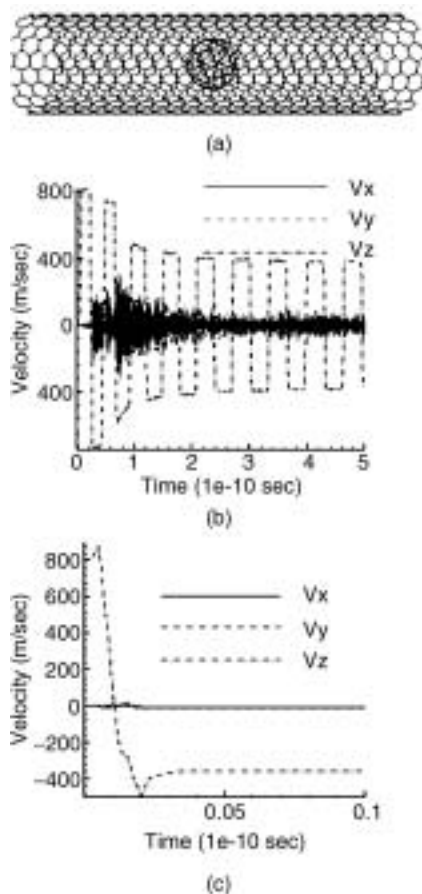
FIGURE 19.36 Computational modeling of C_{60} inside nanotubes. (a) The configuration for the problem. (b) The three velocity components history of the C_{60} as it shuttles through the (10,10) nanotube 20 times (Vz corresponds to the axial direction with an initial value of 0). (c) Same as (b) but for the case of an (8,8) nanotube. (From Wang Y, Tomanek D, and Bertsch GF, (1991), Stiffness of a solid composed of c60 clusters, *Phys. Rev. B.* 44(12): 6562–6565. With permission of Elsevier Science.)

the method used is not universally applicable. Numerous efforts have been undertaken along this direction, including combining oxidation with heating[287–289] and the use of liquid-based approaches, such as nitric acid,[290] hydrochloric acid,[291] or other oxidants.[292,293] Using these processes and the arc evaporation method, different types of materials were also incorporated into CNTs, e.g., compounds of metals or their carbides[268,290,294,295] and biological molecules,[296,297] hydrogen,[298] and argon.[299] Filling of SWCNTs was first reported by Sloan et al.[291,300] Experimental observation of fullerenes inside CNTs has also been reported by Smith et al.[301–303] and Burteaux et al.[304] using pulsed laser evaporation (PLV) of a graphite target containing a catalyst, and by Sloan et al.[305] and Zhang et al.[306] using arc vaporization of carbon with a mixed Ni/Y catalyst.

Filled CNTs have recently been treated by theory and modeling. Pederson et al.[307] discussed the capillary effect at the nanoscale. A major topic is the effect of the change in the dimensionality (from three-dimensional to one-dimensional) and scale (from macroscale to nanoscale) on the resulting physical properties. The effect of the size of the CNT as a geometric constraint on the crystallization process is discussed by Prasad et al.[308] Tuzun et al. studied flow of helium and argon[185] and mixed flow of helium and C_{60}[186] inside CNTs using MD. Berber et al.[309] studied various configurations of putting C_{60} inside a CNT using an *ab initio* method. Stan et al. presented analysis of the hydrogen storage problem.[310] The diffusion properties of molecular flow of methane, ethane, and ethylene inside CNTs were studied using MD by Mao et al.[311]

A general analysis of the statistical properties of the quasi-one-dimensional structure inside a filled CNT is treated by Stan et al.[312] The mechanics of C_{60} inside CNTs was studied by Qian, Liu, and Ruoff et al.[212] using MD simulation. An interesting phenomenon is observed in which C_{60} is sucked into the (10,10) or (9,9) SWCNTs by the sharp surface tension force present in the front of the open end, following which it then oscillates between the two open ends of the nanotube, never escaping. Moreover, the oscillation shows little decay after stabilizing after a few cycles. Both the C_{60} molecule and the nanotube show small deformations as a function of time and position. Furthermore, C_{60}, even when fired on axis with an initial speed up to 1600 m/sec, cannot penetrate into any of the (8,8), (7,7), (6,6) or (5,5) NTs. The simulation results suggest the possibility of using C_{60} in CNTs for making nanodevices such as nanobearings or nanopistons. We continue to study this nanocomposite of fullerenes in CNTs.

19.5.3 Nanoelectromechanical Systems (NEMS)

19.5.3.1 Fabrication of NEMS

Nanoelectromechanical systems (NEMS) are evolving, with new scientific studies and technical applications emerging. NEMS are characterized by small dimensions, where the dimensions are relevant for the function of the devices. Critical feature sizes may be from hundreds to a few nanometers. New physical properties, resulting from the small dimensions, may dominate the operation of the devices. Mechanical devices are shrinking in size to reduce mass, decrease response time, and increase sensitivity.

NEMS systems defined by photolithography processes are approaching the dimensions of carbon nanotubes. NEMS can be fabricated with various materials and integrated with multiphysics systems such as electronic, optical, and biological systems to create devices with new or improved functions. The new class of NEMS devices may provide a revolution in applications such as sensors, medical diagnostics, functional molecules, displays, and data storage. The initial research in science and technology related to nanomechanical systems is taking place now in a growing number of laboratories throughout the world.

The fabrication processes combine various micro/nanomachining techniques including micro/nano-structure fabrication and surface chemistry modification of such fabricated structures to allow site-specific placement of nanofilaments (NF) for actuation and sensing. Different kinds of NFs such as SWCNTs and MWCNTs, nanowhiskers (NWs), and etched nanostructures require different processing steps.

Controlled deposition of individual SWCNT on chemically functionalized templates was first introduced by Liu et al.[313] Reliable deposition of well-separated individual SWCNTs on chemically functionalized nanolithographic patterns was demonstrated. The approach offers promise in making structures and electronic circuits with nanotubes in predesigned patterns.

SWCNTs generally exist as bundles when purchased, so they have to be dispersed into individual SWCNTs in a solution before being used for device experimentation. One controllable procedure is done by diluting the SWCNT suspension into N, N-dimethylformamide (DMF) at a ratio of 1:100. The vial is then sonicated in a small ultrasonic bath for 4–8 hours. Such steps are repeated at least 3 times until the clear suspension contains at least 50% of the SWCNTs completely separated as individual SWCNTs (Figure 19.37).

Recently, Chung, Ruoff, and Lee[314] have developed new techniques for nanoscale gap fabrication (50–500nm) and the consecutive integration of CNTs. These techniques are essential for the batch assembly of CNTs (diameter ~ 10nm) for various applications.[29,264,315–319] Figure 19.38 shows an ideal configuration for chemical sensing by electromechanical transduction involving only a single CNT. So far, they have successfully deposited CNT bundles across the circular gap based on microlithography (Figure 19.39). The fabrication steps do not use serial and time-consuming processes such as e-beam lithography, showing the potential for batch production. It is also noted that these deposition steps were performed at standard environment conditions, thus providing more process freedom. Details of this new fabrication technique can be found in Reference 314.

19.5.3.2 Use of Nanotubes as Sensors in NEMS

The small size and unique properties of carbon nanotubes suggests that they can be used in sensor devices with unprecedented sensitivity. One route to make such sensors is to utilize the electrical properties of
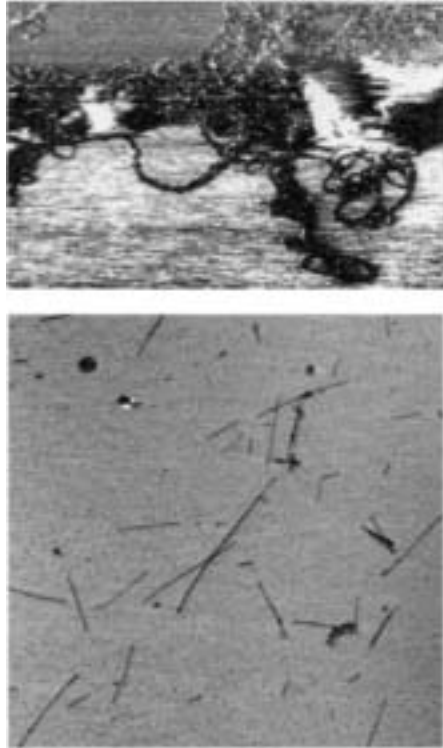
FIGURE 19.37 Before (upper) and after (lower) untangling the nanotubes in the suspension.
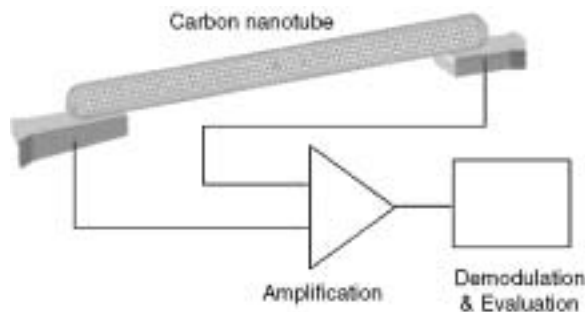

FIGURE 19.38 Carbon nanotube-based sensor.

CNTs. Experiment[320] and computation[321,322] have shown that the conductivity of CNTs can change by several orders of magnitude when deformed by the tip of an atomic force microscope. CNT chemical sensors have also been demonstrated: it has been found experimentally that the electrical resistance of a semiconducting SWCNT changes dramatically upon adsorption of certain gaseous molecules, such as NO_2, NH_3,[318] H_2,[323] and O_2.[317] This phenomenon has been modeled numerically by Peng and Cho[324] using a DFT–LDA technique.

The high sensitivity of the Raman spectra of CNTs to their environment also makes them useful as mechanical sensors. Raman spectra are known from experiment to give shifted peaks when CNTs undergo stress or strain.[325–327] This phenomenon has been used to detect phase transitions and to measure stress fields in polymers with embedded nanotubes.[328,329]

Yet another interesting application of nanotubes as sensors is through the use of the mechanical resonance frequency shift to detect adsorbed molecules or groups of molecules. When the mass of a
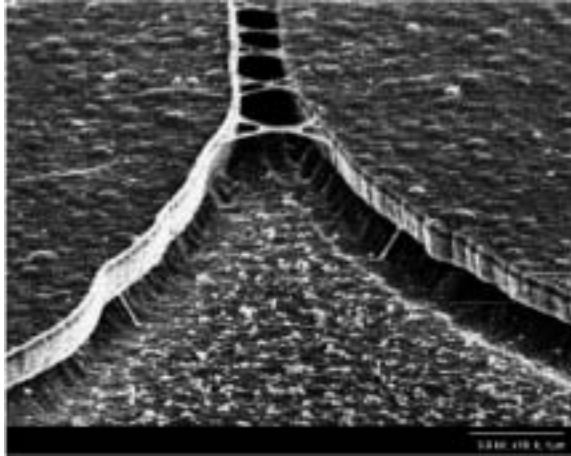
FIGURE 19.39 CNT deposition in a round gap by AC electrophoresis.

vibrating cantilever changes, as by the addition of an adsorbed body, the fundamental frequency of the cantilever as described by Equation (19.2) decreases. Ilic et al.[330] demonstrated micromachined silicon cantilevers with typical dimensions on the order of 20 μm × 320 nm × 100 μm to detect *E. coli* cells; the device was shown sensitive enough to detect as few as 16 cells under atmospheric conditions. Because the sensitivity of the device is hampered by the mechanical quality factor Q of the oscillating cantilever, even greater sensitivity might be expected in vacuum where the lack of air damping enables higher Q; of course, operation in vacuum limits the utility of the device. Shrinking the size of the design by using a carbon nanotube rather than a micromachined cantilever may give unprecedented sensitivity.

Poncharal et al.[44] were able to use the resonant frequency of a vibrating cantilevered nanotube (Figure 19.18) to estimate the mass of a ~30 fg carbon particle attached to the end of the tube. Our own calculations predict that detection of a 1% change in the resonant frequency of a 100-nm-long (10,10) CNT allows the measurement of an end mass of around 800 amu, approximately the mass of a single C_{60} molecule. The frequency shift of a vibrating cantilevered CNT due to an adsorbed mass at the free end can be estimated using beam theory (Section 19.2.2.2). To the first order approximation, the change in resonance frequency of mode i is

$$\Delta f_i = -\frac{2Mf_i}{\rho AL} \tag{19.48}$$

where M is the mass of the adsorbed body and ρ, A, and L are, respectively, the density, cross-sectional area, and length of the CNT. Sensitivity may be even further enhanced by taking advantage of critical points in the amplitude–frequency behavior of the vibrating CNT. For example, it is likely that the nonlinear force–deflection curve of the nanotube under certain conditions can result in a bistable response, as has been seen for other vibrating structures at this scale.[331,331a] Recently we have measured four parametric resonances of the fundamental mode of boron nanowires, the first observation of parametric resonance in a nanostructure.[332] It is likely that extraordinarily sensitive molecular sensors can be based on exploiting the parametric resonance of nanostructures (such as nanotubes, nanowires, or nanoplatelets).

19.5.4 Nanotube-Reinforced Polymer

The extremely high modulus and tunable electrical and thermal properties of carbon nanotubes offer an appealing mechanism to dramatically improve both strength and stiffness characteristics, as well as add multifunctionality to polymer-based composite systems. Experimental results to date, however, demonstrate

only modest improvements in important material properties amidst sometimes contradictory data.[333–337] Much of the discrepancy in the published results can be attributed to nonuniformity of material samples. In order to obtain optimal property enhancement, key issues to be resolved include improved dispersion of nanotubes, alignment of nanotubes, functionalization of the nanotubes to enhance matrix bonding/load transfer, and efficient use of the different types of nanotube reinforcements (single-wall vs. nanorope vs. multi-wall).

Ongoing investigations are focusing on improved processing and design of nanocomposites with emphasis on controlled nanotube geometric arrangement. Techniques to obtain homogeneous dispersion and significant alignment of the nanotubes include application of electric field during polymerization, extrusion, and deformation methods.[338–340] In addition to dispersion and alignment, recent work[341,342] has demonstrated that the waviness of the nanotubes (see Figure 19.40) in the polymer decreases the potential reinforcing factor by an additional 50% beyond a twofold decrease due to random orientation.

Among the encouraging results is work by Qian[335] for a MWCNT-reinforced polymer, where good dispersion and matrix bonding was achieved. In this case, using only 0.5 vol% nanotube reinforcement with no alignment and moderate NT waviness, elastic stiffness was improved 40% over that of the neat matrix material; and strength values improved nearly 25%. Figure 19.40 shows nanotubes bridging a

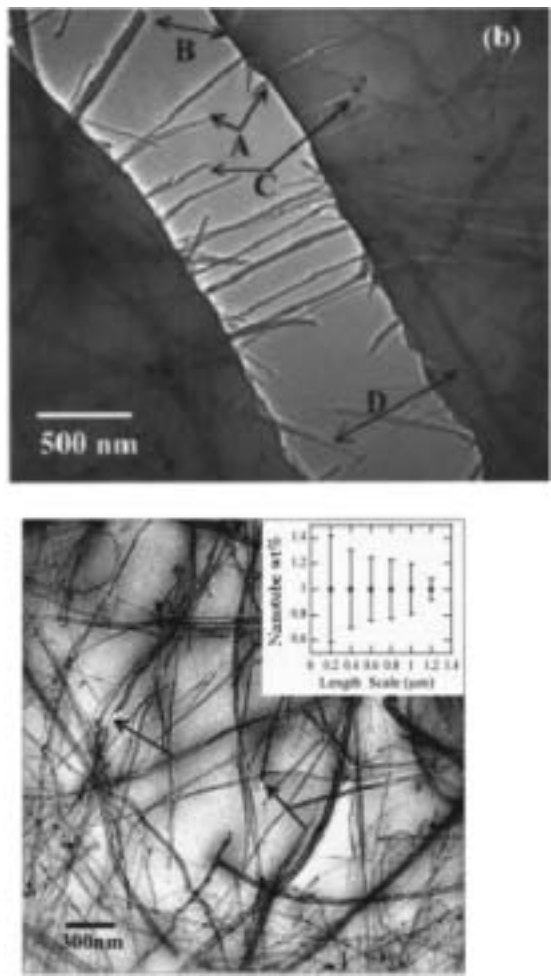**FIGURE 19.40**   Upper: *In situ* TEM image of crack in polystyrene film with nanotubes bridging the crack. Lower: arrangement of nanotubes in polymer, good dispersion, random orientation, and moderate waviness. (From Qian D, Dickey EC, Andrews R, and Rantell T, (2000), Load transfer and deformation mechanisms in carbon nanotube–polystyrene composites, *Appl. Phys. Lett.* 76(20): 2868–2870. With permission.)
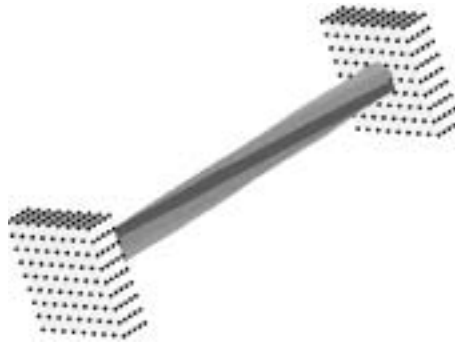
FIGURE 19.41   Multiscale analysis of nanorope-reinforced materials.

matrix crack and demonstrates excellent bonding between nanotubes and matrix material. Viscoelastic properties have also been investigated, with some evidence that well-dispersed nanotubes impact the mobility of the polymer chains themselves, causing changes in glass transition temperature and relaxation characteristics,[343,344] a feature not observed in polymers with a micron-sized reinforcing phase. Limited work on electrical properties shows that percolation can be reached with nanotube volume fractions of less than 1%,[333] leading to dramatic changes in electrical response of the polymer. This enables applications such as polymer coatings with electrostatic discharge capability.[345]

Understanding the mechanisms involved and the degree of property improvement possible for nanotube-reinforced polymers remains a goal of intensive research. Current work emphasizes surface modification of CNTs; control of matrix–NT adhesion; processing methods to control nanotube geometry; hybridization of nanoscale and microscale reinforcements; multifunctional capabilities; and integration of atomistic, micromechanics, and continuum modeling for predictive capability and understanding.

The multiscale method described in Section 19.4.3 shows great potential in the analysis and modeling of nanotube-reinforced material. Shown in Figure 19.41 is an illustration of the approach, combined with the nanorope application discussed in Section 19.5.1. In this method, the domain of the problem is decomposed into three regions: (1) the coarse-scale region, (2) the coupling-scale region, and (3) the fine-scale region. We will solve the coupled equation (Equations (19.47a and 19.47b)) based on the area of interest. A unique advantage of this method is the multiscale decomposition of the displacement field. The governing equations for continuum scale and molecular scale are unified and no special treatment is needed in handling the transition. More details of the modeling approach is included in Reference 346.

19.6   Conclusions

The development of successful methods for the synthesis of high-quality CNTs[85] has led to a worldwide R&D effort in the field of nanotubes. Part of the focus in this paper has been to address the particularly promising mechanical attributes of CNTs as indicated in numerous experiments, with emphasis on the inherent high stiffness and strength of such nanostructures. As stated in Section 19.3.3, much work still remains on the experimental measurement of the mechanical properties of CNTs. Progress made on the theoretical and computational fronts has also been briefly summarized.

It is amazing to see the applicability of continuum elasticity theory even down to the nanometer scale, although this fact should not lead to overconfidence in its use or to any ignorance of the physics that lies beneath. There are also a lot of unresolved issues in theoretical analysis and simulation due to the highly cross-disciplinary nature of the problem. In fact, numerous research efforts are under way in developing multiscale multiphysics simulation schemes. These efforts depend largely on gaining a basic understanding of the phenomena from the quantum level to the continuum level. Therefore, the terms *nanomechanics* or *nanoscale mechanics* indeed go beyond the nanoscale and serve as a manifestation of the link between fundamental science and important engineering applications. This is a major challenge

for the engineering community as well as the science community in the sense that the traditional boundary of each field has to be redefined to establish the new forefront of nanotechnology. A number of applications that are described in Section 19.5 serve as the best examples. Yet there are still numerous other likely applications of CNTs that we would like to mention; for instance, there has also been interesting research on the use of CNTs as ferroelectric devices, nanofluidic devices, and energy storage devices; and there exists the possibility of their use in biosurgical instruments. We have not been able to address these topics due to time and space limitations.

As we try to give an up-to-date status of the work that has been done, the field is rapidly evolving, and a tremendous amount of information can be found from various media. It is conceivable that the discovery of carbon nanotubes and other multifunctional nanostructures will parallel the importance of the transistor in technological impact. The size and the mechanical, electrical, thermal, and chemical properties of CNTs — as well as the fact that they are hollow and that matter can thus be located inside them and transported through them — have suggested an astonishingly wide array of potential applications, many of which are under testing now. Statements[347] are being made about factories being set up with ton-level production capabilities. We believe the unique structure and properties of CNTs and related nanomaterials will bring a fundamental change to technology.

Acknowledgments

References

1. Iijima S, (1991), Helical microtubules of graphitic carbon, *Nature*. 354(6348): 56–58.
2. Normile D, (1999), Technology — nanotubes generate full-color displays, *Science*. 286(5447): 2056–2057.
3. Choi WB, Chung DS, Kang JH, Kim HY, Jin YW, Han IT, Lee YH, Jung JE, Lee NS, Park GS, and Kim JM, (1999), Fully sealed, high-brightness carbon-nanotube field-emission display, *Appl. Phys. Lett.* 75(20): 3129–3131.
4. Bachtold A, Hadley P, Nakanishi T, and Dekker C, (2001), Logic circuits with carbon nanotube transistors, *Science*. 294(5545): 1317–1320.
5. Derycke V, Martel R, Appenzeller J, and Avouris P, (2001), Carbon nanotube inter- and intramolecular logic gates, *Nano Lett.* 10.1021/n1015606f.
6. Baughman RH, Cui CX, Zakhidov AA, Iqbal Z, Barisci JN, Spinks GM, Wallace GG, Mazzoldi A, De Rossi D, Rinzler AG, Jaschinski O, Roth S, and Kertesz M, (1999), Carbon nanotube actuators, *Science*. 284(5418): 1340–1344.
7. Harris PJF, (1999), *Carbon Nanotube and Related Structures: New Materials for the 21st Century*. Cambridge University Press. Cambridge, UK.
8. Dresselhaus MS, Dresselhaus, G, Eklund, PC, (1996), *Science of Fullerenes and Carbon Nanotubes*. Academic Press. San Diego.
9. Dresselhaus MS and Avouris P, (2001), Introduction to carbon materials research, *Carbon Nanotubes*, 1–9.

10. Brown TLL, Bursten BE, and Lemay HE, (1999), *Chemistry: The Central Science*. 8th ed. Prentice Hall. PTR.

11. Yu MF, Yakobson BI, and Ruoff RS, (2000), Controlled sliding and pullout of nested shells in individual multi-walled carbon nanotubes, *J. Phys. Chem. B.* 104(37): 8764–8767.

12. Saito R, Fujita M, Dresselhaus G, and Dresselhaus MS, (1992), Electronic-structure of chiral graphene tubules, *Appl. Phys. Lett.* 60(18): 2204–2206.

13. Dresselhaus MS, Dresselhaus G, and Saito R, (1995), Physics of carbon nanotubes, *Carbon.* 33(7): 883–891.

14. Fujita M, Saito R, Dresselhaus G, and Dresselhaus MS, (1992), Formation of general fullerenes by their projection on a honeycomb lattice, *Phys. Rev. B.* 45(23): 13834–13836.

15. Dresselhaus MS, Dresselhaus, G, Eklund, PC, (1993), Fullerenes, *J. Mater. Res.* 8: 2054.

16. Yuklyosi K, Ed. (1977), *Encyclopedic Dictionary of Mathematics*. The MIT Press. Cambridge.

17. Iijima S, (1993), Growth of carbon nanotubes, *Mater. Sci. Eng. B Solid State Mater. Adv. Technol.* 19(1–2): 172–180.

18. Dravid VP, Lin X, Wang Y, Wang XK, Yee A, Ketterson JB, and Chang RPH, (1993), Buckytubes and derivatives — their growth and implications for buckyball formation, *Science.* 259(5101): 1601–1604.

19. Iijima S, Ichihashi T, and Ando Y, (1992), Pentagons, heptagons and negative curvature in graphite microtubule growth, *Nature.* 356(6372): 776–778.

20. Saito Y, Yoshikawa T, Bandow S, Tomita M, and Hayashi T, (1993), Interlayer spacings in carbon nanotubes, *Phys. Rev. B.* 48(3): 1907–1909.

21. Zhou O, Fleming RM, Murphy DW, Chen CH, Haddon RC, Ramirez AP, and Glarum SH, (1994), Defects in carbon nanostructures, *Science.* 263(5154): 1744–1747.

22. Kiang CH, Endo M, Ajayan PM, Dresselhaus G, and Dresselhaus MS, (1998), Size effects in carbon nanotubes, *Phys. Rev. Lett.* 81(9): 1869–1872.

23. Amelinckx S, Bernaerts D, Zhang XB, Vantendeloo G, and Vanlanduyt J, (1995), A structure model and growth-mechanism for multishell carbon nanotubes, *Science.* 267(5202): 1334–1338.

24. Lavin JG, Subramoney S, Ruoff RS, Berber S, and Tomanek D, (2001), Scrolls and nested tubes in multiwall carbon tubes, unpublished.

25. Ajayan PM and Ebbesen TW, (1997), Nanometre-size tubes of carbon, *Rep. Prog. Phys.* 60(10): 1025–1062.

26. Amelinckx S, Lucas A, and Lambin P, (1999), Electron diffraction and microscopy of nanotubes, *Rep. Prog. Phys.* 62(11): 1471–1524.

27. Lourie O and Wagner HD, (1998), Evaluation of Young's modulus of carbon nanotubes by micro-Raman spectroscopy, *J. Mater. Res.* 13(9): 2418–2422.

28. Yu MF, Files BS, Arepalli S, and Ruoff RS, (2000), Tensile loading of ropes of single wall carbon nanotubes and their mechanical properties, *Phys. Rev. Lett.* 84(24): 5552–5555.

29. Yu MF, Lourie O, Dyer MJ, Moloni K, Kelly TF, and Ruoff RS, (2000), Strength and breaking mechanism of multi-walled carbon nanotubes under tensile load, *Science.* 287(5453): 637–640.

30. Overney G, Zhong W, and Tomanek D, (1993), Structural rigidity and low-frequency vibrational-modes of long carbon tubules, *Zeitschr. Phys. D-Atoms Molecules Clusters.* 27(1): 93–96.

31. Treacy MMJ, Ebbesen TW, and Gibson JM, (1996), Exceptionally high Young's modulus observed for individual carbon nanotubes, *Nature.* 381(6584): 678–680.

32. Tibbetts GG, (1984), Why are carbon filaments tubular? *J. Crystal Growth.* 66(3): 632–638.

33. Ruoff RS and Lorents DC, (1995), Mechanical and thermal properties of carbon nanotubes, *Carbon.* 33(7): 925–930.

34. Robertson DH, Brenner DW, and Mintmire JW, (1992), Energetics of nanoscale graphitic tubules, *Phys. Rev. B.* 45(21): 12592–12595.

35. Brenner DW, (1990), Empirical potential for hydrocarbons for use in simulating the chemical vapor deposition of diamond films, *Phys. Rev. B.* 42(15): 9458–9471.

36. Gao GH, Cagin T, and Goddard WA, (1998), Energetics, structure, mechanical and vibrational properties of single-walled carbon nanotubes, *Nanotechnology*. 9(3): 184–191.

37. Yakobson BI, Brabec CJ, and Bernholc J, (1996), Nanomechanics of carbon tubes: instabilities beyond linear response, *Phys. Rev. Lett.* 76(14): 2511–2514.

38. Timoshenko S and Gere J, (1988), *Theory of Elastic Stability*. McGraw-Hill. New York.

39. Lu JP, (1997), Elastic properties of carbon nanotubes and nanoropes, *Phys. Rev. Lett.* 79(7): 1297–1300.

40. Yao N and Lordi V, (1998), Young's modulus of single-walled carbon nanotubes, *J. Appl. Phys.* 84(4): 1939–1943.

41. Hernandez E, Goze C, Bernier P, and Rubio A, (1998), Elastic properties of c and bxcynz composite nanotubes, *Phys. Rev. Lett.* 80(20): 4502–4505.

42. Zhou X, Zhou JJ, and Ou-Yang ZC, (2000), Strain energy and Young's modulus of single-wall carbon nanotubes calculated from electronic energy-band theory, *Phys. Rev. B*. 62(20): 13692–13696.

43. Yakobson BI and Smalley RE, (1997), Fullerene nanotubes: C-1000000 and beyond, *Am. Sci.* 85(4): 324–337.

44. Poncharal P, Wang ZL, Ugarte D, and de Heer WA, (1999), Electrostatic deflections and electro-mechanical resonances of carbon nanotubes, *Science*. 283(5407): 1513–1516.

45. Liu JZ, Zheng Q, and Jiang Q, (2001), Effect of a rippling mode on resonances of carbon nanotubes, *Phys. Rev. Lett.* 86(21): 4843–4846.

46. Krishnan A, Dujardin E, Ebbesen TW, Yianilos PN, and Treacy MMJ, (1998), Young's modulus of single-walled nanotubes, *Phys. Rev. B*. 58(20): 14013–14019.

47. Yu MF, Dyer MJ, Chen J, and Bray K (2001), Multiprobe nanomanipulation and functional assembly of nanomaterials inside a scanning electron microscope. *Intl. Conf. IEEE-NANO2001*, Maui.

48. Wong EW, Sheehan PE, and Lieber CM, (1997), Nanobeam mechanics: elasticity, strength, and toughness of nanorods and nanotubes, *Science*. 277(5334): 1971–1975.

49. Salvetat JP, Kulik AJ, Bonard JM, Briggs GAD, Stockli T, Metenier K, Bonnamy S, Beguin F, Burnham NA, and Forro L, (1999), Elastic modulus of ordered and disordered multi-walled carbon nanotubes, *Adv. Mater.* 11(2): 161–165.

50. Salvetat JP, Briggs GAD, Bonard JM, Bacsa RR, Kulik AJ, Stockli T, Burnham NA, and Forro L, (1999), Elastic and shear moduli of single-walled carbon nanotube ropes, *Phys. Rev. Lett.* 82(5): 944–947.

51. Govindjee S and Sackman JL, (1999), On the use of continuum mechanics to estimate the properties of nanotubes, *Solid State Comm.* 110(4): 227–230.

52. Harik VM, (2001), Ranges of applicability for the continuum-beam model in the mechanics of carbon-nanotubes and nanorods, *Solid State Comm.* 120(331–335).

53. Harik VM, (2001), Ranges of applicability for the continuum-beam model in the constitutive analysis of carbon-nanotubes: nanotubes or nano-beams? in NASA/CR-2001–211013, also in *Computational Material Science* (Submitted).

54. Ru CQ, (2000), Effect of van der Waals forces on axial buckling of a double-walled carbon nanotube, *J. Appl. Phys.* 87(10): 7227–7231.

55. Ru CQ, (2000), Effective bending stiffness of carbon nanotubes, *Phys. Rev. B*. 62(15): 9973–9976.

56. Ru CQ, (2000), Column buckling of multi-walled carbon nanotubes with interlayer radial displacements, *Phys. Rev. B*. 62(24): 16962–16967.

57. Ru CQ, (2001), Degraded axial buckling strain of multi-walled carbon nanotubes due to interlayer slips, *J. Appl. Phys.* 89(6): 3426–3433.

58. Ru CQ, (2001), Axially compressed buckling of a double-walled carbon nanotube embedded in an elastic medium, *J. Mech. Phys. Solids*. 49(6): 1265–1279.

59. Ru CQ, (2000), Elastic buckling of single-walled carbon nanotube ropes under high pressure, *Phys. Rev. B*. 62(15): 10405–10408.

60. Bernholc J, Brabec C, Nardelli MB, Maiti A, Roland C, and Yakobson BI, (1998), Theory of growth and mechanical properties of nanotubes, *App. Phys. A — Mater. Sci. Proc.* 67(1): 39–46.

61. Yakobson BI and Avouris P, (2001), Mechanical properties of carbon nanotubes, in *Carbon Nanotubes*, 287–327.

62. Qian D, Liu WK, and Ruoff RS, (2002), Bent and kinked multi-shell carbon nanotubes — treating the interlayer potential more realistically. *43rd AIAA/ASME/ASCE/AHS Struct., Struct. Dynamics, Mater. Conf.* Denver, CO.

63. Iijima S, Brabec C, Maiti A, and Bernholc J, (1996), Structural flexibility of carbon nanotubes, *J. Chem. Phys.* 104(5): 2089–2092.

64. Ruoff RS, Lorents DC, Laduca R, Awadalla S, Weathersby S, Parvin K, and Subramoney S, (1995), *Proc. Electrochem. Soc.* 95–10: 557–562.

65. Subramoney S, Ruoff RS, Laduca R, Awadalla S, and Parvin K, (1995), *Proc. Electrochem. Soc.* 95–10: 563–569.

66. Falvo MR, Clary GJ, Taylor RM, Chi V, Brooks FP, Washburn S, and Superfine R, (1997), Bending and buckling of carbon nanotubes under large strain, *Nature.* 389(6651): 582–584.

67. Hertel T, Martel R, and Avouris P, (1998), Manipulation of individual carbon nanotubes and their interaction with surfaces, *J. Phys. Chem. B.* 102(6): 910–915.

68. Lourie O, Cox DM, and Wagner HD, (1998), Buckling and collapse of embedded carbon nanotubes, *Phys. Rev. Lett.* 81(8): 1638–1641.

69. Ruoff RS, Tersoff J, Lorents DC, Subramoney S, and Chan B, (1993), Radial deformation of carbon nanotubes by van der Waals forces, *Nature.* 364(6437): 514–516.

70. Tersoff J and Ruoff RS, (1994), Structural properties of a carbon-nanotube crystal, *Phys. Rev. Lett.* 73(5): 676–679.

70a. Lopez, MJ, Rubio A, Alonso JA, Qin LC, and Iijima S, (2001) Novel polygonized single-wall carbon nanotube bundles, *Phys. Rev. Lett.* 86(14): 3056–3059.

71. Chopra NG, Benedict LX, Crespi VH, Cohen ML, Louie SG, and Zettl A, (1995), Fully collapsed carbon nanotubes, *Nature.* 377(6545): 135–138.

72. Benedict LX, Chopra NG, Cohen ML, Zettl A, Louie SG, and Crespi VH, (1998), Microscopic determination of the interlayer binding energy in graphite, *Chem. Phys. Lett.* 286(5–6): 490–496.

73. Hertel T, Walkup RE, and Avouris P, (1998), Deformation of carbon nanotubes by surface van der Waals forces, *Phys. Rev. B.* 58(20): 13870–13873.

74. Avouris P, Hertel T, Martel R, Schmidt T, Shea HR, and Walkup RE, (1999), Carbon nanotubes: nanomechanics, manipulation, and electronic devices, *Appl. Surf. Sci.* 141(3–4): 201–209.

75. Yu MF, Dyer MJ, and Ruoff RS, (2001), Structure and mechanical flexibility of carbon nanotube ribbons: an atomic-force microscopy study, *J. Appl. Phys.* 89(8): 4554–4557.

76. Yu MF, Kowalewski T, and Ruoff RS, (2001), Structural analysis of collapsed, and twisted and collapsed, multi-walled carbon nanotubes by atomic force microscopy, *Phys. Rev. Lett.* 86(1): 87–90.

77. Lordi V and Yao N, (1998), Radial compression and controlled cutting of carbon nanotubes, *J. Chem. Phys.* 109(6): 2509–2512.

78. Shen WD, Jiang B, Han BS, and Xie SS, (2000), Investigation of the radial compression of carbon nanotubes with a scanning probe microscope, *Phys. Rev. Lett.* 84(16): 3634–3637.

79. Yu MF, Kowalewski T, and Ruoff RS, (2000), Investigation of the radial deformability of individual carbon nanotubes under controlled indentation force, *Phys. Rev. Lett.* 85(7): 1456–1459.

80. Chesnokov SA, Nalimova VA, Rinzler AG, Smalley RE, and Fischer JE, (1999), Mechanical energy storage in carbon nanotube springs, *Phys. Rev. Lett.* 82(2): 343–346.

81. Tang J, Qin LC, Sasaki T, Yudasaka M, Matsushita A, and Iijima S, (2000), Compressibility and polygonization of single-walled carbon nanotubes under hydrostatic pressure, *Phys. Rev. Lett.* 85(9): 1887–1889.

82. Yu MF, Dyer MJ, Chen J, Qian D, Liu WK, and Ruoff RS, (2001), Locked twist in multi-walled carbon nanotube ribbons, *Phys. Rev. B, Rapid Commn.* 64: 241403R.

83. Ebbesen TW and Ajayan PM, (1992), Large-scale synthesis of carbon nanotubes, *Nature.* 358(6383): 220–222.

84. Iijima S, Ajayan PM, and Ichihashi T, (1992), Growth model for carbon nanotubes, *Phys. Rev. Lett.* 69(21): 3100–3103.

85. Thess A, Lee R, Nikolaev P, Dai HJ, Petit P, Robert J, Xu CH, Lee YH, Kim SG, Rinzler AG, Colbert DT, Scuseria GE, Tomanek D, Fischer JE, and Smalley RE, (1996), Crystalline ropes of metallic carbon nanotubes, *Science.* 273(5274): 483–487.

86. Guo T, Nikolaev P, Thess A, Colbert DT, and Smalley RE, (1995), Catalytic growth of single-walled nanotubes by laser vaporization, *Chem. Phys. Lett.* 243(1–2): 49–54.

87. Kong J, Soh HT, Cassell AM, Quate CF, and Dai HJ, (1998), Synthesis of individual single-walled carbon nanotubes on patterned silicon wafers, *Nature.* 395(6705): 878–881.

88. Cassell AM, Raymakers JA, Kong J, and Dai HJ, (1999), Large-scale CVD synthesis of single-walled carbon nanotubes, *J. Phys. Chem. B.* 103(31): 6484–6492.

89. Li WZ, Xie SS, Qian LX, Chang BH, Zou BS, Zhou WY, Zhao RA, and Wang G, (1996), Large-scale synthesis of aligned carbon nanotubes, *Science.* 274(5293): 1701–1703.

90. Dal HJ, Rinzler AG, Nikolaev P, Thess A, Colbert DT, and Smalley RE, (1996), Single-wall nanotubes produced by metal-catalyzed disproportionation of carbon monoxide, *Chem. Phys. Lett.* 260(3–4): 471–475.

91. Nardelli MB, Yakobson BI, and Bernholc J, (1998), Brittle and ductile behavior in carbon nanotubes, *Phys. Rev. Lett.* 81(21): 4656–4659.

92. Walters DA, Ericson LM, Casavant MJ, Liu J, Colbert DT, Smith KA, and Smalley RE, (1999), Elastic strain of freely suspended single-wall carbon nanotube ropes, *Appl. Phys. Lett.* 74(25): 3803–3805.

93. Pan ZW, Xie SS, Lu L, Chang BH, Sun LF, Zhou WY, Wang G, and Zhang DL, (1999), Tensile tests of ropes of very long aligned multi-wall carbon nanotubes, *Appl. Phys. Lett.* 74(21): 3152–3154.

94. Wagner HD, Lourie O, Feldman Y, and Tenne R, (1998), Stress-induced fragmentation of multi-wall carbon nanotubes in a polymer matrix, *Appl. Phys. Lett.* 72(2): 188–190.

95. Li F, Cheng HM, Bai S, Su G, and Dresselhaus MS, (2000), Tensile strength of single-walled carbon nanotubes directly measured from their macroscopic ropes, *Appl. Phys. Lett.* 77(20): 3161–3163.

96. Yakobson BI, Campbell MP, Brabec CJ, and Bernholc J, (1997), High strain rate fracture and c-chain unraveling in carbon nanotubes, *Computational Mater. Sci.* 8(4): 341–348.

97. Belytschko T, Xiao SP, Schatz GC, and Ruoff RS, (2001), Simulation of the fracture of nanotubes, *Phys. Rev.* B, accepted.

98. Yakobson BI, (1997), in *Recent Advances in the Chemistry and Physics of Fullerenes and Related Materials*, Kadish KM (Ed.), Electrochemical Society, Inc., Pennington, NJ, 549.

99. Nardelli MB, Yakobson BI, and Bernholc J, (1998), Mechanism of strain release in carbon nanotubes, *Phys. Rev. B.* 57(8): R4277-R4280.

100. Srivastava D, Menon M, and Cho KJ, (1999), Nanoplasticity of single-wall carbon nanotubes under uniaxial compression, *Phys. Rev. Lett.* 83(15): 2973–2976.

101. Wei CY, Srivastava D, and Cho KJ, (2001), Molecular dynamics study of temperature-dependent plastic collapse of carbon nanotubes under axial compression, *Comp. Modeling Eng. Sci.* 3, 255.

102. Srivastava D, Wei CY, and Cho KJ, (2002) Computational nanomechanics of carbon nanotubes and composites, ASME, *Applied Mechanics Reviews* (special issue on nanotechnology), in press.

103. Yakobson BI, (1998), Mechanical relaxation and intramolecular plasticity in carbon nanotubes, *Appl. Phys. Lett.* 72(8): 918–920.

104. Zhang PH, Lammert PE, and Crespi VH, (1998), Plastic deformations of carbon nanotubes, *Phys. Rev. Lett.* 81(24): 5346–5349.

105. Zhang PH and Crespi VH, (1999), Nucleation of carbon nanotubes without pentagonal rings, *Phys. Rev. Lett.* 83(9): 1791–1794.

106. Bockrath M, Cobden DH, McEuen PL, Chopra NG, Zettl A, Thess A, and Smalley RE, (1997), Single-electron transport in ropes of carbon nanotubes, *Science.* 275(5308): 1922–1925.

107. Cumings J and Zettl A, (2000), Low-friction nanoscale linear bearing realized from multi-wall carbon nanotubes, *Science.* 289(5479): 602–604.

108. Kelly BT, (1981), *Physics of Graphite*. Applied Science. London.

109. Ausman KD and Ruoff RS, (2001), Unpublished.

110. Yakobson BI, (2001), Unpublished.

111. Geohegan DB, Schittenhelm H, Fan X, Pennycook SJ, Puretzky AA, Guillorn MA, Blom DA, and Joy DC, (2001), Condensed phase growth of single-wall carbon nanotubes from laser annealed nanoparticulates, *Appl. Phys. Lett.* 78(21): 3307–3309.

112. Piner RD and Ruoff RS, (2001), Unpublished.

113. Born M and Huang K, (1954), *Dynamical Theory of Crystal Lattices*. Oxford University Press. Oxford.

114. Keating PN, (1966), Theory of third-order elastic constants of diamond-like crystals, *Phys. Rev.* 149(2): 674.

115. Keating PN, (1966), Effect of invariance requirements on elastic strain energy of crystals with application to diamond structure, *Phys. Rev.* 145(2): 637.

116. Keating PN, (1967), On sufficiency of Born–Huang relations, *Phys. Lett. A.* A 25(7): 496.

117. Keating PN, (1968), Relationship between macroscopic and microscopic theory of crystal elasticity. 2. nonprimitive crystals, *Phys. Rev.* 169(3): 758.

118. Brugger K, (1964), Thermodynamic definition of higher order elastic coefficients, *Phys. Rev.* 133(6A): A1611.

119. Martin JW, (1975), Many-body forces in metals and brugger elastic-constants, *J. Phys. C — Solid State Phys.* 8(18): 2837–2857.

120. Martin JW, (1975), Many-body forces in solids and Brugger elastic-constants. 2. INNER elastic-constants, *J. Phys. C — Solid State Phys.* 8(18): 2858–2868.

121. Martin JW, (1975), Many-body forces in solids — elastic-constants of diamond-type crystals, *J. Phys. C — Solid State Phys.* 8(18): 2869–2888.

122. Daw MS and Baskes MI, (1984), Embedded-atom method — derivation and application to impurities, surfaces, and other defects in metals, *Phys. Rev. B.* 29(12): 6443–6453.

123. Daw MS, Foiles SM, and Baskes MI, (1993), The embedded-atom method — a review of theory and applications, *Mater. Sci. Rep.* 9(7–8): 251–310.

124. Tadmor EB, Ortiz M, and Phillips R, (1996), Quasicontinuum analysis of defects in solids, *Philos. Mag. A — Phys. Cond. Matter Struct. Defects Mech. Prop.* 73(6): 1529–1563.

125. Tadmor EB, Phillips R, and Ortiz M, (1996), Mixed atomistic and continuum models of deformation in solids, *Langmuir.* 12(19): 4529–4534.

126. Friesecke G and James RD, (2000), A scheme for the passage from atomic to continuum theory for thin films, nanotubes and nanorods, *J. Mech. Phys. Solids.* 48(6–7): 1519–1540.

127. Belytschko T, Liu WK, and Moran B, (2000), *Nonlinear Finite Elements for Continua and Structures*. John Wiley & Sons, LTD.

128. Marsden JE and Hughes TJR, (1983), *Mathematical Foundations of Elasticity*. Prentice-Hall. Englewood Cliffs, NJ.

129. Malvern LE, (1969), *Introduction to the Mechanics of a Continuous Medium*. Prentice-Hall. Englewood Cliffs, NJ.

130. Milstein F, (1982), Crystal elasticity, in *Mechanics of Solids*, Sewell MJ (Ed.), Pergamon Press, Oxford.

131. Ericksen JL, (1984), in *Phase Transformations and Material Instabilities in Solids*, Gurtin M (Ed.), Academic Press, New York.

132. Tersoff J, (1986), New empirical model for the structural properties of silicon, *Phys. Rev. Lett.* 56(6): 632–635.

133. Tersoff J, (1988), New empirical approach for the structure and energy of covalent systems, *Phys. Rev. B.* 37(12): 6991–7000.

134. Tersoff J, (1988), Empirical interatomic potential for carbon, with applications to amorphous-carbon, *Phys. Rev. Lett.* 61(25): 2879–2882.

135. Tersoff J, (1989), Modeling solid-state chemistry — interatomic potentials for multicomponent systems, *Phys. Rev. B.* 39(8): 5566–5568.

136. Green AE and Rivlin RS, (1964), Multipolar continuum mechanics, *Arch. Rat. Mech. An.* 17: 113–147.

137. Cousins CSG, (1978), Inner elasticity, *J. Phys. C — Solid State Phys.* 11(24): 4867–4879.

138. Zhang P, Huang Y, Geubelle PH, and Hwang KC, (2002), On the continuum modeling of carbon nanotubes. *Acta Mechanica Sinica.* (In press).

139. Zhang P, Huang Y, Geubelle PH, Klein P, and Hwang KC, (2002), The elastic modulus of single-wall carbon nanotubes: a continuum analysis incorporating interatomic potentials, *Intl. J. Solids Struct.* In press.

140. Zhang P, Huang Y, Gao H, and Hwang KC, (2002), Fracture nucleation in single-wall carbon nanotubes under tension: a continuum analysis incorporating interatomic potentials. *J. Appl. Mech.* (In press).

141. Wiesendanger R, (1994), *Scanning Probe Microscopy and Spectroscopy: Methods and Applications.* Cambridge University Press. Oxford.

142. Binnig G and Quate CF, (1986), Atomic force microscope, *Phys. Rev. Lett.* 56: 930–933.

143. Cumings J, Collins PG, and Zettl A, (2000), Materials — peeling and sharpening multi-wall nanotubes, *Nature.* 406(6796): 586–586.

144. Ohno K, Esfarjani K, and Kawazoe Y, (1999), *Computational Material Science: From Ab Initio to Monte Carlo Methods.* Solid State Sciences, Cardona M, et al. (Ed.) Springer. Berlin.

145. Dirac PAM, (1958), *The Principles of Quantum Mechanics.* Oxford University Press. London.

146. Landau LD and Lifshitz EM, (1965), *Quantum Mechanics; Non-Relativistic Theory.* Pergamon. Oxford.

147. Merzbacher E, (1998), *Quantum Mechanics.* Wiley. New York.

148. Messiah A, (1961), *Quantum Mechanics.* North-Holland. Amsterdam.

149. Schiff LI, (1968), *Quantum Mechanics.* McGraw-Hill. New York.

150. Fock V, (1930), Naherungsmethode zur losung des quantenmechanis-chen mehrkorperproblems, *Z. Physik.* 61: 126.

151. Hartree DR, (1928), The wave mechanics of an atom with a non-Coulomb central field, part I, theory and methods, *Proc. Cambridge Phil. Soc.* 24: 89.

152. Hartree DR, (1932–1933), A practical method for the numerical solution of differential equations, *Mem. and Proc. Manchester Lit. Phil. Soc.* 77: 91.

153. Clementi E, (2000), *Ab initio* computations in atoms and molecules (reprinted from *IBM Journal of Research and Development* 9, 1965), *IBM J. Res. Dev.* 44(1–2): 228–245.

154. Hohenberg P and Kohn W, (1964), Inhomogeneous electron gas, *Phys. Rev. B.* 136: 864.

155. Kohn W and Sham LJ, (1965), Self-consistent equations including exchange and correlation effects, *Phys. Rev.* 140(4A): 1133.

156. Perdew JP, McMullen ER, and Zunger A, (1981), Density-functional theory of the correlation-energy in atoms and ions — a simple analytic model and a challenge, *Phys. Rev. A.* 23(6): 2785–2789.

157. Perdew JP and Zunger A, (1981), Self-interaction correction to density-functional approximations for many-electron systems, *Phys. Rev. B.* 23(10): 5048–5079.

158. Slater JC, Wilson TM, and Wood JH, (1969), Comparison of several exchange potentials for electrons in cu+ ion, *Phys. Rev.* 179(1): 28.

159. Moruzzi VJ and Sommers CB, (1995), *Calculated Electronic Properties of Ordered Alloys: A Handbook.* World Scientific. Singapore.

160. Payne MC, Teter MP, Allan DC, Arias TA, and Joannopoulos JD, (1992), Iterative minimization techniques for *ab initio* total-energy calculations — molecular-dynamics and conjugate gradients, *Rev. Mod. Phys.* 64(4): 1045–1097.

161. Car R and Parrinello M, (1985), Unified approach for molecular-dynamics and density-functional theory, *Phys. Rev. Lett.* 55(22): 2471–2474.

162. Slater JC and Koster GF, (1954), Wave functions for impurity levels, *Phys. Rev.* 94(1498).

163. Harrison WA, (1989), *Electronic Structure and the Properties of Solids: The Physics of the Chemical Bond*. Dover. New York.

164. Matthew W, Foulkes C, and Haydock R, (1989), Tight-binding models and density-functional theory, *Phys. Rev. B.* 39(17): 12520–12536.

165. Xu CH, Wang CZ, Chan CT, and Ho KM, (1992), A transferable tight-binding potential for carbon, *J. Phys. Condensed Matter.* 4(28): 6047–6054.

166. Mehl MJ and Papaconstantopoulos DA, (1996), Applications of a tight-binding total-energy method for transition and noble metals: elastic constants, vacancies, and surfaces of monatomic metals, *Phys. Rev. B.* 54(7): 4519–4530.

167. Liu F, (1995), Self-consistent tight-binding method, *Phys. Rev. B.* 52(15): 10677–10680.

168. Porezag D, Frauenheim T, Kohler T, Seifert G, and Kaschner R, (1995), Construction of tight-binding-like potentials on the basis of density-functional theory — application to carbon, *Phys. Rev. B.* 51(19): 12947–12957.

169. Taneda A, Esfarjani K, Li ZQ, and Kawazoe Y, (1998), Tight-binding parameterization of transition metal elements from LCAO *ab initio* Hamiltonians, *Computational Mater. Sci.* 9(3–4): 343–347.

170. Menon M and Subbaswamy KR, (1991), Universal parameter tight-binding molecular-dynamics — application to c-60, *Phys. Rev. Lett.* 67(25): 3487–3490.

171. Sutton AP, Finnis MW, Pettifor DG, and Ohta Y, (1988), The tight-binding bond model, *J. Phys. C — Solid State Phys.* 21(1): 35–66.

172. Menon M and Subbaswamy KR, (1997), Nonorthogonal tight-binding molecular-dynamics scheme for silicon with improved transferability, *Phys. Rev. B.* 55(15): 9231–9234.

173. Haile JM, (1992), *Molecular Dynamics Simulation*. Wiley Interscience, New York.

174. Rapaport DC, (1995), *The Art of Molecular Dynamics Simulation*. Cambridge University Press, London.

175. Frenkel D and Smit, B., (1996), *Understanding Molecular Simulation: From Algorithms to Applications*. Academic Press, New York.

176. Hockney RW and Eastwood, J.W., (1989), *Computer Simulation Using Particles*. IOP Publishing Ltd. New York.

177. Li. SF and Liu WK, (2002), Mesh-free and particle methods, *Appl. Mech. Rev.* 55(1): 1–34.

178. Berendsen HJC and van Gunsteren W.F., (1986), *Dynamics Simulation of Statistical Mechanical Systems*, Ciccotti GPF, Hoover, W.G. (Eds.) Vol. 63. North Holland. Amsterdam. 493.

179. Verlet L, (1967), Computer experiments on classical fluids. I. Thermodynamical properties of Lennard-Jones molecules, *Phys. Rev.* 159(1): 98.

180. Gray SK, Noid DW, and Sumpter BG, (1994), Symplectic integrators for large-scale molecular-dynamics simulations — a comparison of several explicit methods, *J. Chem. Phys.* 101(5): 4062–4072.

181. Allinger NL, (1977), Conformational-analysis.130. MM2 — hydrocarbon force-field utilizing V1 and V2 torsional terms, *J. Am. Chem. Soc.* 99(25): 8127–8134.

182. Allinger NL, Yuh YH, and Lii JH, (1989), Molecular mechanics — the MM3 force-field for hydrocarbons. 1, *J. Am. Chem. Soc.* 111(23): 8551–8566.

183. Mayo SL, Olafson BD, and Goddard WA, (1990), Dreiding — a generic force-field for molecular simulations, *J. Phys. Chem.* 94(26): 8897–8909.

184. Guo YJ, Karasawa N, and Goddard WA, (1991), Prediction of fullerene packing in c60 and c70 crystals, *Nature.* 351(6326): 464–467.

185. Tuzun RE, Noid DW, Sumpter BG, and Merkle RC, (1996), Dynamics of fluid flow inside carbon nanotubes, *Nanotechnology.* 7(3): 241–246.

186. Tuzun RE, Noid DW, Sumpter BG, and Merkle RC, (1997), Dynamics of he/c-60 flow inside carbon nanotubes, *Nanotechnology.* 8(3): 112–118.

187. Abell GC, (1985), Empirical chemical pseudopotential theory of molecular and metallic bonding, *Phys. Rev. B*. 31(10): 6184–6196.

188. Brenner DW, (2000), The art and science of an analytic potential, *Physica Status Solidi B — Basic Res*. 217(1): 23–40.

189. Nordlund K, Keinonen J, and Mattila T, (1996), Formation of ion irradiation induced small-scale defects on graphite surfaces, *Phys. Rev. Lett*. 77(4): 699–702.

190. Brenner DW, Harrison JA, White CT, and Colton RJ, (1991), Molecular-dynamics simulations of the nanometer-scale mechanical properties of compressed buckminsterfullerene, *Thin Solid Films*. 206(1–2): 220–223.

191. Robertson DH, Brenner DW, and White CT, (1992), On the way to fullerenes — molecular-dynamics study of the curling and closure of graphitic ribbons, *J. Phys. Chem*. 96(15): 6133–6135.

192. Robertson DH, Brenner DW, and White CT, (1995), Temperature-dependent fusion of colliding c-60 fullerenes from molecular-dynamics simulations, *J. Phys. Chem*. 99(43): 15721–15724.

193. Sinnott SB, Colton RJ, White CT, and Brenner DW, (1994), Surface patterning by atomically-controlled chemical forces — molecular-dynamics simulations, *Surf. Sci*. 316(1–2): L1055-L1060.

194. Harrison JA, White CT, Colton RJ, and Brenner DW, (1992), Nanoscale investigation of indentation, adhesion and fracture of diamond (111) surfaces, *Surf. Sci*. 271(1–2): 57–67.

195. Harrison JA, White CT, Colton RJ, and Brenner DW, (1992), Molecular-dynamics simulations of atomic-scale friction of diamond surfaces, *Phys. Rev. B*. 46(15): 9700–9708.

196. Harrison JA, Colton RJ, White CT, and Brenner DW, (1993), Effect of atomic-scale surface-roughness on friction — a molecular-dynamics study of diamond surfaces, *Wear*. 168(1–2): 127–133.

197. Harrison JA, White CT, Colton RJ, and Brenner DW, (1993), Effects of chemically-bound, flexible hydrocarbon species on the frictional properties of diamond surfaces, *J. Phys. Chem*. 97(25): 6573–6576.

198. Harrison JA, White CT, Colton RJ, and Brenner DW, (1993), Atomistic simulations of friction at sliding diamond interfaces, *MRS Bull*. 18(5): 50–53.

199. Harrison JA and Brenner DW, (1994), Simulated tribochemistry — an atomic-scale view of the wear of diamond, *J. Am. Chem. Soc*. 116(23): 10399–10402.

200. Harrison JA, White CT, Colton RJ, and Brenner DW, (1995), Investigation of the atomic-scale friction and energy — dissipation in diamond using molecular-dynamics, *Thin Solid Films*. 260(2): 205–211.

201. Tupper KJ and Brenner DW, (1993), Atomistic simulations of frictional wear in self-assembled monolayers, *Abstr. Papers Am. Chem. Soc*. 206: 172.

202. Tupper KJ and Brenner DW, (1993), Molecular-dynamics simulations of interfacial dynamics in self-assembled monolayers, *Abstr. Papers Am. Chem. Soc*. 206: 72.

203. Tupper KJ and Brenner DW, (1994), Molecular-dynamics simulations of friction in self-assembled monolayers, *Thin Solid Films*. 253(1–2): 185–189.

204. Brenner DW, (2001), Unpublished.

205. Pettifor DG and Oleinik II, (1999), Analytic bond-order potentials beyond Tersoff-Brenner. Ii. Application to the hydrocarbons, *Phys. Rev. B*. 59(13): 8500.

206. Pettifor DG and Oleinik II, (2000), Bounded analytic bond-order potentials for sigma and pi bonds, *Phys. Rev. Lett*. 84(18): 4124–4127.

207. Jones JE, (1924), On the determination of molecular fields-I. From the variation of the viscosity of a gas with temperature, *Proc. R. Soc*. 106: 441.

208. Jones JE, (1924), On the determination of molecular fields-II. From the equation of state of a gas, *Proc. R. Soc*. 106: 463.

209. Girifalco LA and Lad RA, (1956), Energy of cohesion, compressibility and the potential energy functions of the graphite system, *J. Chem. Phys*. 25(4): 693–697.

210. Girifalco LA, (1992), Molecular-properties of c-60 in the gas and solid-phases, *J. Phys. Chem*. 96(2): 858–861.

211. Wang Y, Tomanek D, and Bertsch GF, (1991), Stiffness of a solid composed of c60 clusters, *Phys. Rev. B.* 44(12): 6562–6565.

212. Qian D, Liu WK, and Ruoff RS, (2001), Mechanics of c60 in nanotubes, *J. Phys. Chem. B.* 105: 10753–10758.

213. Zhao YX and Spain IL, (1989), X-ray-diffraction data for graphite to 20 gpa, *Phys. Rev. B.* 40(2): 993–997.

214. Hanfland M, Beister H, and Syassen K, (1989), Graphite under pressure — equation of state and first-order Raman modes, *Phys. Rev. B.* 39(17): 12598–12603.

215. Boettger JC, (1997), All-electron full-potential calculation of the electronic band structure, elastic constants, and equation of state for graphite, *Phys. Rev. B.* 55(17): 11202–11211.

216. Girifalco LA, Hodak M, and Lee RS, (2000), Carbon nanotubes, buckyballs, ropes, and a universal graphitic potential, *Phys. Rev. B.* 62(19): 13104–13110.

217. Falvo MR, Clary G, Helser A, Paulson S, Taylor RM, Chi V, Brooks FP, Washburn S, and Superfine R, (1998), Nanomanipulation experiments exploring frictional and mechanical properties of carbon nanotubes, *Microsc. Microanal.* 4(5): 504–512.

218. Falvo MR, Taylor RM, Helser A, Chi V, Brooks FP, Washburn S, and Superfine R, (1999), Nanometre-scale rolling and sliding of carbon nanotubes, *Nature.* 397(6716): 236–238.

219. Falvo MR, Steele J, Taylor RM, and Superfine R, (2000), Evidence of commensurate contact and rolling motion: AFM manipulation studies of carbon nanotubes on hopg, *Tribol, Lett.* 9(1–2): 73–76.

220. Falvo MR, Steele J, Taylor RM, and Superfine R, (2000), Gearlike rolling motion mediated by commensurate contact: carbon nanotubes on hopg, *Phys. Rev. B.* 62(16): R10665-R10667.

221. Schall JD and Brenner DW, (2000), Molecular dynamics simulations of carbon nanotube rolling and sliding on graphite, *Molecular Simulation.* 25(1–2): 73–79.

222. Buldum A and Lu JP, (1999), Atomic scale sliding and rolling of carbon nanotubes, *Phys. Rev. Lett.* 83(24): 5050–5053.

223. Kolmogorov AN and Crespi VH, (2000), Smoothest bearings: Interlayer sliding in multi-walled carbon nanotubes, *Phys. Rev. Lett.* 85(22): 4727–4730.

224. Shenoy VB, Miller R, Tadmor EB, Phillips R, and Ortiz M, (1998), Quasicontinuum models of interfacial structure and deformation, *Phys. Rev. Lett.* 80(4): 742–745.

225. Miller R, Ortiz M, Phillips R, Shenoy V, and Tadmor EB, (1998), Quasicontinuum models of fracture and plasticity, *Eng, Fracture Mech.* 61(3–4): 427–444.

226. Miller R, Tadmor EB, Phillips R, and Ortiz M, (1998), Quasicontinuum simulation of fracture at the atomic scale, *Modelling Sim. Mater. Sci. Eng.* 6(5): 607–638.

227. Shenoy VB, Miller R, Tadmor EB, Rodney D, Phillips R, and Ortiz M, (1999), An adaptive finite element approach to atomic-scale mechanics — the quasicontinuum method, *J. Mech. Phys. Solids.* 47(3): 611–642.

228. Tadmor EB, Miller R, Phillips R, and Ortiz M, (1999), Nanoindentation and incipient plasticity, *J. Mater. Res.* 14(6): 2233–2250.

229. Rodney D and Phillips R, (1999), Structure and strength of dislocation junctions: An atomic level analysis, *Phys. Rev. Lett.* 82(8): 1704–1707.

230. Smith GS, Tadmor EB, and Kaxiras E, (2000), Multiscale simulation of loading and electrical resistance in silicon nanoindentation, *Phys. Rev. Lett.* 84(6): 1260–1263.

231. Knap J and Ortiz M, (2001), An analysis of the quasicontinuum method, *J. Mech Phys. Solids.* 49(9): 1899–1923.

232. Shin CS, Fivel MC, Rodney D, Phillips R, Shenoy VB, and Dupuy L, (2001), Formation and strength of dislocation junctions in fcc metals: a study by dislocation dynamics and atomistic simulations, *J. Physique Iv.* 11(PR5): 19–26.

233. Shenoy V, Shenoy V, and Phillips R, (1999), Finite temperature quasicontinuum methods, in *Multiscale Modelling of Materials*, Ghoniem N (Ed.), Materials Research Society, Warrendale, PA, 465–471.

234. Arroyo M and Belytschko T, (2002), An atomistic-based membrane for crystalline films one atom thick *J. Mech. Phys. Solids*. 50: 1941–1977.

235. Liu WK and Chen YJ, (1995), Wavelet and multiple scale reproducing kernel methods, *Intl. J. Numerical Meth. Fluids*. 21(10): 901–931.

236. Liu WK, Jun S, and Zhang YF, (1995), Reproducing kernel particle methods, *Intl. J. Numerical Meth. Fluids*. 20(8–9): 1081–1106.

237. Liu WK, Jun S, Li SF, Adee J, and Belytschko T, (1995), Reproducing kernel particle methods for structural dynamics, *Intl. J. Numerical Meth. Eng*. 38(10): 1655–1679.

238. Liu WK, Chen YJ, Uras RA, and Chang CT, (1996), Generalized multiple scale reproducing kernel particle methods, *Computer Meth. Appl. Mech. Eng*. 139(1–4): 91–157.

239. Liu WK, Chen Y, Chang CT, and Belytschko T, (1996), Advances in multiple scale kernel particle methods, *Computational Mech*. 18(2): 73–111.

240. Liu WK, Jun S, Sihling DT, Chen YJ, and Hao W, (1997), Multiresolution reproducing kernel particle method for computational fluid dynamics, *Intl. J. Numerical Meth. Fluids*. 24(12): 1391–1415.

241. Liu WK, Li SF, and Belytschko T, (1997), Moving least-square reproducing kernel methods. 1. Methodology and convergence, *Computer Meth. Appl. Mech. Eng*. 143(1–2): 113–154.

242. Liu WK, Belytscho T, and Oden JT. (Eds.), (1996), *Computer Meth. Appl. Mech. Eng*. Vol. 139.

243. Chen JS and Liu WK (Eds.), (2000), *Computational Mech*. Vol. 25.

244. Odegard GM, Gates TS, Nicholson LM, and Wise KE, (2001), *Equivalent-Continuum Modeling of Nano-Structured Materials*. NASA Langley Research Center, NASA-2001-TM 210863.

245. Odegard GM, Harik VM, Wise KE, and Gates TS, (2001), *Constitutive Modeling of Nanotube-Reinforced Polymer Composite Systems*. NASA Langley Research Center, NASA-2001-TM 211044.

246. Abraham FF, Broughton JQ, Bernstein N, and Kaxiras E, (1998), Spanning the continuum to quantum length scales in a dynamic simulation of brittle fracture, *Europhys. Lett*. 44(6): 783–787.

247. Broughton JQ, Abraham FF, Bernstein N, and Kaxiras E, (1999), Concurrent coupling of length scales: methodology and application, *Phys. Rev. B*. 60(4): 2391–2403.

248. Nakano A, Bachlechner ME, Kalia RK, Lidorikis E, Vashishta P, Voyiadjis GZ, Campbell TJ, Ogata S, and Shimojo F, (2001), Multiscale simulation of nanosystems, *Computing Sci. Eng*. 3(4): 56–66.

249. Rafii-Tabar H, Hua L, and Cross M, (1998), Multiscale numerical modelling of crack propagation in two-dimensional metal plate, *Mater. Sci. Tech*. 14(6): 544–548.

250. Rafii-Tabar H, Hua L, and Cross M, (1998), A multi-scale atomistic-continuum modelling of crack propagation in a two-dimensional macroscopic plate, *J. Phys. Condensed Matter*. 10(11): 2375–2387.

251. Rudd RE and Broughton JQ, (1998), Coarse-grained molecular dynamics and the atomic limit of finite elements, *Phys. Rev. B*. 58(10): R5893-R5896.

252. Rudd RE and Broughton JQ, (2000), Concurrent coupling of length scales in solid state systems, *Physica Status Solidi B-Basic Research*. 217(1): 251–291.

253. Liu WK, Zhang Y, and Ramirez MR, (1991), Multiple scale finite-element methods, *Intl. J. Numerical Meth. Eng*. 32(5): 969–990.

254. Liu WK, Uras RA, and Chen Y, (1997), Enrichment of the finite element method with the reproducing kernel particle method, *J. Appl. Mech. Trans. ASME*. 64(4): 861–870.

255. Hao S, Liu WK, and Qian D, (2000), Localization-induced band and cohesive model, *J. Appl. Mech. Trans. ASME*. 67(4): 803–812.

256. Wagner GJ, Moes N, Liu WK, and Belytschko T, (2001), The extended finite element method for rigid particles in stokes flow, *Intl. J. Numerical Meth. Eng*. 51(3): 293–313.

257. Wagner GJ and Liu WK, (2001), Hierarchical enrichment for bridging scales and mesh-free boundary conditions, *Intl. J. Numerical Meth. Eng*. 50(3): 507–524.

258. Wagner GJ and Liu WK, (2002), Coupling of atomistic and continuum simulations (in preparation).

259. Costello GA, (1978), Analytical investigation of wire rope, *Appl. Mech. Rev. ASME*. 31: 897–900.

260. Costello GA, (1997), *Theory of Wire Rope*. 2nd ed. Springer. New York.

261. Qian D, Liu WK, and Ruoff RS, (2002), Load transfer mechanism in nano-ropes, Computational Mechanics Laboratory Research Report (02-03) Dept. of Mech. Eng., Northwestern University.

262. Ruoff RS, Qian D, Liu WK, Ding WQ, Chen XQ, and Dikin D (Eds.), (2002), What kind of carbon nanofiber is ideal for structural applications? *43rd AIAA/ASME/ASCE/AHS Struct. Struct. Dynamics Mater. Conf.* Denver, CO.

263. Pipes BR and Hubert P, (2001), Helical carbon nanotube arrays: mechanical properties (submitted).

264. Yu MF, Dyer MJ, Skidmore GD, Rohrs HW, Lu XK, Ausman KD, Von Ehr JR, and Ruoff RS, (1999), Three-dimensional manipulation of carbon nanotubes under a scanning electron microscope, *Nanotechnology*. 10(3): 244–252.

265. Ruoff RS, Lorents DC, Chan B, Malhotra R, and Subramoney S, (1993), Single-crystal metals encapsulated in carbon nanoparticles, *Science*. 259(5093): 346–348.

266. Tomita M, Saito Y, and Hayashi T, (1993), Lac2 encapsulated in graphite nano-particle, *Jpn. J. App. Phys. Part 2–Lett.* 32(2B): L280-L282.

267. Seraphin S, Zhou D, Jiao J, Withers JC, and Loutfy R, (1993), Selective encapsulation of the carbides of yttrium and titanium into carbon nanoclusters, *Appl. Phys. Lett.* 63(15): 2073–2075.

268. Seraphin S, Zhou D, Jiao J, Withers JC, and Loutfy R, (1993), Yttrium carbide in nanotubes, *Nature*. 362(6420): 503–503.

269. Seraphin S, Zhou D, and Jiao J, (1996), Filling the carbon nanocages, *J. Appl. Phys.* 80(4): 2097–2104.

270. Saito Y, Yoshikawa T, Okuda M, Ohkohchi M, Ando Y, Kasuya A, and Nishina Y, (1993), Synthesis and electron-beam incision of carbon nanocapsules encaging yc2, *Chem. Phys. Lett.* 209(1–2): 72–76.

271. Saito Y, Yoshikawa T, Okuda M, Fujimoto N, Sumiyama K, Suzuki K, Kasuya A, and Nishina Y, (1993), Carbon nanocapsules encaging metals and carbides, *J. Phys. Chem. Solids*. 54(12): 1849–1860.

272. Saito Y and Yoshikawa T, (1993), Bamboo-shaped carbon tube filled partially with nickel, *J. Crystal Growth*. 134(1–2): 154–156.

273. Saito Y, Okuda M, and Koyama T, (1996), Carbon nanocapsules and single-wall nanotubes formed by arc evaporation, *Surf. Rev. Lett.* 3(1): 863–867.

274. Saito Y, Nishikubo K, Kawabata K, and Matsumoto T, (1996), Carbon nanocapsules and single-layered nanotubes produced with platinum-group metals (Ru, Rh, Pd, Os, Ir, Pt) by arc discharge, *J. Appl. Phys.* 80(5): 3062–3067.

275. Saito Y, (1996), Carbon cages with nanospace inside: fullerenes to nanocapsules, *Surf. Rev. Lett.* 3(1): 819–825.

276. Saito Y, (1995), Nanoparticles and filled nanocapsules, *Carbon*. 33(7): 979–988.

277. McHenry ME, Majetich SA, Artman JO, Degraef M, and Staley SW, (1994), Superparamagnetism in carbon-coated Co particles produced by the kratschmer carbon-arc process, *Phys. Rev. B*. 49(16): 11358–11363.

278. Majetich SA, Artman JO, McHenry ME, Nuhfer NT, and Staley SW, (1993), Preparation and properties of carbon-coated magnetic nanocrystallites, *Phys. Rev. B*. 48(22): 16845–16848.

279. Jiao J, Seraphin S, Wang XK, and Withers JC, (1996), Preparation and properties of ferromagnetic carbon-coated Fe, Co, and Ni nanoparticles, *J. Appl. Phys.* 80(1): 103–108.

280. Diggs B, Zhou A, Silva C, Kirkpatrick S, Nuhfer NT, McHenry ME, Petasis D, Majetich SA, Brunett B, Artman JO, and Staley SW, (1994), Magnetic properties of carbon-coated rare-earth carbide nanocrystallites produced by a carbon-arc method, *J. Appl. Phys.* 75(10): 5879–5881.

281. Brunsman EM, Sutton R, Bortz E, Kirkpatrick S, Midelfort K, Williams J, Smith P, McHenry ME, Majetich SA, Artman JO, Degraef M, and Staley SW, (1994), Magnetic-properties of carbon-coated, ferromagnetic nanoparticles produced by a carbon-arc method, *J. Appl. Phys.* 75(10): 5882–5884.

282. Funasaka H, Sugiyama K, Yamamoto K, and Takahashi T, (1995), Synthesis of actinide carbides encapsulated within carbon nanoparticles, *J. Appl. Phys.* 78(9): 5320–5324.

283. Kikuchi K, Kobayashi K, Sueki K, Suzuki S, Nakahara H, Achiba Y, Tomura K, and Katada M, (1994), Encapsulation of radioactive gd-159 and tb-161 atoms in fullerene cages, *J. Am. Chem. Soc.* 116(21): 9775–9776.

284. Burch WM, Sullivan PJ, and McLaren CJ, (1986), Technegas – a new ventilation agent for lung-scanning, *Nucl. Med. Commn.* 7(12): 865.

285. Senden TJ, Moock KH, Gerald JF, Burch WM, Browitt RJ, Ling CD, and Heath GA, (1997), The physical and chemical nature of technegas, *J. Nucl. Med.* 38(8): 1327–1333.

286. Ajayan PM and Iijima S, (1993), Capillarity-induced filling of carbon nanotubes, *Nature.* 361(6410): 333–334.

287. Ajayan PM, Ebbesen TW, Ichihashi T, Iijima S, Tanigaki K, and Hiura H, (1993), Opening carbon nanotubes with oxygen and implications for filling, *Nature.* 362(6420): 522–525.

288. Tsang SC, Harris PJF, and Green MLH, (1993), Thinning and opening of carbon nanotubes by oxidation using carbon-dioxide, *Nature.* 362(6420): 520–522.

289. Xu CG, Sloan J, Brown G, Bailey S, Williams VC, Friedrichs S, Coleman KS, Flahaut E, Hutchison JL, Dunin-Borkowski RE, and Green MLH, (2000), 1d lanthanide halide crystals inserted into single-walled carbon nanotubes, *Chem. Commn.* (24): 2427–2428.

290. Tsang SC, Chen YK, Harris PJF, and Green MLH, (1994), A simple chemical method of opening and filling carbon nanotubes, *Nature.* 372(6502): 159–162.

291. Sloan J, Hammer J, Zwiefka-Sibley M, and Green MLH, (1998), The opening and filling of single walled carbon nanotubes (swts), *Chem. Commn.* (3): 347–348.

292. Hiura H, Ebbesen TW, and Tanigaki K, (1995), Opening and purification of carbon nanotubes in high yields, *Adv. Mater.* 7(3): 275–276.

293. Hwang KC, (1995), Efficient cleavage of carbon graphene layers by oxidants, *J. Chem. Soc. -Chem. Commn.* (2): 173–174.

294. Ajayan PM, Colliex C, Lambert JM, Bernier P, Barbedette L, Tence M, and Stephan O, (1994), Growth of manganese filled carbon nanofibers in the vapor-phase, *Phys. Rev. Lett.* 72(11): 1722–1725.

295. Subramoney S, Ruoff RS, Lorents DC, Chan B, Malhotra R, Dyer MJ, and Parvin K, (1994), Magnetic separation of gdc2 encapsulated in carbon nanoparticles, *Carbon.* 32(3): 507–513.

296. Tsang SC, Davis JJ, Green MLH, Allen H, Hill O, Leung YC, and Sadler PJ, (1995), Immobilization of small proteins in carbon nanotubes – high- resolution transmission electron-microscopy study and catalytic activity, *J. Chem. Soc. Chem. Commn.* (17): 1803–1804.

297. Tsang SC, Guo ZJ, Chen YK, Green MLH, Hill HAO, Hambley TW, and Sadler PJ, (1997), Immobilization of platinated and iodinated oligonucleotides on carbon nanotubes, *Angewandte Chemie.* 36(20): 2198–2200. International Edition in English.

298. Dillon AC, Jones KM, Bekkedahl TA, Kiang CH, Bethune DS, and Heben MJ, (1997), Storage of hydrogen in single-walled carbon nanotubes, *Nature.* 386(6623): 377–379.

299. Gadd GE, Blackford M, Moricca S, Webb N, Evans PJ, Smith AN, Jacobsen G, Leung S, Day A, and Hua Q, (1997), The world's smallest gas cylinders? *Science.* 277(5328): 933–936.

300. Sloan J, Wright DM, Woo HG, Bailey S, Brown G, York APE, Coleman KS, Hutchison JL, and Green MLH, (1999), Capillarity and silver nanowire formation observed in single walled carbon nanotubes, *Chem. Commn.* (8): 699–700.

301. Smith BW and Luzzi DE, (2000), Formation mechanism of fullerene peapods and coaxial tubes: a path to large scale synthesis, *Chem. Phys. Lett.* 321(1–2): 169–174.

302. Smith BW, Monthioux M, and Luzzi DE, (1998), Encapsulated c-60 in carbon nanotubes, *Nature.* 396(6709): 323–324.

303. Smith BW, Monthioux M, and Luzzi DE, (1999), Carbon nanotube encapsulated fullerenes: a unique class of hybrid materials, *Chem. Phys. Lett.* 315(1–2): 31–36.

304. Burteaux B, Claye A, Smith BW, Monthioux M, Luzzi DE, and Fischer JE, (1999), Abundance of encapsulated c-60 in single-wall carbon nanotubes, *Chem. Phys. Lett.* 310(1–2): 21–24.

305. Sloan J, Dunin-Borkowski RE, Hutchison JL, Coleman KS, Williams VC, Claridge JB, York APE, Xu CG, Bailey SR, Brown G, Friedrichs S, and Green MLH, (2000), The size distribution, imaging and obstructing properties of c-60 and higher fullerenes formed within arc-grown single walled carbon nanotubes, *Chem. Phys. Lett.* 316(3–4): 191–198.

306. Zhang Y, Iijima S, Shi Z, and Gu Z, (1999), Defects in arc-discharge-produced single-walled carbon nanotubes, *Philos. Mag. Lett.* 79(7): 473–479.

307. Pederson MR and Broughton JQ, (1992), Nanocapillarity in fullerene tubules, *Phys. Rev. Lett.* 69(18): 2689–2692.

308. Prasad R and Lele S, (1994), Stabilization of the amorphous phase inside carbon nanotubes — solidification in a constrained geometry, *Philos. Mag. Lett.* 70(6): 357–361.

309. Berber S, Kwon YK, and Tomanek D, (2001), Unpublished.

310. Stan G and Cole MW, (1998), Hydrogen adsorption in nanotubes, *J. Low Temp. Phys.* 110(1–2): 539–544.

311. Mao ZG, Garg A, and Sinnott SB, (1999), Molecular dynamics simulations of the filling and decorating of carbon nanotubules, *Nanotechnology.* 10(3): 273–277.

312. Stan G, Gatica SM, Boninsegni M, Curtarolo S, and Cole MW, (1999), Atoms in nanotubes: small dimensions and variable dimensionality, *Am. J. Phys.* 67(12): 1170–1176.

313. Liu J, Casavant MJ, Cox M, Walters DA, Boul P, Lu W, Rimberg AJ, Smith KA, Colbert DT, and Smalley RE, (1999), Controlled deposition of individual single-walled carbon nanotubes on chemically functionalized templates, *Chem. Phys. Lett.* 303(1–2): 125–129.

314. Chung J, Lee JH, Ruoff RS, and Liu WK, (2001), Nanoscale gap fabrication and integration of carbon nanotubes by micromachining (in preparation).

315. Ren Y and Price DL, (2001), Neutron scattering study of h-2 adsorption in single-walled carbon nanotubes, *Appl. Phys. Lett.* 79(22): 3684–3686.

316. Zhang YG, Chang AL, Cao J, Wang Q, Kim W, Li YM, Morris N, Yenilmez E, Kong J, and Dai HJ, (2001), Electric-field-directed growth of aligned single-walled carbon nanotubes, *Appl. Phys. Lett.* 79(19): 3155–3157.

317. Collins PG, Bradley K, Ishigami M, and Zettl A, (2000), Extreme oxygen sensitivity of electronic properties of carbon nanotubes, *Science.* 287(5459): 1801–1804.

318. Kong J, Franklin NR, Zhou CW, Chapline MG, Peng S, Cho KJ, and Dai HJ, (2000), Nanotube molecular wires as chemical sensors, *Science.* 287(5453): 622–625.

319. Yamamoto K, Akita S, and Nakayama Y, (1998), Orientation and purification of carbon nanotubes using ac electrophoresis, *J. Phys. D Appl. Phys.* 31(8): L34-L36.

320. Tombler TW, Zhou CW, Alexseyev L, Kong J, Dai HJ, Lei L, Jayanthi CS, Tang MJ, and Wu SY, (2000), Reversible electromechanical characteristics of carbon nanotubes under local-probe manipulation, *Nature.* 405(6788): 769–772.

321. Maiti A, (2001), Application of carbon nanotubes as electromechanical sensors – results from first-principles simulations, *Physica Status Solidi B-Basic Research.* 226(1): 87–93.

322. Maiti A, Andzelm J, Tanpipat N, and von Allmen P, (2001), Carbon nanotubes as field emission device and electromechanical sensor: results from first-principles dft simulations, *Abstr. Papers Am. Chem. Soc.* 222: 204.

323. Kong J, Chapline MG, and Dai HJ, (2001), Functionalized carbon nanotubes for molecular hydrogen sensors, *Adv. Mater.* 13(18): 1384–1386.

324. Peng S and Cho KJ, (2000), Chemical control of nanotube electronics, *Nanotechnology.* 11(2): 57–60.

325. Wood JR, Frogley MD, Meurs ER, Prins AD, Peijs T, Dunstan DJ, and Wagner HD, (1999), Mechanical response of carbon nanotubes under molecular and macroscopic pressures, *J. Phys. Chem. B.* 103(47): 10388–10392.

326. Wood JR and Wagner HD, (2000), Single-wall carbon nanotubes as molecular pressure sensors, *Appl. Phys. Lett.* 76(20): 2883–2885.

327. Wood JR, Zhao Q, Frogley MD, Meurs ER, Prins AD, Peijs T, Dunstan DJ, and Wagner HD, (2000), Carbon nanotubes: From molecular to macroscopic sensors, *Phys. Rev. B*. 62(11): 7571–7575.

328. Zhao Q, Wood JR, and Wagner HD, (2001), Using carbon nanotubes to detect polymer transitions, *J. Polymer Sci. Part B-Polymer Phys*. 39(13): 1492–1495.

329. Zhao Q, Wood JR, and Wagner HD, (2001), Stress fields around defects and fibers in a polymer using carbon nanotubes as sensors, *Appl. Phys. Lett*. 78(12): 1748–1750.

330. Ilic B, Czaplewski D, Craighead HG, Neuzil P, Campagnolo C, and Batt C, (2000), Mechanical resonant immunospecific biological detector, *Appl. Phys. Lett*. 77(3): 450–452.

331. Carr DW, Evoy S, Sekaric L, Craighead HG, and Parpia JM, (1999), Measurement of mechanical resonance and losses in nanometer scale silicon wires, *App. Phys. Lett*. 75(7): 920–922.

331a. Yu MF, Wagner GJ, Ruoff RS, and Dyer MJ, (2002), Realization of parametric resonances in a nanowire mechanical system with nanomanipulation inside a scanning electron microscope, *Phys. Rev. B*, in press.

332. Turner KL, Miller SA, Hartwell PG, MacDonald NC, Strogatz SH, and Adams SG, (1998), Five parametric resonances in a microelectromechanical system, *Nature*. 396(6707): 149–152.

333. Sandler J, Shaffer MSP, Prasse T, Bauhofer W, Schulte K, and Windle AH, (1999), Development of a dispersion process for carbon nanotubes in an epoxy matrix and the resulting electrical properties, *Polymer*. 40(21): 5967–5971.

334. Schadler LS, Giannaris SC, and Ajayan PM, (1998), Load transfer in carbon nanotube epoxy composites, *Appl. Phys. Lett*. 73(26): 3842–3844.

335. Qian D, Dickey EC, Andrews R, and Rantell T, (2000), Load transfer and deformation mechanisms in carbon nanotube-polystyrene composites, *Appl. Phys. Lett*. 76(20): 2868–2870.

336. Ajayan PM, Schadler LS, Giannaris C, and Rubio A, (2000), Single-walled carbon nanotube-polymer composites: strength and weakness, *Adv. Mater*. 12(10): 750–753.

337. Thostenson ET, Ren ZF, and Chou TW, (2001), Advances in the science and technology of carbon nanotubes and their composites: a review, *Composites Sci. Technol*. 61(13): 1899–1912.

338. Jin L, Bower C, and Zhou O, (1998), Alignment of carbon nanotubes in a polymer matrix by mechanical stretching, *Appl. Phys. Lett*. 73(9): 1197–1199.

339. Haggenmueller R, Gommans HH, Rinzler AG, Fischer JE, and Winey KI, (2000), Aligned single-wall carbon nanotubes in composites by melt processing methods, *Chem. Phys. Lett*. 330(3–4): 219–225.

340. Barrera EV, (2000), Key methods for developing single-wall nanotube composites, *Jom-J. Minerals Metals Mater. Soc*. 52(11): A38-A42.

341. Fischer JE, (2002) Nanomechanics and the viscoelastic behavior of carbon nanotube-reinforced polymers. Ph.D. thesis. Northwestern University, Evanston.

342. Fisher FT, Bradshaw RD, and Brinson LC, (2001), Effects of nanotube waviness on the mechanical properties of nanoreinforced polymers, *Appl. Phys. Lett*. 80(24): 4647–4649.

343. Shaffer MSP and Windle AH, (1999), Fabrication and characterization of carbon nanotube/poly(vinyl alcohol) composites, *Adv. Mater*. 11(11): 937–941.

344. Gong XY, Liu J, Baskaran S, Voise RD, and Young JS, (2000), Surfactant-assisted processing of carbon nanotube/polymer composites, *Chem. Mater*. 12(4): 1049–1052.

345. Lozano K, Bonilla-Rios J, and Barrera EV, (2001), A study on nanofiber-reinforced thermoplastic composites (II): Investigation of the mixing rheology and conduction properties, *J. Appl. Polymer Sci*. 80(8): 1162–1172.

346. Qian D and Liu WK, (2002), In preparation.

347. Mitsubishi chemical to mass-produce nanotech substance, (2001), in *Kyodo News*.